CORNELL UNIVERSITY

Center for Radiophysics and Space Research

ITHACA, N. Y.

CRSR 753

ONE MILLIMETER CONTINUUM OBSERVATIONS OF EXTRAGALACTIC THERMAL SOURCES

Thomas Leonard Roellig, Ph.D.

ONE MILLIMETER CONTINUUM OBSERVATIONS OF EXTRAGALACTIC THERMAL SOURCES

Thomas Leonard Roellig, Ph.D.
Cornell University, 1981

A composite bolometer detector system operating at 0.37°K has been developed for making 1 mm continuum observations using the 5 m Hale telescope on Mount Palomar. The cryostat employs adsorption pumping of liquid ^{3}He to attain this low temperature. The electrical NEP of the bolometer is 1×10^{-15} W/$\sqrt{\text{Hz}}$. On the telescope in the best weather the system can detect a flux level of 5.8 Jy with a signal to noise ratio of 1:1 in one second of integration.

The ^{3}He detector system has been used to make 1 mm continuum observations of extragalactic thermal sources. Eight spiral galaxies, NGC 1068, and M 82 were observed. Of this sample, M 82, NGC 253, NGC 4631, and NGC 6946 were detected with a statistical significance of better than 2σ. The 3σ upper limits of the other galaxies were approximately 1 Jy. For the galaxies in the sample that have been detected at far infrared wavelengths (M 82, NGC 253, NGC 6946, NGC 1068, and IC 342), the 1 mm points are found to lie on a modified black body curve $B' = B(\nu,T)\nu^p$. The 1 mm results indicate that $p \approx 1.5$ for NGC 253, M 82, and NGC 6946, while for NGC 1068 $p \geq 2.0$. The color temperatures derived from the far infrared observations lie in the 30-40°K range. Similar

parameters result from observations of molecular clouds in our galaxy. Therefore, the observations are consistent with the 1 mm emission from the galaxies originating in a molecular cloud environment. This would imply that there is not a great deal of 10-20°K interstellar dust in these galaxies.

There seems to be no correlation between the 1 mm flux and the total HI emission from the galaxies. There is perhaps a correlation between the level of synchrotron emission and the 1 mm flux from the galaxies.

The 1 mm flux from three points along the galactic plane of M 82 was measured. Only emission from the nucleus was detected, indicating that the dust distribution is strongly peaked at the location of the nucleus. This sharp peak is also seen in CO.

Estimates of the gas to dust ratio for the observed galaxies range from less than 31:1 to greater than 200:1. These estimates assume that $[CO]/[H_2] = 4 \times 10^{-5}$ and $Q/a\rho = 5 \times 10^{-2}$ cm^2/g for the dust.

ONE MILLIMETER CONTINUUM OBSERVATIONS OF EXTRAGALACTIC THERMAL SOURCES

A Thesis

Presented to the Faculty of the Graduate School

of Cornell University

in Partial Fulfillment for the Degree of

Doctor of Philosophy

by

Thomas Leonard Roellig

January, 1981

Biographical Sketch

Thomas Leonard Roellig was born on June 5, 1953, in Ann Arbor, Michigan. He attended public schools in Michigan and London, England, and received a B.S. in Physics from Stanford University in 1975. On August 7, 1976, he married Marianne Petersen. During his stay at Cornell University he was a teaching assistant for two years and a research assistant for three. In 1979 he received a Master's degree in Applied Physics from Cornell University.

ACKNOWLEDGMENTS

First and most importantly, I would like to acknowledge the assistance, instruction, and support of my research advisor, Jim Houck. Jim's wide range of knowledge was an invaluable asset in my research, from the design and construction of the equipment to the interpretation of the results. Jim was also very patient and understanding, qualities that I especially appreciated during the observing field trips.

I would also especially like to acknowledge the assistance of my opposite number at Cal Tech, Dave Ennis. Dave assisted in making most of the observations reported here and spent a great deal of his own time helping me on my visits to Cal Tech.

The night assistants at the Mount Palomar and Siding Springs observatories were always willing to expend a little extra personal effort to make sure the observations were a success. I would also like to thank Gerry Neugebauer for the temporary use of his laboratories at Cal Tech.

During the field trip to Australia, Dave Jauncey was very helpful in getting everything organised and running smoothly.

George Gull and Gerry Stasavage helped in the construction of the instrumentation.

I would like to thank Martin Harwit and Ed Salpeter for serving on my committee as well as for their useful suggestions. Bill Forrest and Gary Melnick should also be

acknowledged for their discussions.

Barbara Boettcher and Mary Wright were responsible for the diagrams and typing, respectively, of this thesis.

Last, but certainly not least, I would like to thank my friends and family, and especially my wife, Marianne, for their support and encouragement.

This work was supported by National Aeronautics and Space Administration grant NSG-7324.

Table of Contents

Chapter		Page
1	Introduction.	1
2	Observing 1 mm Radiation.	5
	Detectors.	5
	The atmosphere	5
	Telescopes and observing sites	9
3	Instrumentation	12
	Cryostat	12
	Bolometer.	20
	Filters.	21
	Photometer	21
	Telescopes	22
	Electronics and data system.	23
4	Observing Procedures and Data Reduction . .	30
	Observing procedure.	30
	Millimeter flux standards.	37
	Data reduction	39
5	Observations of Extragalactic Thermal Sources	41
	Introduction	41
	Observations	42
	Millimeter and submillimeter spectra . .	43
	Dust masses.	65
	Flux correlations.	70

Table of Contents (cont'd)

Chapter		Page
	Individual objects.	79
	M 82	79
	NGC 253.	85
	NGC 6946	87
	NGC 4631	88
	IC 342	90
	NGC 1068	91
	Upper limits.	99
	The Milky Way galaxy.	100
	Summary	102
Appendix A	The Bolometer	104
	Theory and performance	104
	Total system noise	111
	Bolometer construction	119
Appendix B	Filters and Field Optics.	129
Appendix C	Atmospheric Corrections	142
References	. . . . .	151

List of Tables

Table		Page
3-1	Cryostat Performance	20
3-2	Bolometer Performance	21
3-3	Preamplifier Performance	26
4-1	Calibration Standards	38
5-1	Nuclear Positions.	44
5-2	Observations	45
5-3	Isothermal Dust Model Parameters.	59
5-4	Two Temperature Dust Model	65
5-5	Values of Q/aρ at 1 mm for Some Suggested Grain Materials.	69
5-6	Dust Mass Column Densities	71
5-7	Galactic Distances	72
5-8	Total Dust Masses.	73
5-9	Upper Limits	100
A-1	Symbol Definitions	107
A-2	Dewar Noise at 10 Hz, Measured at the Bolometer	113
A-3	Measured Bolometer Electrical Performance. .	113
A-4	Heat Capacity of Bolometer Elements.	122
B-1	Bolometer Optical Performance.	141

List of Illustrations

Figure		Page
2-1	Atmospheric transmission and dewar response.	7
3-1	^{3}He dewar	14
3-2	Pumping system.	16
3-3	Beam profile.	24
3-4	5 m data system	27
3-5	4 m data system	29
4-1	Beam nomenclature	31
5-1	Galactic spectra.	47
5-2	Flux derivation nomenclature.	67
5-3	HI - 1 mm plots.	76
5-4	Synchroton - 1 mm plot	78
5-5	Scans along plane of M 82	82
A-1	Schematic diagram of a bolometer.	105
A-2	^{3}He bolometer signal and noise.	114
A-3	Noise spectrum.	116
A-4	^{3}He bolometer	121
A-5	Bolometer soldering	126
B-1	Filters and field optics used in dewar. . . .	130
B-2	Diffraction transmission curves	134
B-3	Dewar response - grating monochromater	139
B-4	Dewar response - Fourier transform spectrometer.	140

List of Illustrations (cont'd)

Figure		Page
C-1	Q curves.	144
C-2	Corrected flux of 7027.	145
C-3	Effective wavelength of system.	149

Chapter 1

Introduction

The field of millimeter continuum astronomy is still in its infancy. Observations are so difficult that the technology needed to make useful astronomical measurements has only recently been developed. The difficulty of making observations is due to three factors.

First of all, the atmosphere is essentially opaque to radiation from 20 μm to 750 μm as far as ground based observations are concerned. Beyond 750 μm the atmosphere becomes more transparent, but the atmosphere still attenuates and introduces noise into the celestial radiation.

The second difficulty in making 1 mm observations is caused by the state of the art of detector technology. Detectors in the near and mid infrared regions of the spectrum (1 μm-30 μm) have a great deal of use in military and industrial applications. As a result, development of these detectors has been well funded and the detector technology is relatively advanced. Typically, infrared astronomers working in this wavelength region are able to purchase excellent detectors from industrial sources. The detectors used in 1 mm astronomy are generally fabricated by the astronomers themselves and have not been subject to the intensive development of the photoconductor and photovoltaic devices used in shorter wavelength work. As a result

of this limitation, 1 mm astronomy is as much a field of detector technology as it is observational astronomy.

Lastly, most astronomical sources are very faint at a wavelength of 1 mm. This wavelength region is long enough to be well into the Rayleigh-Jeans tail of thermal sources ($T > 5°K$) and yet too short for strong synchrotron emission. In spite of these difficulties, 1 mm observations are important since they can provide information about astronomical objects that is unavailable at other wavelengths.

Astronomical objects that are observed at 1 mm can be put into three main categories.

a) Thermal sources. 1 mm thermal sources include solar system bodies, spiral galaxies, molecular clouds, Class II Seyfert galaxies, and planetary nebulae. With the exception of the planetary nebulae all of these sources emit 1 mm radiation either from the surfaces of the objects themselves or from heated dust grains. The 1 mm emission from planetary nebulae is due to thermal bremstrahlung. The brightest sources in the 1 mm sky, the sun, Jupiter, and Saturn, are all thermal sources. 1 mm observations of the solar system objects can provide information about their atmospheres and the composition of their surfaces. Measurements of the 1 mm flux from planetary nebulae can check for the presence of ultra compact components. As will be seen in more detail later, 1 mm measurements and maps of dusty objects can provide very useful information about the temperature, composition, and distribution of the

dust.

b) Non-thermal sources. Observed non-thermal sources have been either radio galaxies, QSO's, Class I Seyferts, or supernovae remnants. In general, the 1 mm flux from these objects can be predicted by extrapolating from the radio spectrum (Ennis, 1980). Measurements at 1 mm are useful because they can set limits on the energy density and magnetic fields in these objects.

c) Cosmic background. The 3°K cosmic background has roughly a blackbody spectrum. Thus, its peak is near a wavelength of 1 mm. Unfortunately, the severe atmospheric noise generally negates the value of photometric observations at this wavelength, since accurate calibration is impossible. As a result, most cosmic background work has been in the context of investigations of the spectrum. 1 mm observations are also useful for special projects such as searching for small scale inhomogeneities in the background radiation or observing the Sunyavev-Zeldovich effect in clusters of galaxies (Gould and Rephaeli, 1978).

This work reports the results of 1 mm observations of extragalactic thermal sources. The methods of making 1 mm observations are described in Chapter 2. The instrumentation used to make the observations is described in Chapter 3, with more details on its theory of operation and construction given in Appendices A and B. The observing procedure followed is given in Chapter 4. More details on the

data reduction, especially the atmospheric correction procedures, are given in Appendix C. The results of the observations, together with their interpretation, is given in Chapter 5.

This work was done in collaboration with members of the infrared group at Cal Tech. In this collaboration the Cornell group provided the detector and filters, while the Cal Tech workers provided the photometer. We jointly obtained the telescope time on the 5 m Hale telescope. The observations themselves were made by joint research teams composed of members of both groups. The observations and results reported here constitute part of the author's contributions to the program. The other results of this collaboration appear in the open literature.

Chapter 2

Observing 1 mm Radiation

Detectors

Two different types of detectors are presently in use in making 1 mm astronomical observations. The first type of detector is a superheterodyne system similar in principle to those used in radio astronomy. In millimeter work an InSb crystal usually functions as the mixer. The sensitivity of these devices is limited by the power of the local oscillator. Since high harmonics of a Klystron generator are used to supply the local oscillator power, the sensitivity of these devices is relatively low, with system temperatures of a few thousand degrees. Since the bandwidth of these devices is quite small, they have been used chiefly in molecular line work.

The second type of 1 mm detector is the bolometer. These devices are incoherent detectors with very large bandwidths. As a result, they are more suitable for continuum work than are the superheterodyne receivers. The detector used in this study was a bolometer. The theory of operation for these detectors and the methods of their construction are treated in Appendix A.

The Atmosphere

One of the biggest problems in making 1 mm observations is caused by the atmosphere. As can be seen in Figure 2-1,

the atmosphere is essentially opaque at ground based observing sites from 20 μm to 750 μm. Most of the atmospheric absorption is due to water vapor, with smaller amounts of absorption due to oxygen, ozone, and carbon dioxide (Traub and Stier, 1976).

In reducing the 1 mm results, the first step is to remove obvious noise spikes from the data. The data is then corrected for the effects of the atmosphere. In practice, this means using an atmospheric model to find the effective attenuation through the detector wavelength passband. Since the dominant source of atmospheric opacity is due to water at these wavelengths, good atmospheric correction procedures need accurate water vapor measurements.

One way of measuring the water vapor content of the atmosphere is to measure the dew point during the observations. This technique has been employed by Rowan-Robinson et al. (1975) in reducing their 1 mm data. Because this method only measures ground level water vapor, non-uniform atmospheric conditions cause inaccuracies in this procedure.

A more accurate method is described in Elias et al. (1978) and was used for the 1 mm results presented here. Briefly, this method employs measuring the infrared flux from the sun both in and just outside of the 1.9 μm water band. This measurement is made using a calibrated Westphal meter (Westphal, 1974). This technique has the advantage that it measures the integrated water vapor content through the whole atmosphere. Unfortunately, with the present

Figure 2-1: a) Atmospheric transmission from 1 μm to 1000 μm, with 1.2 mm of precipitable water vapor (Traub and Stier, 1975).

b) Smoothed passband of detector and dewar used in the 1 mm observations reported here.

a)

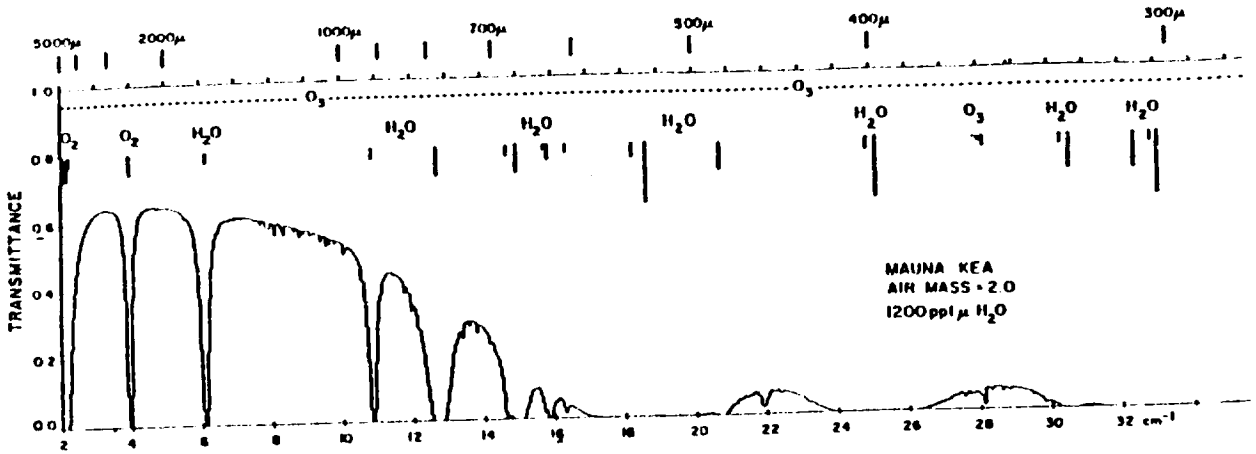
5000μ
2000μ
1000μ
700μ
500μ
400μ
300μ
O_3
O_2
H_2O
TRANSMITTANCE
MAUNA KEA
AIR MASS = 2.0
1200 ppt μ H_2O
cm⁻¹

b)

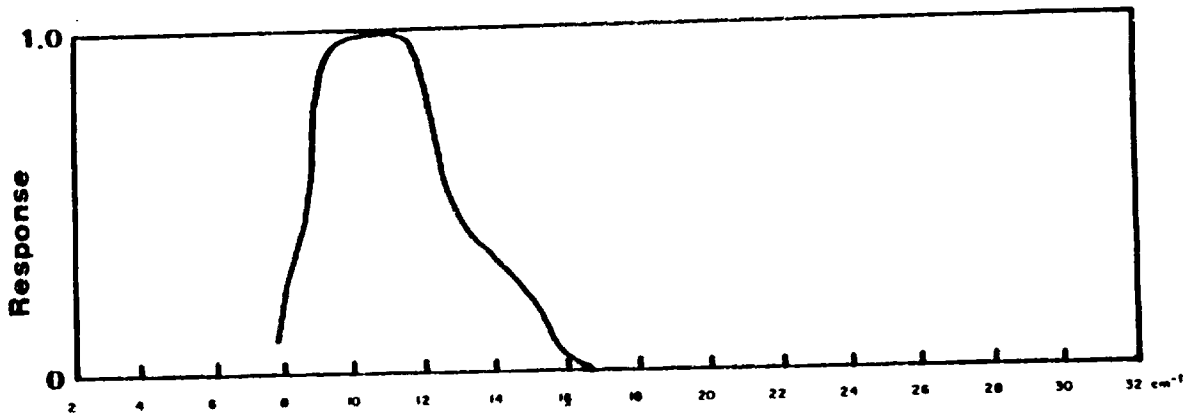
1.0
Response
0
cm⁻¹

equipment the method cannot be used at night. The Westphal meter readings can be converted into precipitable millimeters of water, which can then be used as a parameter in an accurate atmospheric correction model. The atmospheric model used to reduce the data presented in this work is described in Appendix C.

Telescopes and Observing Sites

1 mm observations have been made from balloons and ground based observatories. Aircraft observatories have been used in some submillimeter observations, but have not been used at 1 mm. The use of high altitude balloons has the advantage of removing a great deal of the atmospheric attenuation of the celestial signals, permitting observations at submillimeter wavelengths as well as at 1 mm. Balloon telescopes have the disadvantage of small size (generally their mirror diameters are 1 m or less), which limits both the spatial resolution and the collecting area. They also have the disadvantage that their flights are of limited duration, thus long observing sessions are not possible. As a result of these drawbacks, balloon telescopes have only been used at millimeter wavelengths for 3°K cosmic background work, where the reduction of atmospheric effects is the overriding concern (Woody and Richards, 1979).

For most of the past work at 1 mm, ground based telescopes have been used. These telescopes are either the

millimeter dishes used in molecular line radio astronomy or large optical telescopes. Large ground based telescopes can be much larger than balloon borne telescopes. Their diffraction limited beam sizes are of the order of 1', which allows reasonably fine scale mapping to be undertaken. The large apertures also make the detection of faint point sources possible. There are two disadvantages in using these telescopes. First of all, their use is subject to the weather. Since observations are generally made during the winter so that the water vapor levels will be low, the weather is frequently cloudy. The second disadvantage lies in the popularity of these telescopes; it is difficult to get observing time. 1 mm astronomers are fortunate in that they can work in the daytime, so that they can share the telescope with a nighttime observer.

For ground based work at 1 mm, the observing site is just as important as the telescope that is used. The best sites are at locations where the water vapor content of the atmosphere is very low. In practice, this means that the observatories are located at high altitudes. For example, as far as sensitivity is concerned, the 5 m Hale telescope on Mount Palomar (alt. 1706 m) is much better than the 10 m dish at Owen's Valley (alt. 1216 m). This is due to a smaller amount of water vapor over the Hale telescope, which more than balances out the factor of four in the collecting area. The ideal site for 1 mm ground based astronomy is atop Mauna Kea in Hawaii, since this location

has very little water vapor. Plans exist to build a 10 m millimeter (Leighton) dish at this location in the near future. Longer range plans include building a 25 m telescope for Mauna Kea. The observations presented in this work were made at either the 5 m Hale telescope or at the 4 m Anglo-Australian telescope (alt. 1165 m).

Chapter 3

Instrumentation

The 1 mm observations reported here were made using a composite bolometer operating at pumped ^{3}He temperatures. The reasons for going to such low temperatures are detailed in Appendix A. This chapter is concerned mainly with describing the cryostat, photometer, telescopes, and electronics of the instrumentation.

Cryostat

For astronomical applications, using pumped ^{3}He cryostats is the most convenient way of reaching temperatures of less than 1.0°K. Such cryostats are compact, relatively simple, and stable, facilitating their use on telescopes. Pumped ^{3}He reaches lower temperatures than pumped ^{4}He for three reasons: a) ^{3}He has a higher vapor pressure than ^{4}He at all temperatures, thus reaching lower temperatures for a given pumping pressure, b) ^{3}He is a fermion, so there is no superfluid film to transport heat for T > 10 m°K, and c) the lack of a superfluid film means that the pumping lines can be constructed of large diameter tubing without the small orifices needed in pumped ^{4}He dewars. Since ^{3}He is an expensive gas (~ $160/liter STP), the pumping mechanism employed must be closed so that the ^{3}He can be recovered. For our purposes, an additional constraint in the dewar design was set by size, since the dewar was intended to be

compatible with an existing photometer on the 5 m Hale telescope.

The basic dewar configuration is shown in Figure 3-1 and consists of a liquid N_2 bath and radiations shield, a liquid ^4He bath and work surface, and a vacuum jacket. The maximum height of the dewar is only 16".

The ^3He pumping system is shown in Figure 3-2. An adsorption pump with a mechanical heat switch was used to provide a fast, closed, and vibrationless pump. With the exception of the condenser, the pumping lines running from the liquid chamber to the adsorption pump are all of thin wall 3/16" stainless steel tubing, giving a pumping speed at 4°K greater than 1 1/2" tubing at room temperature. The condenser is constructed of OFHC copper and is thermally clamped to the ^4He work surface. In order to give a good thermal contact between the work surface and the condenser, the surfaces that were clamped together were gold plated. The gas flows through the condenser through seven 1.6 mm holes. This impedance, although slowing the pumping speed slightly, increases the cold surface available for condensation and stops oscillations in the ^3He pumping line. The adsorption pump consists of a 2" diameter OFHC copper ball filled with activated charcoal. The ball has numerous internal fins made of OFHC copper so that any piece of charcoal is in close proximity to a cold surface. A 1/8" thin wall stainless steel tube runs from the ball to a refrigeration gauge and various plumbing fittings on the top of the dewar.

Figure 3-1: Drawing of ^{3}He dewar used in observations.

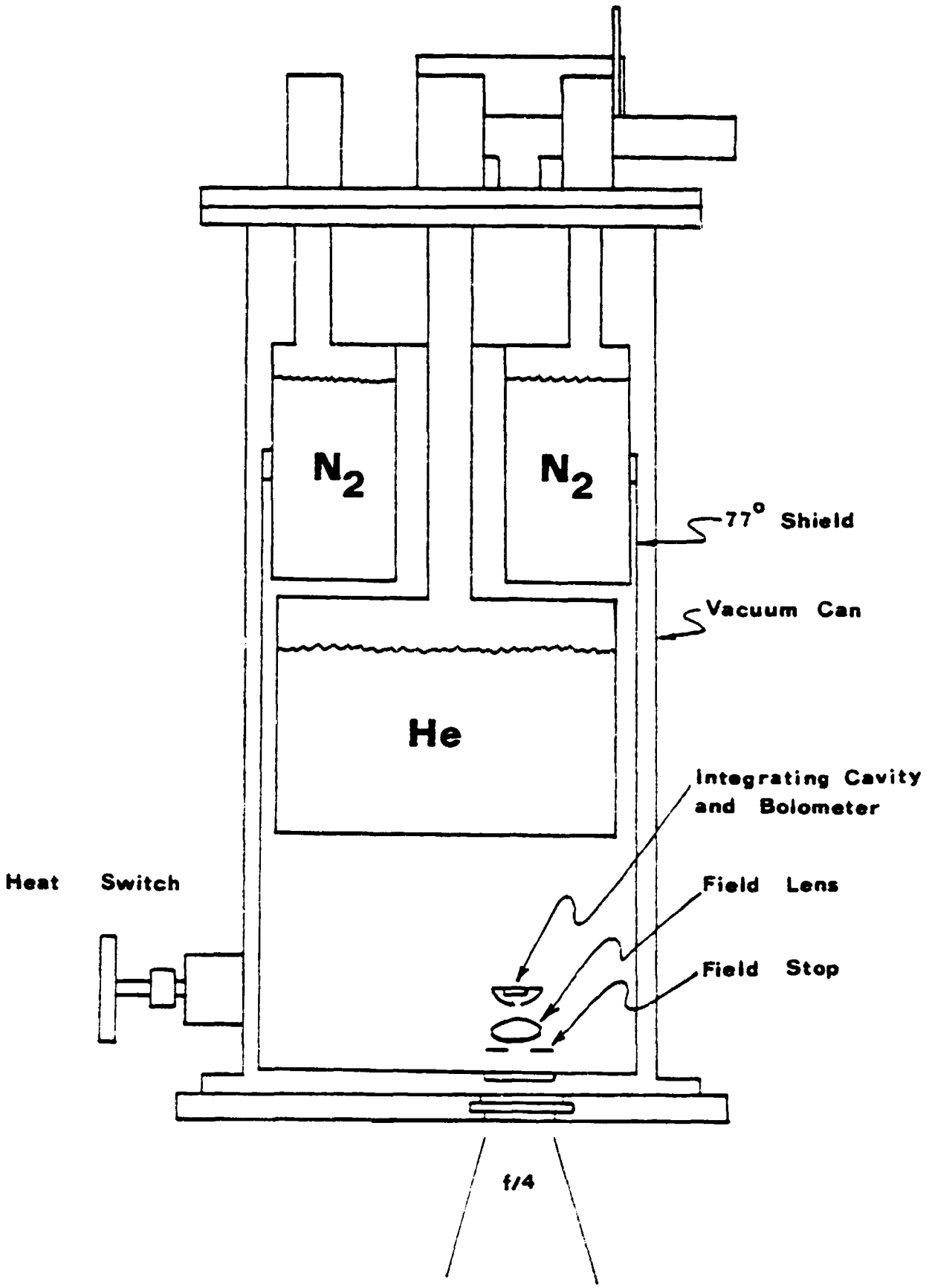
N_2
N_2
77° Shield
Vacuum Can
He
Integrating Cavity
and Bolometer
Heat Switch
Field Lens
Field Stop
f/4

Figure 3-2: Schematic diagram of the ^{3}He adsorption pumping system.

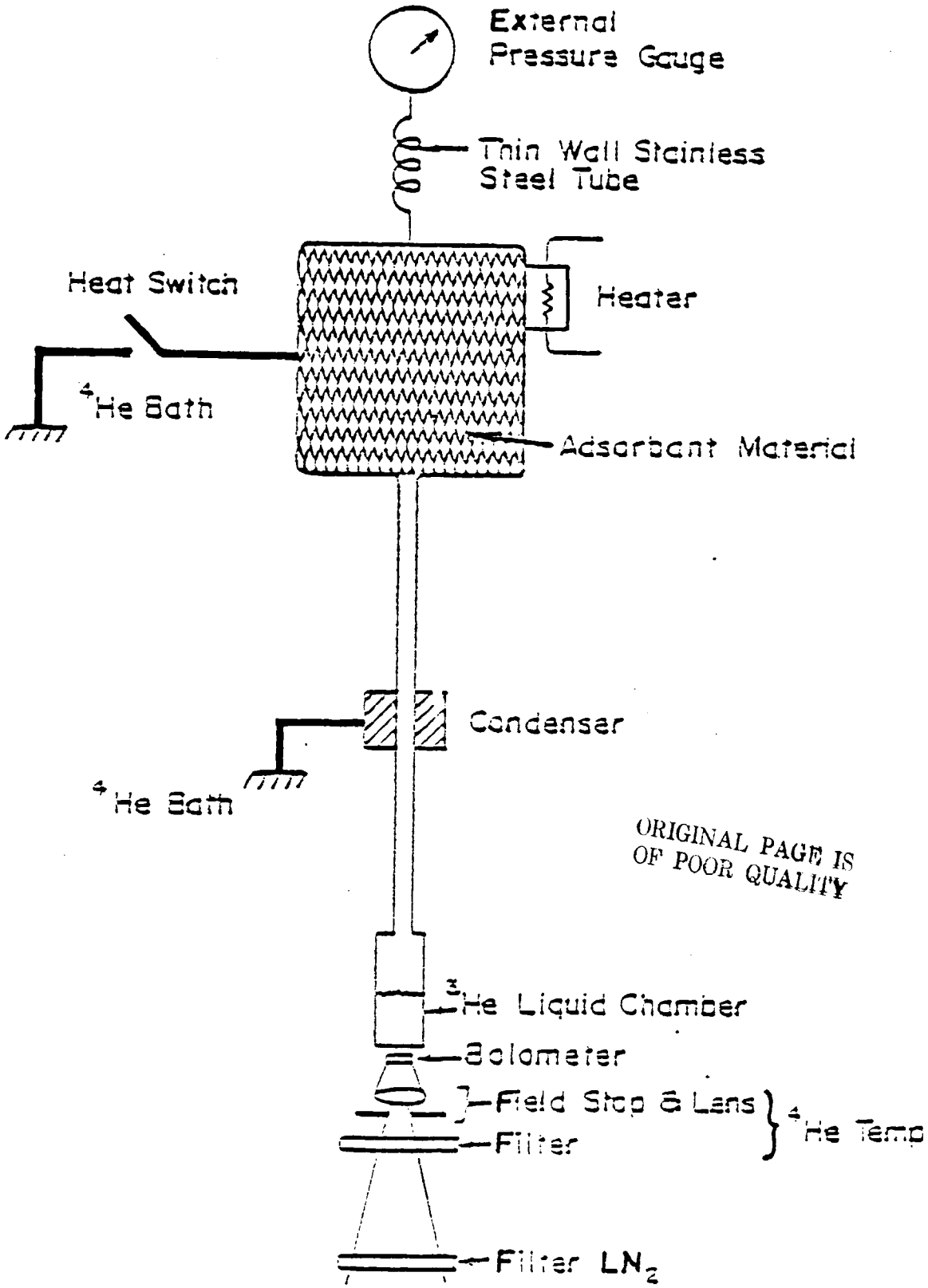

The refrigeration gauge is used for monitoring the ^{3}He pressure, while the fittings are used to charge the dewar with ^{3}He. The heat switch is mechanical, with a geared drive that strongly presses two gold plated OFHC copper contacts together. One of these contacts is soldered to the ^{4}He work surface while the other is soldered to a thick braided copper grounding strap connected to the ball containing the activated charcoal. The heat switch shaft leading into the dewar from the outside world has an Oldham coupling. This allows the shaft to be disconnected to reduce the thermal heat load into the dewar.

The operation of the cryostat is as follows.

1) The ^{4}He bath is topped off and the heat switch is opened, breaking the thermal path between the ball and the ^{4}He work surface.

2) A special fitting is attached to the ^{4}He fill tube and the ^{4}He bath is pumped to as low a temperature as possible. At the same time, current is run through a 100 ohm heating resistor on the ball. A 15 volt input puts 1 watt of heat into the charcoal. (The missing power is dissipated in the wires inside the dewar, which have a resistance of 50Ω.) The heater is turned off about 25 minutes later when the charcoal reaches approximately 50°K. This temperature is high enough to insure that all of the ^{3}He is driven from the charcoal. As soon as the ^{4}He bath drops below the condensation temperature, the ^{3}He will start condensing in the condenser. At 1 atm the condensation temperature of ^{3}He is

3.2°K. The critical temperature is only 3.35°K, so that the ^{4}He bath must be pumped to a lower temperature than this before condensation occurs. Gravity causes the ^{3}He droplets to then run down the pumping line and into the liquid chamber. Eventually, the ^{4}He bath is as cold as it will get (about 1.5°K in the present dewar configuration). At this time approximately 90% of the ^{3}He is in liquid form, filling a volume of 1.4 cm^3 in the liquid chamber.

3) The heat switch is then closed, which starts cooling the adsorbant. At the same time the pump is disconnected from the ^{4}He bath, allowing the ^{4}He bath temperature to rise to 4.2°K. As the ball temperature drops below 15°K the ^{3}He will start to readsorb onto the charcoal. Within 20 minutes the temperature in the liquid ^{3}He chamber will have dropped to the operating temperature. This temperature has been determined to be 0.37°K by a calibrated Ge thermometer. The loss in cooling the ^{3}He to this temperature is only about 15% of the original volume of liquid. The ^{3}He itself has the greatest heat capacity and its self-cooling is responsible for most of this loss.

4) Topping up the ^{4}He bath completes the start-up procedure.

The heat load on the ^{3}He is low enough so that the hold time at 0.37°K is approximately 15 hours. The complete list of the cryostat performance specifications is given in Table 3-1.

Table 3-1

Cryostat Performance

Liquid N_2 hold time	12 hours
Liquid He hold time	14 hours
Pumped ^3He hold time	15 hours
Operating temperature	0.37°K
Heat load into the ^3He	13 μW
Thermal conductivity of heat switch	45 mW/°K
Volume of ^3He pumping system	120 cm^3
Amount of ^3He used in dewar	1 liter STP
Volume of ^4He bath	0.87 liters
Volume of liquid N_2 bath	0.80 liters

Bolometer

A full discussion of the bolometer, including the theory of operation, performance, and construction, is given in Appendix A. Briefly, the bolometer is a composite design with a semiconductor thermistor element. A listing of its performance is given in Table 3-2. On the 5 m Hale telescope in the best weather the bolometer can detect 5.8 Jy with a signal:noise ratio of one in 1 second of integration time.

Table 3-2

Bolometer Performance

Electrical NEP	1.5×10^{-15} W/$\sqrt{\text{Hz}}$
Optical NEP at 10 Hz, f/35 beam	5×10^{-15} W/$\sqrt{\text{Hz}}$
Thermal time constant	14 μs
Operating temperature	0.37°K

Filters

The filters used for the observations are covered in detail in Appendix B. We will only note here that the half power points of the dewar transmission passband are at 750 μm and 1200 μm.

Photometer

The bolometer dewar is mounted on a chopping photometer at the prime focus of the telescope. In its original configuration this photometer has been described in Elias et al. (1978). Briefly, it is a reimaging system with a wobbling tertiary mirror that performs the chopping. Recently, the photometer has been modified at Cornell for a larger chopper throw and for remote control operation.

The photometer reimages the beam from the telescope into the dewar. At the same time, the beam shape also changes from the telescope's f/3.3 to f/4.0. The photometer servo drives the tertiary mirror to follow an input waveform provided by a standard function generator. The photometer

can chop as far as 4' and at a rate of 20 Hz before the mirror encounters difficulty in following a square wave input. The photometer orientation can be changed to chop in any direction. At the 5 m Hale telescope the drive electronics only permit the telescope to nod automatically in the N-S or E-W directions.

A motor driven 45° flat mirror is located inside the photometer top. With the mirror in the beam the light is reflected into a television camera. In the viewing mode accurate telescope pointing can be obtained from observations of bright stars. The television camera has enough sensitivity and contrast so that stars down to the 4th magnitude can be observed in daylight against a deep blue sky using the 5 m Hale telescope. This is about as well as the human eye can do. At night the television system limiting magnitude is roughly 8.5. The human eye does much better than this! Therefore, for certain applications where pointing must be determined from dim stars at night, the television camera can be removed and an observer can ride in the prime focus cage and do the pointing. In practice, the television system has been sufficient for all of our observations. When the mirror is pulled out of the beam, the radiation enters the bolometer dewar. The mirror position may be changed from the observatory data room.

Telescopes

The observations were made at either the 5 m Hale

telescope on Mount Palomar or the 4 m Anglo-Australian telescope at Siding Springs. The same photometer was used on both telescopes, since the beam shapes at prime focus were almost identical. The dewar incorporated a field stop of 1/4" diameter. With the f/4 beam on the 5 m telescope the geometrical beam size was 66" on the sky. Due to diffraction effects, the beam shape was not perfectly square, but could be approximated by a Gaussian core with enhanced wings (Figure 3-3). The FWHM of the measured beam was 55". The Anglo-Australian telescope was similar to the Hale telescope, except that the primary mirror diameter is 3.8 m. As a result, the geometrical beam size on the Anglo-Australian telescope was 88" on the sky. Lack of a suitably bright source precluded measuring the beam shape on the 4 m telescope; it was assumed to have been the same as on the 5 m telescope. This would correspond to a FWHM beam size of 73". The observing procedures used on these telescopes are given in Chapter 4.

Electronics and Data System

The voltage signals from the bolometer are first amplified by a preamp mounted on the dewar. The performance of this amplifier is shown in Table 3-3. The amplifier was designed to have the lowest noise possible. The JFET used in the front end was specially selected for its low-noise characteristics. To further reduce the noise, the preamp is powered by two 13.6 volt mercury batteries. The capacity of the batteries is large enough so that the preamp can be operated for over 40 hours before battery changes

Figure 3-3: Beam shape of the 1 mm system on the 5 m Hale telescope, obtained by scanning the planet Saturn.

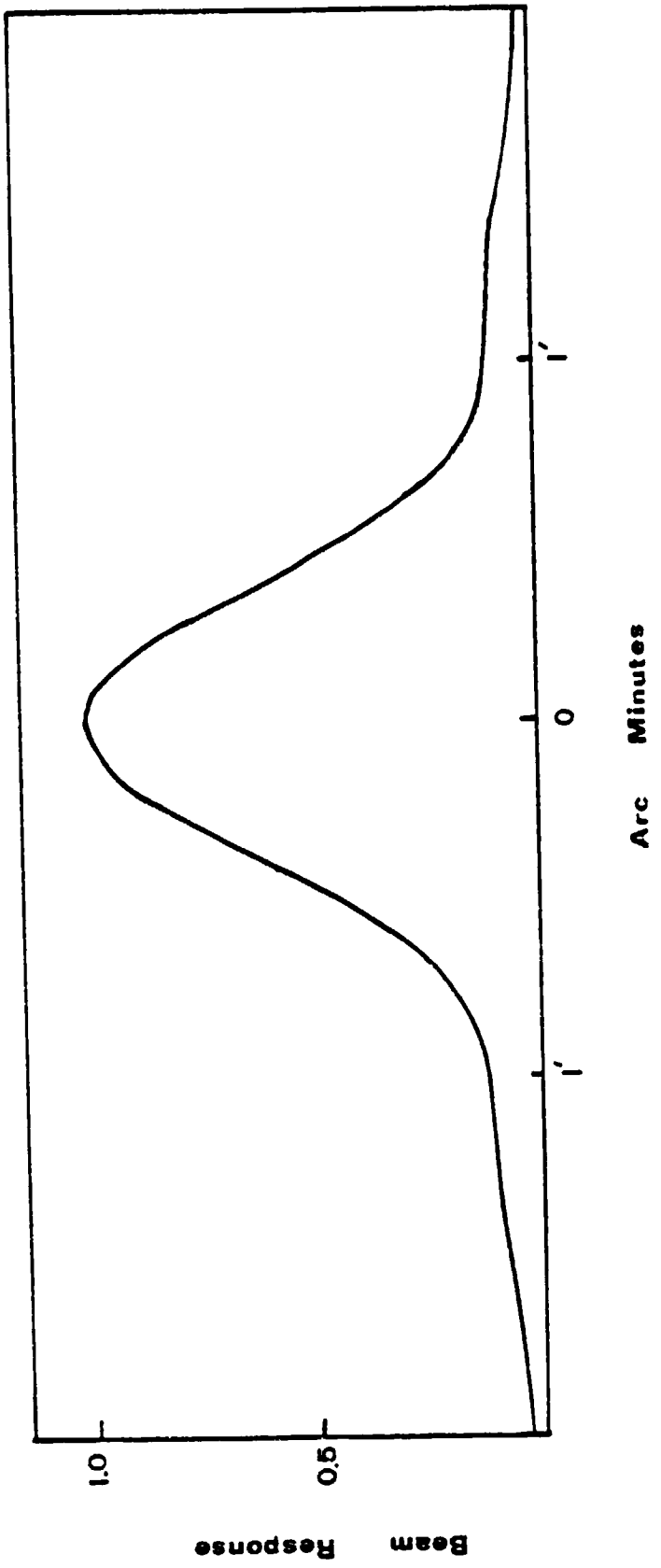
1.0
0.5
Beam Response
1'
0
1'
Arc Minutes

Table 3-3

Preamplifier Performance

Voltage gain at 10 Hz	858
Voltage noise at 10 Hz	4.1 $nV/\sqrt{Hz}$
Current noise at 10 Hz	3.4 $fA/\sqrt{Hz}$

become necessary. The bolometer bias voltage source is also contained in the preamp box and is powered by these same batteries. Proper shielding is very important in eliminating pickup from nearby electronics. In order to provide this shielding the preamp was bolted directly to the vacuum jacket of the bolometer dewar. In addition, the wires connecting the front end of the amplifier to the bolometer and load resistor were made as short as possible and were doubly shielded.

The output of the preamp entered either of two data systems (shown schematically in Figures 3-4 and 3-5) depending on the telescope in use. At the Hale telescope, integration was performed by counting the cycles out of a voltage to frequency converter. At the Anglo-Australian telescope the in-house computer system allowed us to perform the integrations in the data acquisition computer after sampling the output of the lock-in amplifier.

Figure 3-4: Schematic diagram of the data system used on the 5 m Hale telescope.

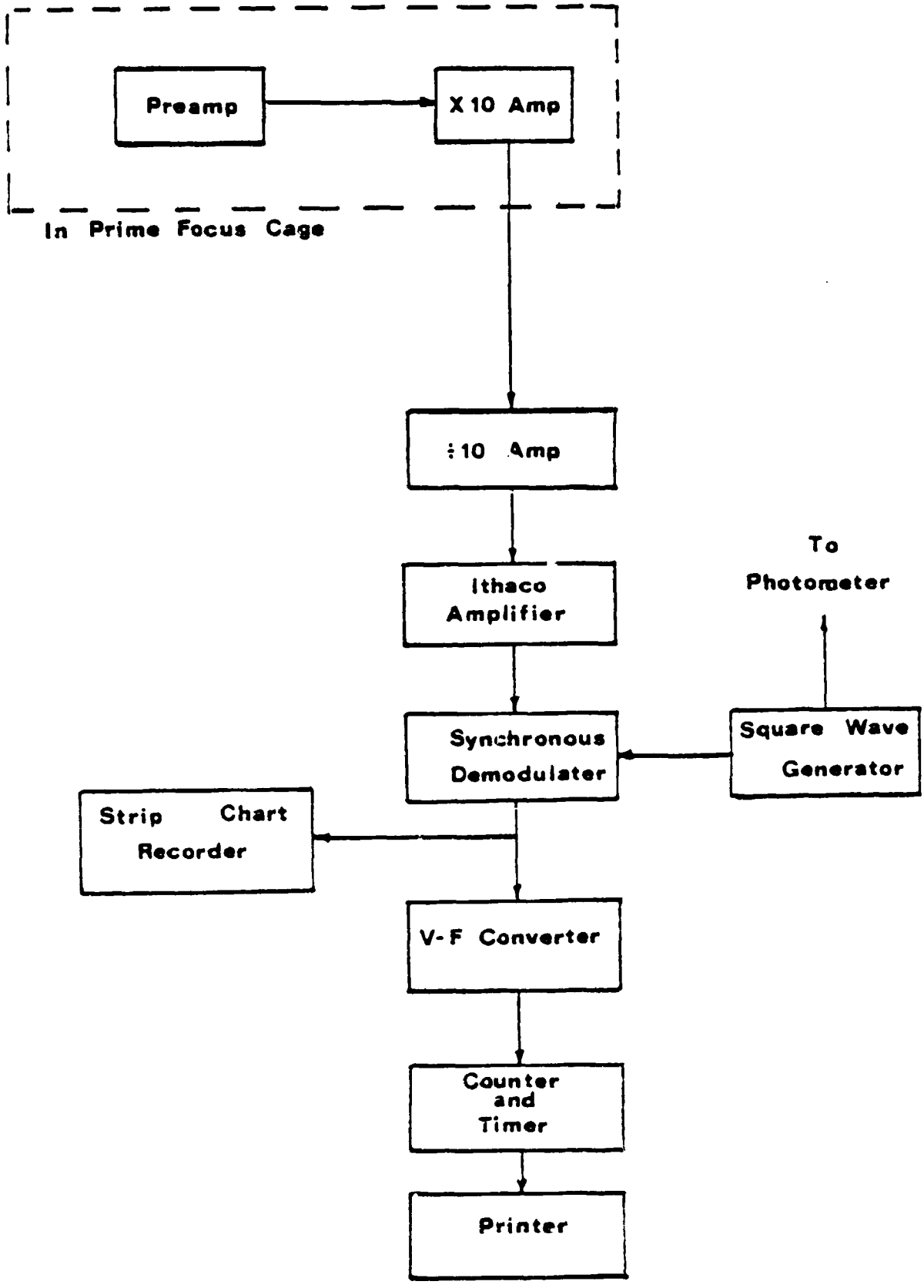
Preamp
X 10 Amp
In Prime Focus Cage
÷10 Amp
Ithaco Amplifier
To Photometer
Synchronous Demodulater
Square Wave Generator
Strip Chart Recorder
V-F Converter
Counter and Timer
Printer

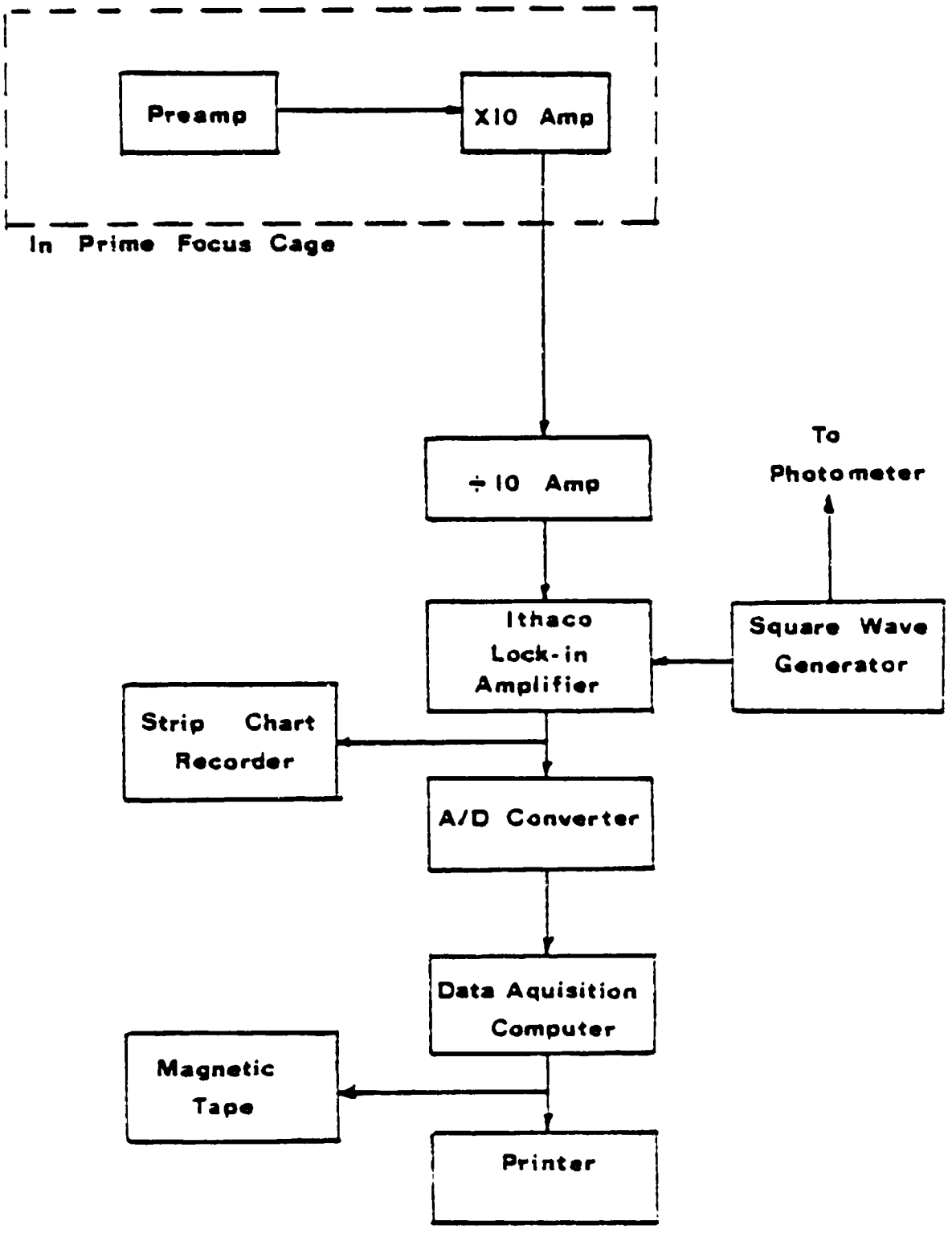

Figure 3-5: Schematic diagram of the data system used at the 4 m Anglo-Australian telescope.

Chapter 4

Observing Procedure and Data Reduction

Observing Procedure

During the 1 mm observations special observing procedures were followed to insure low noise accurate flux measurements. Because the atmosphere causes a great deal of trouble in making 1 mm astronomical observations, most of the observing procedures are therefore employed to minimize the effects of the atmosphere.

The observed millimeter flux from any object aside from the sun is much less than the emission from the atmosphere and telescope. As a result, differential measurement techniques that allow partial cancellation of the atmospheric emission are used. When the wobbling tertiary mirror in the photometer is driven by a square wave signal, it has the effect of rapidly alternating the telescope position between two spots in the sky. This is shown in Figure 4-1. When the telescope is positioned so that the object being observed is in the left beam, the telescope is defined to be in the signal position. Conversely, when the telescope is positioned so that the object is in the right beam, the telescope is defined to be in the reference position. If F_{RB} and F_{LB} are the fluxes entering the bolometer dewar from the left and right beams, respectively, we find that the AC signal when the telescope is in the signal position is

Figure 4-1: Diagram of the beam positions and nomenclature used in differential flux measurements. In the signal position the object is in the left beam as the wobbling tertiary mirror chops in a square wave pattern at 11 Hz. To move to the reference telescope position the telescope is nodded the distance of the chopper throw. The telescope nods back and forth every 20 seconds.

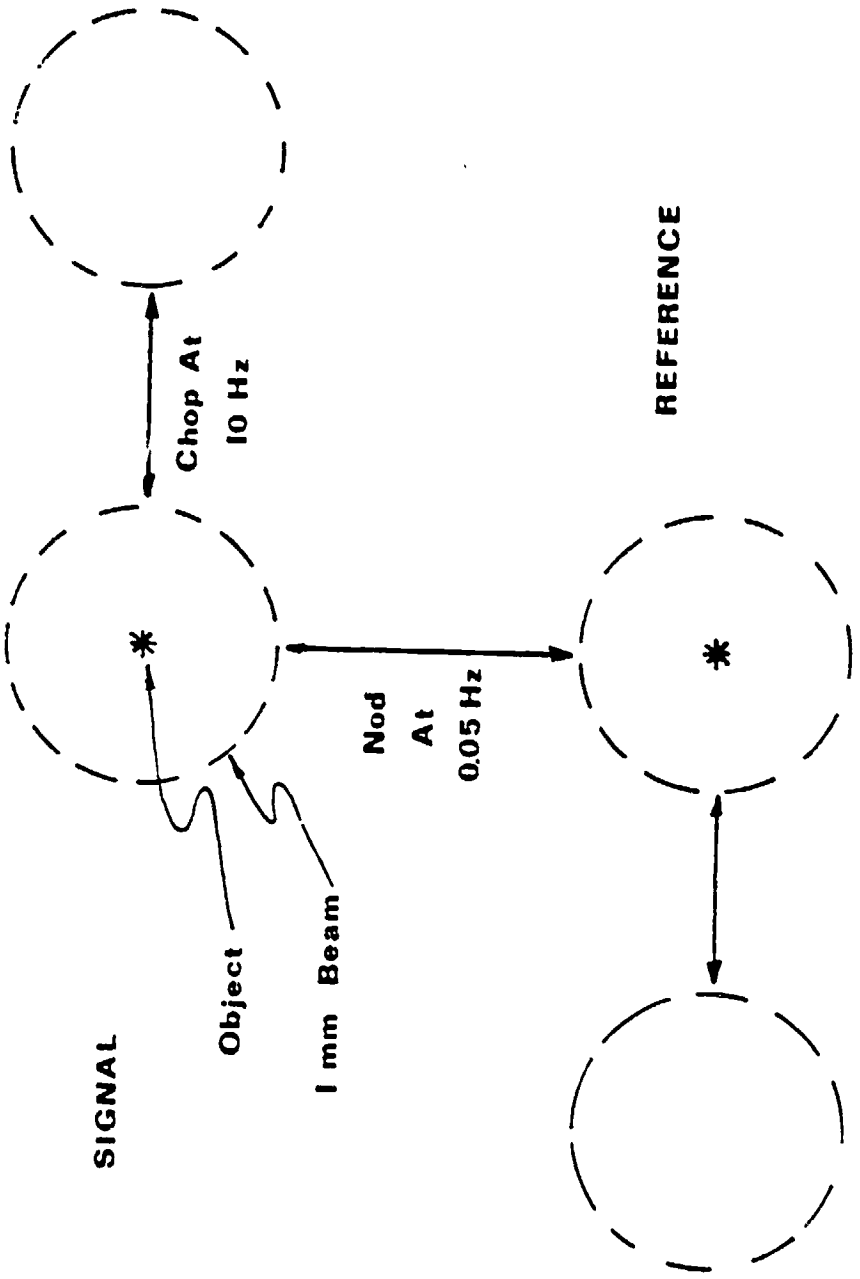
SIGNAL
Object
1 mm Beam
Nod
At
0.05 Hz
REFERENCE
Chop At
10 Hz

$$S_S = R(F_{LB} - F_{RB}) \tag{4.1}$$

where R is the dewar responsivity in volts per watt. Breaking down the total fluxes into their various components we have

$$S_S = R[(F_o + F_a + F_t)_{LB} - (F_a + F_t)_{RB}] \tag{4.2}$$

where F_o is the flux from the object, F_a is the flux from atmospheric emission, and F_t is the flux from emission from the warm telescope and photometer. Similarly, the AC signal when the telescope is in the reference position is

$$S_R = R[F_{LB} - F_{RB}] \tag{4.3}$$

or

$$S_R = R[(F_a + F_t)_{LB} - (F_a + F_t + F_o)_{RB}] \tag{4.4}$$

The electronics of the data system synchronously demodulate and integrate the AC signals. As long as the atmospheric emission is the same in both beams (a good approximation except when there are clouds or an approaching frontal system) the signal from the object will then be given by

$$S_o = RF_o = \frac{R}{2}[\int S_S - \int S_R] \tag{4.5}$$

This procedure therefore cancels out almost all of the effects of the telescope and atmospheric emission.

The telescope is nodded between the signal and reference positions every 20 seconds. This allows two 10 second integrations in each position. When the weather is only marginal, it is sometimes advantageous to nod the telescope more

frequently, perhaps every three seconds. This tends to remove some of the excess sky noise. The disadvantage with shortening the integration time is that the time it takes the telescope to move and settle after every nod is time lost for integration purposes. A standard run for a very bright object such as a planet is two pairs, or SRRS, where S and R refer to integrations with the telescope in the signal and reference positions, respectively. For longer integration runs a SRRSSR...RS pattern was followed. This had the effect of cancelling out the effects of a monotonic linear change in the weather conditions. The standard observing block for fainter objects was composed of 16 pairs of 10 second integrations.

The details of the observing procedure are given below.

1) Initial set-up: The first task undertaken in any observing trip is to allign the millimeter and optical beams. To do this it is necessary to observe an object that is bright at both 1 mm and optical wavelengths. The ideal objects are the planets Venus, Mars, Jupiter, and Saturn, since they are not only bright in both wavelength regions but are also almost point sources for our 55" beam. This last feature means that the beam center can be easily determined.

With the 45° flat in the photometer head out of the beam, the 1 mm beam center is found by observing the output of the lock-in amplifier while moving the telescope. The strip chart connected to the lock-in amplifier output makes

this task easier. When the 1 mm signal peak is found, the telescope is then moved to this position and the 45° mirror is inserted into the beam. The light from the object is now reflected into the television camera. An adjustable reticle located in the photometer head is then moved so that the cross hairs are centered on the left-hand image. For the rest of the observing run any object centered in the cross hairs will also be centered in the signal 1 mm beam.

The 45° mirror is next moved out of the beam and the phase control on the synchronous demodulator and the telescope focus are set to provide a maximum 1 mm signal. The telescope is then nodded into the reference beam. If the signal becomes negative, all is well. If the signal merely drops to zero, the object was centered in the reference rather than the signal beam. The phase on the synchronous demodulator should be changed by 180° and the signal beam located by moving the telescope and inspecting the strip chart as before.

The chopper frequency is also set at this time; the frequency was chosen to give the highest signal to noise. In practice, using the Cornell ^{3}He bolometer dewar and with average atmospheric noise, this frequency was around 10 Hz. In order to eliminate any sort of beating with the 60 Hz mains the frequency was set to some odd number, such as 11 Hz.

2) Observing a standard: Before any set of observations it is necessary to observe some millimeter standard so

that the atmospheric transmission and instrumental sensitivity can be determined. The primary standards for this purpose are the planets, since their 1 mm brightness temperatures have been measured by Werner et al. (1978). Other secondary standards can be used when planetary observations are impossible. These standards will be discussed in more detail shortly. In general, measurements of a standard source are made approximately every 45 minutes, or even more frequently when the atmosphere appears to be unsettled. In addition, readings of the water vapor using the Westphal meter are made once every hour that the sun is up.

3) Observations of the object: Determining accurate telescope pointing is the first step in observing a millimeter object. The easiest way to do this is to offset point from a bright star that is close to the position of the millimeter object. With the 45° mirror in the beam the left-hand image of the star is lined up in the reticle cross hairs. The telescope control computer is given commands that update the position readout to match the precessed catalogued position of the bright star being observed. After these corrections have been made, the telescope is set on the precessed position of the millimeter object. Finally, after the telescope is correctly positioned, the 45° mirror is moved out of the beam and integration is started.

During any observing trip step 1 is done once (or maybe twice to check that it was done correctly the first time) at the beginning of the run. The other steps are done with

each new object. If the integrations on an object will be particularly long, step 2 may be done a few times in the middle of the integration run to check for weather changes.

Millimeter Flux Standards

Since the atmospheric effects are so large at 1 mm, extraterrestrial objects are needed for absolute flux calibration standards. This poses a problem, since both the temperature and emissivities of astronomical objects are unknown. For the 1 mm results reported here we have used the planets Venus, Jupiter, and Saturn as our primary standards. The 1 mm brightness temperatures of these bodies were taken from Werner et al. (1978). In this paper, the reported temperatures were all derived from measurements of the planets against the planet Mars. The 1 mm brightness temperature of Mars was calculated from Mariner 9 results using the thermal model of Wright (1976). Recently, there has been evidence that this model may be incorrect (Forrest, 1980). Taking this into account, we have adopted the values shown in Table 4-1 for the 1 mm brightness temperatures of the planets.

When the planets were observed, corrections had to be made to correct for the partial resolution of the planetary disk by the beam. This correction is given by the formula

$$S_o = S_p \frac{\sigma^2}{d^2} \left[1 - e^{-d^2/\sigma^2}\right] \qquad (4.6)$$

Table 4-1

Calibration Standards

Primary standards

Object	1 mm brightness temperature (°K)
Venus	276 ± 31
Jupiter	168 ± 19
Saturn	145 ± 16
Uranus	87 ± 11

Secondary standards, derived fluxes

Object	1 mm Flux (Jy)	Primary Standard
NGC 7027	5.8 ± 0.8	Saturn
3C84 (Dec. 7, 1979)	53.2 ± 6.1	Jupiter
(Dec. 7, 1979)	41.2 ± 6.7	Saturn
(Dec. 30, 1979)	41.1 ± 6.7	Jupiter
(Feb. 29, 1980)	50.9 ± 5.8	Venus
(Mar. 29, 1979)	63.2 ± 7.5	Venus
(Mar. 29, 1979)	56.8 ± 8.4	Saturn

Note: The measurements of 3C84 made against Saturn were actually made against NGC 7027, but the calibration of NGC 7027 came from Saturn.

where S_o is the observed flux from the planet, S_p is the actual flux from the planet, d is the semidiameter of the planet in arc seconds, and σ is related to the FWHM of the beam shape by

$$\sigma = \frac{FWHM/2}{\sqrt{\ell n\ 1/2}} \qquad (4.7)$$

These standard sources are then used to calibrate other bright objects, such as 3C84 and NGC 7027 so that they can be used as secondary standards. During the period of these observations, 3C84 began to flare. The fluxes measured from 3C84 during the different field trips are therefore listed separately in Table 4-1. The 1 mm flux measured for NGC 7027 was in good agreement with previous values from Elias et al. (1978). Since the temperature of Mars varies throughout the year, it was also measured separately against one of the giant gas planets on each field trip that it was used as a calibration source.

Data Reduction

As was noted above, data from faint sources was generally taken in blocks of 16 pairs of integrations. This data was reduced in the following way. First, the strip chart recorder output was carefully scanned and any obvious noise spikes were removed from the data base. The cleaned data was then reduced by dividing out the atmospheric effects using the Q's described in Appendix C. Typically runs of four blocks of 16 pairs each were sandwiched between

calibration observations of primary or secondary standards.

After cleaning and correction for atmospheric effects, the data from the four blocks was then averaged together, and a mean and statistical error computed. The resulting number was then expressed as a fraction of the cleaned and corrected signal from the calibration runs from the standard. Multiplying this fraction against the 1 mm flux from the standard then gives the 1 mm flux from the object.

Chapter 5

1 mm Observations of Extragalactic Thermal Sources

Introduction

The extragalactic thermal sources that could be expected to be detected at 1 millimeter with today's technology are either spiral, irregular, or class II Seyfert galaxies. Elliptical galaxies have little gas and dust compared to spiral galaxies and their synchrotron emission is relatively weak. As a result, no elliptical galaxy is expected to be detectable at 1 mm using present instrumentation.

Some spiral galaxies do have enough 1 mm flux to be detected with our ^{3}He detector. For normal spiral galaxies the 1 mm radiation due to dust emission is stronger than the synchrotron or thermal bremstrahlung emission. This can be seen by examining the spectrum of NGC 253, a typical spiral galaxy, shown in Figure 5-1a.

Seyfert galaxies have been divided into two classes on the basis of the width of their forbidden emission lines (Khachikian and Weedman, 1971, 1974). There is a fundamental difference in the infrared emission of the two classes. The infrared radiation from the class II Seyferts is thought to arise predominantly from thermal emission from dust grains, while the infrared radiation from class I Seyferts is due to the same non-thermal mechanism that is responsible for the observed short wavelength radio emission (Neugebauer et al., 1976). Both types of Seyfert galaxies

have been observed at 1 mm in the past, with only class I Seyferts being detected (Elias et al., 1978; Hildebrand et al., 1977).

Observations

This study reports observations of 8 spiral galaxies, M 82, and NGC 1068. These galaxies were selected on the basis of the following criteria. First of all, the galaxies were selected so that their nuclear regions would fill, or nearly fill, the 1' beam. In addition, edge on galaxies were favored because of the greater path length through their galactic disks. Finally, the galaxies that had been observed at other wavelengths, especially in the far infrared and in CO, were favored.

The observations were carried out at the 5 m Hale telescope at Mount Palomar and the 4 m Anglo-Australian telescope at Siding Springs. In order that the water vapor content of the atmosphere be as low as possible, the observations were made during local winter. The weather at the 4 m telescope during observations of NGC 253 was only marginal, with 5 mm of precipitable water vapor and a high level of sky noise due to an advancing frontal system. The observations at Mount Palomer reported here were made during good to excellent weather conditions.

The positions of the galactic nuclei were measured from Palomar Sky Survey plates, or in some cases, were taken from Dressel and Condon (1976). The positions of the galactic nuclei are given in Table 5-1. Three positions in M 82 were

observed, the nuclear position and points 1' on each side of the nucleus along the plane of the galaxy.

The results of the observations of the galaxies are shown in Table 5-2. Two different errors are shown in this table. The errors associated with the fluxes are the total uncertainties in the fluxes, including statistical errors in the observations of the object and millimeter standards, as well as uncertainties in the 1 mm flux of the standards. The errors listed in column 6 are statistical errors from the observations of the object only, expressed as Signal/RMS Error. Due to uncertainties in the observations of the standards and the uncertainty in the known fluxes of these standards, these errors are smaller than the total errors given in column 5.

Millimeter and Submillimeter Galactic Spectra

i) Temperatures: By combining the 1 mm continuum observations with shorter wavelength data, it is possible to estimate the dust temperatures and gain information about the grain composition. This information will be needed to estimate the dust masses of the galaxies.

As a first approximation, the submillimeter spectra can be fit with curves of the form

$$F(\nu) = \varepsilon(\nu)B(\nu, T) \qquad (5.1)$$

where $B(\nu, T)$ is the Planck blackbody function and $\varepsilon(\nu)$ is of the form

Table 5-1

Nuclear Positions

Object	RA (1950)	Dec (1950)
M 82 nucleus	9 h 51 m 45.6 s	69° 55' 17"
1' NE	9 h 51 m 55.7 s	69° 55' 47"
1' SW	9 h 51 m 35.5 s	69° 54' 47"
NGC 253	0 h 45 m 04.3 s	-25° 33' 46"
NGC 891	2 h 19 m 21.5 s	42° 06' 55"
NGC 925	2 h 24 m 14.5 s	33° 21' 13"
NGC 1068	2 h 40 m 05.3 s	-00° 13' 44"
NGC 4244	12 h 15 m 00.7 s	38° 05' 06"
NGC 4631	12 h 39 m 43.7 s	32° 48' 50"
NGC 5907	15 h 14 m 36.8 s	56° 30' 17"
NGC 6946	20 h 33 m 45.8 s	59° 58' 36"
IC 342	3 h 41 m 54.6 s	67° 56' 33"

Table 5-2

Observations

Object 1	Dates Observed 2	Telescope 3	Standard(s) 4	Flux(Jy) 5	Sigma 6
M 82 nuc	3/29, 3/31 (1980)	5 m	Mars, 3C84	1.98 ± 0.34	6.4
1' NE	3/29 (1980)	5 m	3C84	0.17 ± 0.43	<1
1' SW	3/29, 3/31 (1980)	5 m	Mars	-0.22 ± 0.55	<1
NGC 253	8/11 (1979)	4 m	Uranus	2.25 ± 1.05	2.3
NGC 891	12/8 (1979), 3/31 (1980)	5 m	3C84	0.03 ± 0.25	<1
NGC 925	2/29, 3/28, 3/30 (1980)	5 m	3C84	0.03 ± 0.27	<1
NGC 1068	12/6, 12/7 (1979)	5 m	3C84	0.27 ± 0.33	<1
NGC 4244	4/2 (1980)	5 m	Mars	0.07 ± 0.33	<1
NGC 4631	12/4, 12/5, 12/9 (1979)	5 m	Sat, Jup	0.74 ± 0.18	4.8
NGC 5907	1/2 (1980)	5 m	NGC 7027	0.10 ± 0.43	<1
NGC 6946	12/6, 12/7, 12/8 (1979); 1/1, 3/27, 3/28, 3/29, 3/30, 4/3 (1980)	5 m	NGC 7027	0.21 ± 0.12	2.4
IC 342	3/28, 3/29, 3/30	5 m	3C84, Venus	-0.34 ± 0.34	<1

Table 5-2 (cont'd)

Column 1: Object name

2: Dates of observations

3: Telescope used in observation; either 5 m Hale telescope or 4 m Anglo-Australian telescope

4: Standards used for calibration of 1 mm flux from galaxy

5: Measured 1 mm flux in 10^{-26} W/m^2Hz; errors are total uncertainty in flux

6: Statistical significance of observations of galaxy; see text for more details.

Figure 5-1a: Spectrum of NGC 253 from 1 GHz to 10^5 GHz, including the 1 mm measurement from this work. Fitted curve is explained in text. Radio points are from Haynes et al. (1975). Far infrared points are from Telesco and Harper (1980), Rieke and Low (1972), and Hildebrand et al. (1977). The 1 mm point is indicated by a triangle.

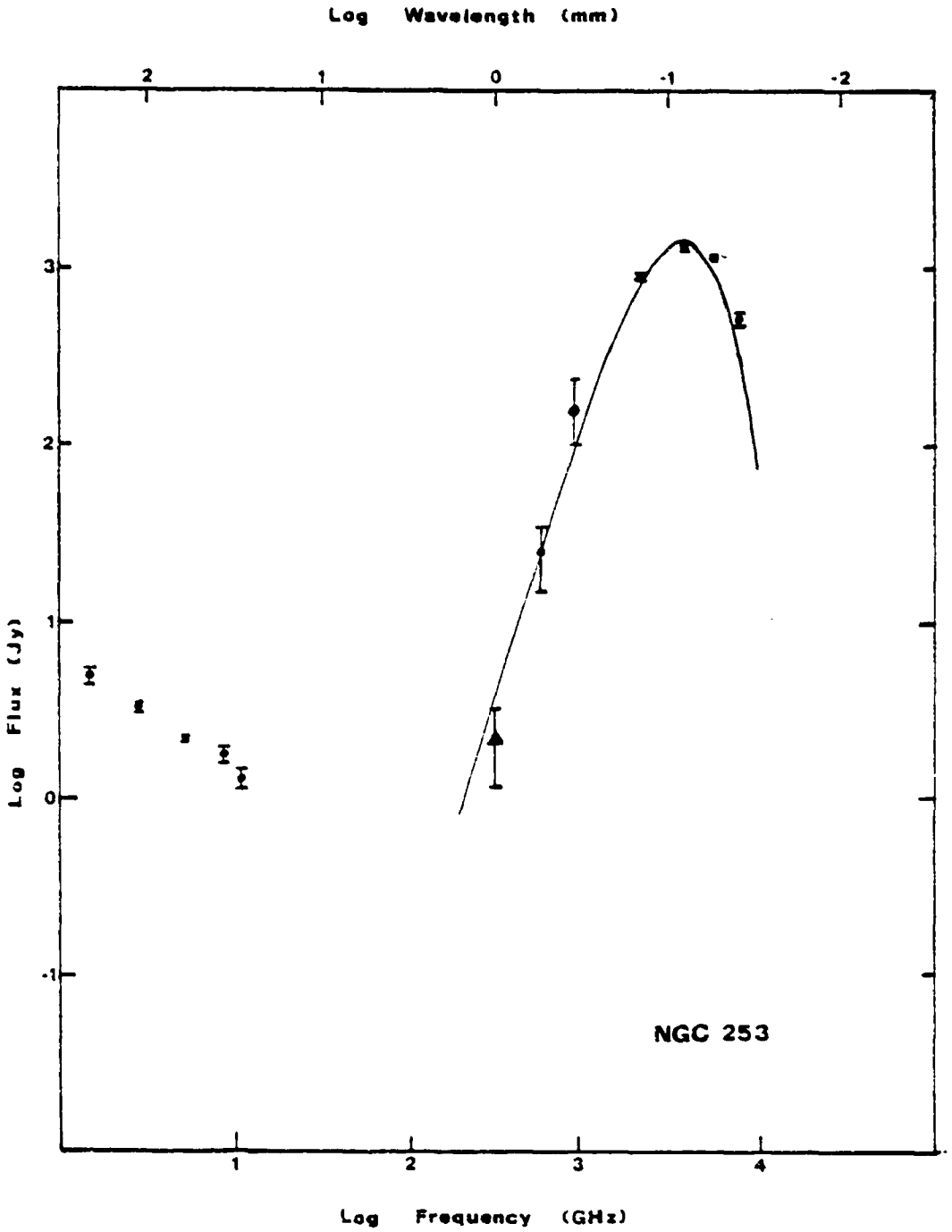
Log Wavelength (mm)
2
1
0
-1
-2
3
2
1
0
-1
Log Flux (Jy)
1
2
3
4
Log Frequency (GHz)
NGC 253

Figure 5-1b: Spectrum of NGC 1068 from 1 GHz to 10^5 GHz, including the 1 mm 3σ upper limit from this work. The fitted curve has an emissivity index of 2, the dotted line corresponds to an emissivity index of 1.5. The radio points are from Haynes et al. (1975) and Dent and Balonek (1980). The far infrared points are from Hildebrand et al. (1977) and Telesco and Harper (1980).

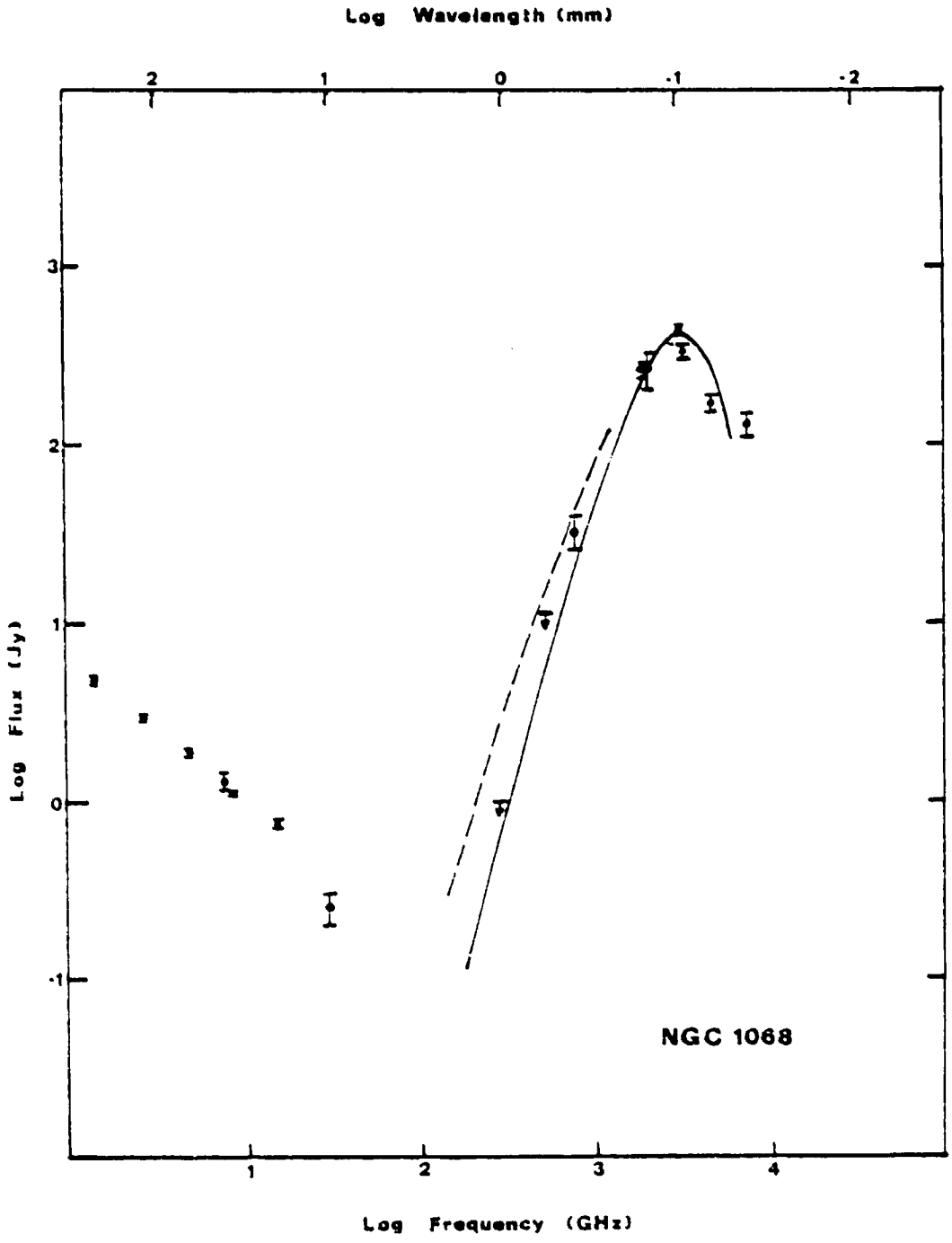
Log Wavelength (mm)
2
1
0
-1
-2
3
2
1
0
-1
Log Flux (Jy)
1
2
3
4
Log Frequency (GHz)
NGC 1068

Figure 5-1c: Spectrum of NGC 4631 from 1 GHz to 10^5 GHz, including the 1 mm measurement from this work. The radio points are from Haynes et al. (1975). The 1 mm point is indicated by a triangle.

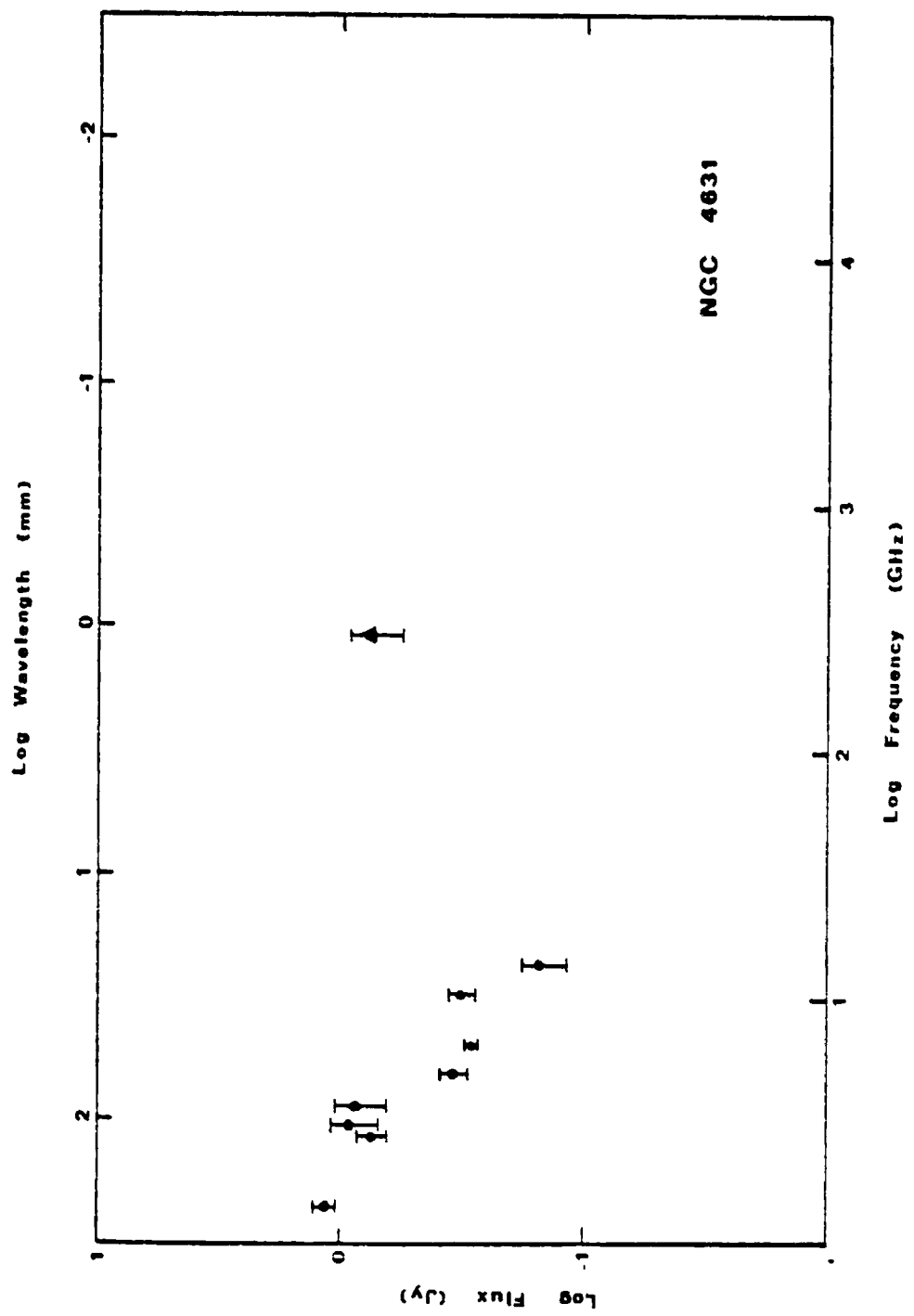
NGC 4631
Log Wavelength (mm)
Log Frequency (GHz)
Log Flux (Jy)
-2
-1
0
1
2
3
4
1
0
-1

Figure 5-1d: Spectrum of NGC 6946 from 1 GHz to 10^5 GHz, including the 1 mm measurement from this work. The fitted curve is explained in the text. The radio points are from Haynes et al. (1975). The far infrared points are from Telesco and Harper (1980). The 1 mm point is indicated by a triangle.

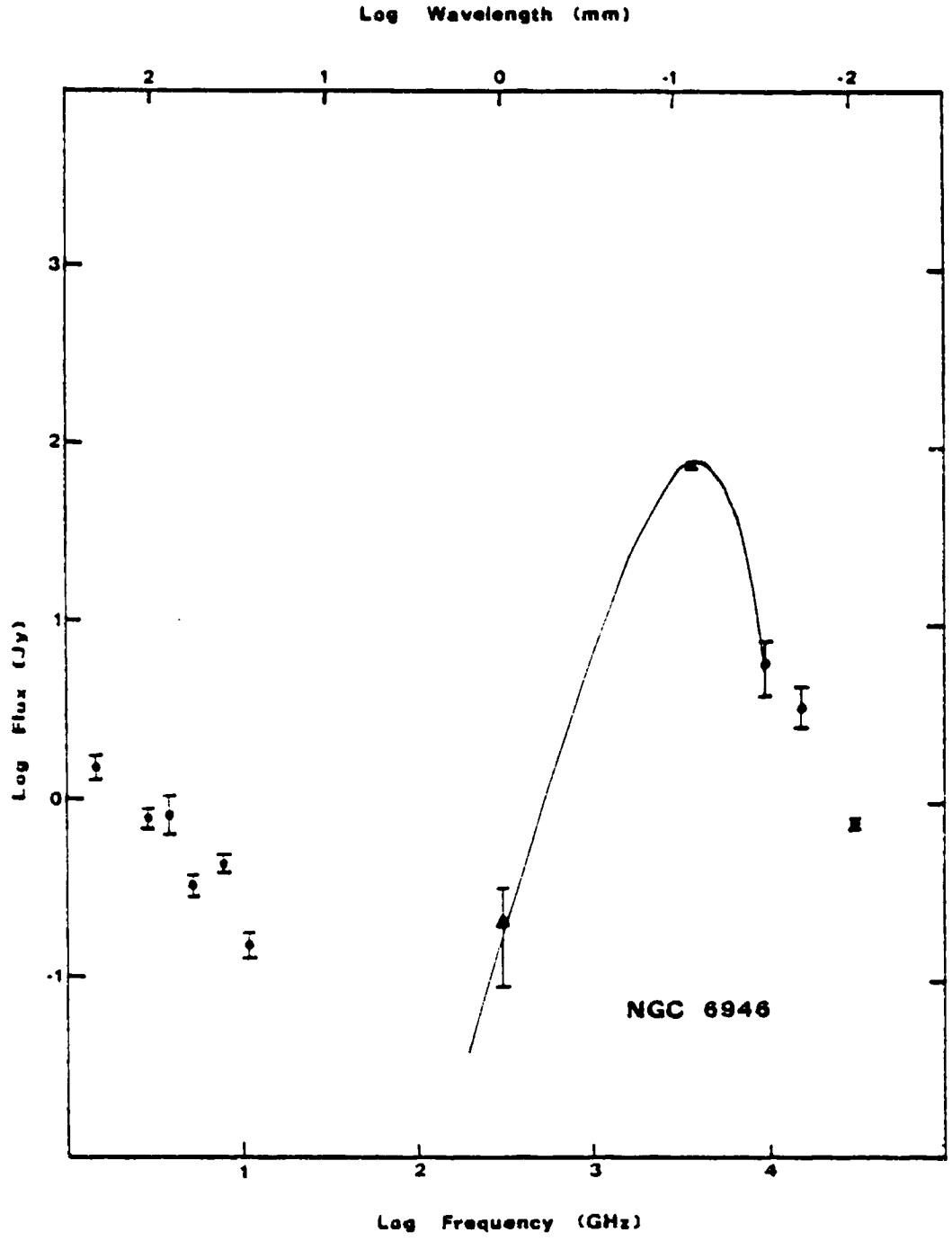
Log Wavelength (mm)
2
1
0
-1
-2
3
2
1
0
-1
Log Flux (Jy)
1
2
3
4
Log Frequency (GHz)
NGC 6946

Figure 5-1e: Spectrum of M 82 from 1 GHz to 10^5 GHz, including the 1 mm measurement from this work. The fitted curve is explained in the text. The radio points are from Haynes et al. (1975) and Dent and Balonek (1980). The far infrared points are from Telesco and Harper (1980). The 1 mm point is indicated by a triangle.

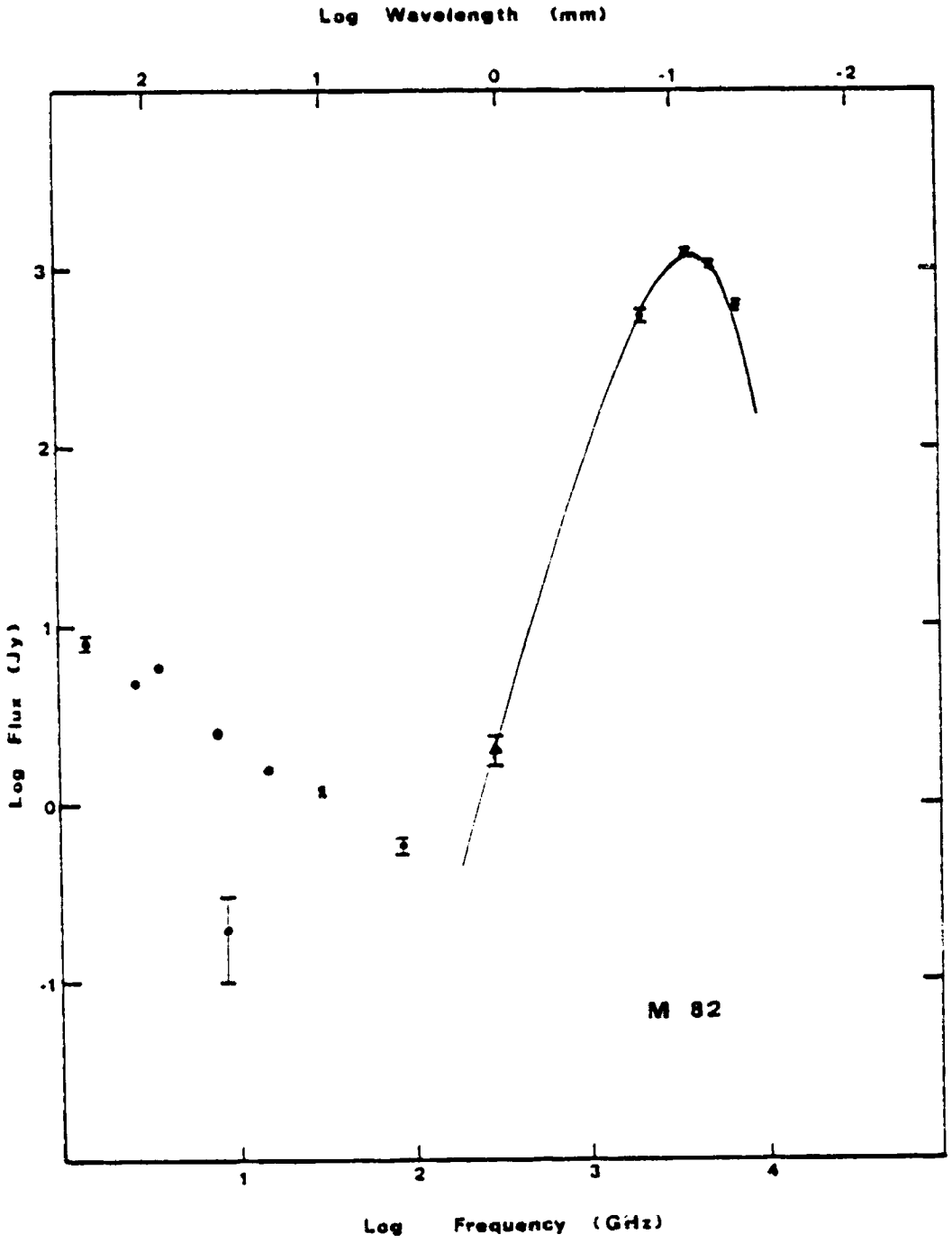
Log Wavelength (mm)
2
1
0
-1
-2
3
2
1
0
-1
Log Flux (Jy)
1
2
3
4
Log Frequency (GHz)
M 82

Figure 5-1f: Spectrum of IC 342 from 1 GHz to 10^5 GHz, including the 1 mm measurement from this work. The fitted curve is explained in the text. The radio points are from Haynes et al. (1975). The far infrared points are from Becklin et al. (1980).

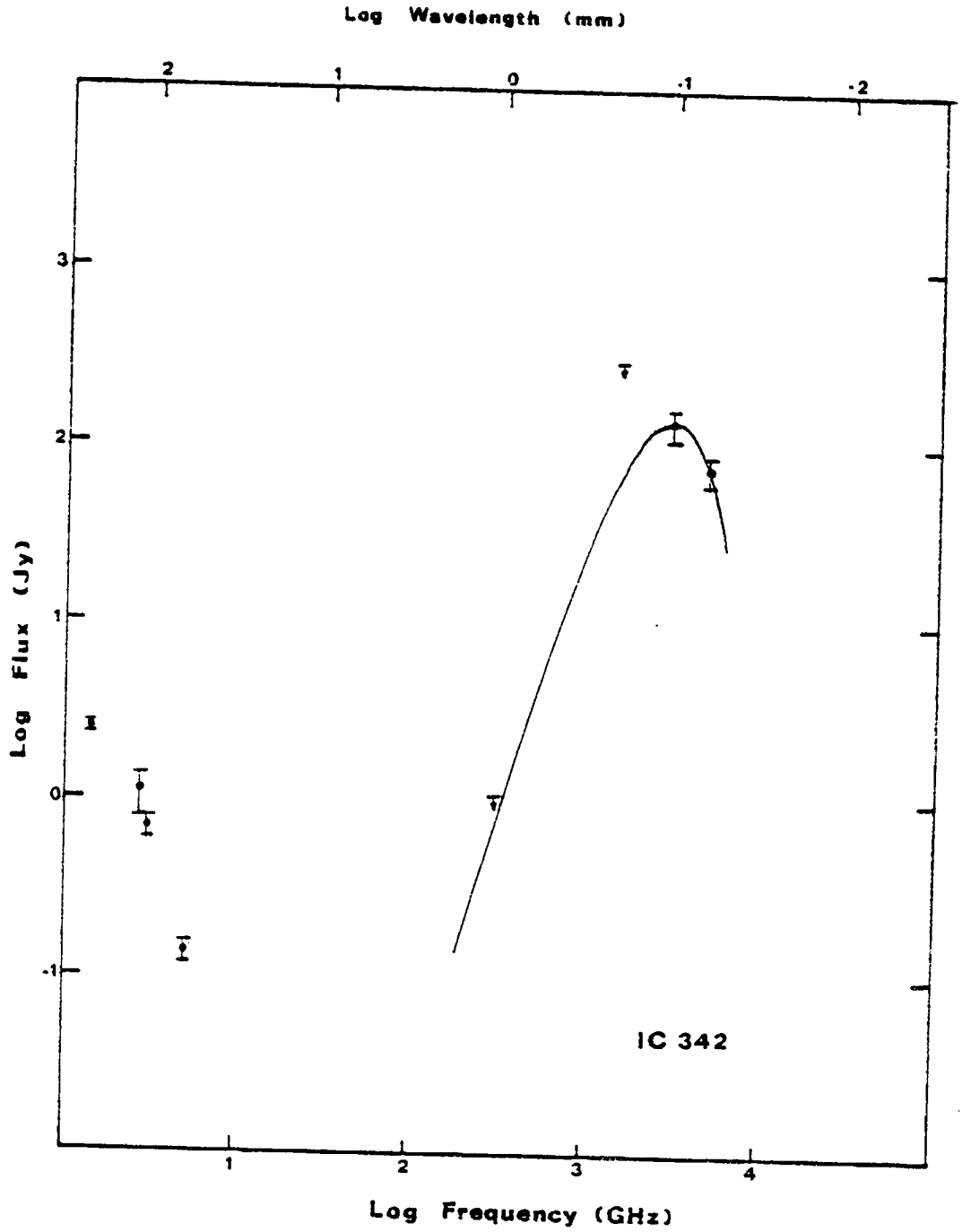
Log Wavelength (mm)
2
1
0
-1
-2
3
2
1
0
-1
Log Flux (Jy)
IC 342
1
2
3
4
Log Frequency (GHz)

$$\varepsilon(\nu) = K\nu^{P}. \qquad (5.2)$$

P will be defined as the emissivity index for the rest of this work. Curves of this form have been fit to the observations of M 82, IC 342, NGC 253, NGC 6946, and NGC 1068. These curves have been plotted in Figures 5-1a, b, c, d, e, and f. The relevant curve parameters are given in Table 5-3. For the other galaxies in our study no far infrared results have been published.

Table 5-3

Isothermal Dust Model Parameters

Object	T_d (°K)	P
M 82	46	1.5
NGC 253	41	1.5
NGC 6946	43	1.5
NGC 1068	33	2.0
IC 342	32	1.5 (assumed)

The observations at wavelengths around 100 μm are most useful in determining the blackbody temperatures, while the longer wavelength observations out to 1 mm are better for determining the value of p. Observations at wavelengths longer than 1 mm are not very useful for studies of the

dust, since the flux becomes so small that detection is very difficult. In addition, at these long wavelengths disentangling the thermal flux from the non-thermal synchrotron flux is a thorny problem.

For the galaxies M 82, NGC 253, and NGC 6946 the best fit curves have blackbody temperatures of around 40°K and $\varepsilon(\nu)\alpha\nu^{1.5}$. There is not enough data to accurately determine the value of the emissivity index for IC 342. A value of 1.5 was therefore chosen so that a dust temperature estimate could be made. NGC 1068 was fit best by a curve with $\varepsilon(\nu)\alpha\nu^{2}$, implying a fundamental difference between this galaxy and the other galaxies in the study.

The dust responsible for the 1 mm emission from spiral galaxies could exist in three different environments. The hottest environment (defined here as Region I) would be in molecular clouds with embedded stellar or protostellar sources. The dust temperature in these clouds has been calculated to range between 15°K and 100°K, depending on the cloud parameters and the location of the dust in the cloud (Leung, 1976). Temperatures of this order have been observed in such clouds in our galaxy (Thronson and Harper, 1979). Dust in interstellar space (Region II) would have an intermediate temperature. The equilibrium temperature of unshielded grains in the interstellar medium of a galaxy depends strongly on the grain composition. The equilibrium temperatures for our Galaxy have been estimated to range from 10°K (silicates, Aannestad, 1975) to 40°K (graphite,

Werner and Salpeter, 1969). The coldest environment is inside dense dark molecular clouds (Region III). The grain temperatures in such clouds have been estimated to be less than or equal to 7°K (Leung, 1975). The thermal emission from the dust in these clouds would be very difficult to detect, since the dust temperature is not much greater than the 3°K cosmic background.

By combining the far infrared, submillimeter, and millimeter observations from a galaxy, we can determine the relative amounts of dust in Regions I and II. Subtracting the spectrum of an average hot molecular cloud from the spectrum of a galaxy will leave the contribution due to the dust in the colder environments. The average spectral index between 340 μm and 1 mm for the molecular clouds measured by Westbrook et al. (1976) is 3.18. This can be compared with the spectral index of our galaxies between 340 μm and 1 mm. Unfortunately, only one galaxy, NGC 253, has been reported to have been detected at 340 μm (Harper and Low, 1973). As a result, the 340 μm flux can only be interpolated from our curves in Figure 5-1 for the other galaxies we have detected. When this is done, the average value of the spectral index from 340 μm to 1 mm for M 82, NGC 253, and NGC 6946 is 3.29. The close similarity of this value with the average value for the molecular clouds implies that almost all the 1 mm radiation from spiral galaxies is emitted in hot molecular clouds. This means that substantial quantities of dust outside of these clouds and at interstellar tempera-

tures (around 15°K) are effectively ruled out. Since a dust cloud at 7°K would emit very little radiation, our results do not set such stringent constraints in the quantity of dust in cold molecular clouds.

ii) Grain composition: If the dust grains are all at the same temperature, the observed value of the emissivity index puts constraints on the grain composition. Aannestad (1975) has measured the absorptive properties of various silicate grain materials, both with and without ice mantles. Of the various materials, only fused quartz, with an emissivity index of 1.6, is close to our derived value of 1.5. Other silicates or silicates with icy mantles have emissivity indices of 2 or higher. Phillip (1977) has made a similar study of graphite grain emissivities. His results for pure graphite grains give an emissivity index of 3 for wavelengths longer than 100 μm.

It should be noted that this problem also exists in explaining the results from hot molecular clouds, since they also have emissivity indices of around 1.5 (Westbrook et al., 1976; Werner et al., 1975; Ade et al., 1974). For these clouds the low value of the emissivity index is thought to be due to the temperature gradient that exists through the clouds. The flux contributions of the colder dust located at the outside edges of the clouds brings the emissivity index down to a lower value than would be indicated by the grain emissivity alone. In order to estimate the amount of dust and the temperature variations that would be required, let us assume that the dust in hot molecular clouds has an

emissivity index of 2.5. This is slightly above the average for silicates or core-mantle ice silicates, but is well within the range of indices for the different silicate materials proposed for interstellar dust. Since the $\varepsilon\alpha\nu^{1.5}$ curves fit the galaxies so well, let us also assume that this expression is exactly true. This means that the spectral shape of the dust emission is given by:

$$F(\nu)\alpha \frac{\nu^{4.5}}{e^{h\nu/kT_c} - 1} \tag{5.3}$$

where T_c is the color temperature of the dust, h is Planck's constant, and k is Boltzmann's constant. Now the low frequency tail of this expression can be approximated by

$$F(\nu)\alpha \int_{T_o}^{T_c} \frac{\nu^{5.5}}{e^{h\nu/kT} - 1} C(T)dT \ , \tag{5.4}$$

corresponding to our assumed dust emissivity index of 2.5. The function C(T) gives the distribution of dust mass as a function of temperature. We can find an upper limit for T_o in the following way. If equation (5.3) is plotted on a log $F(\nu)$ - log ν plot, the slope at a frequency ν will be given by:

$$4.5 - \frac{x}{1 - e^{-x}} \tag{5.5}$$

where $x = h\nu/kT_c$. Similarly the slope of

$$\frac{\nu^{5.5}}{e^{h\nu/kT} - 1} \tag{5.6}$$

on the same plot is given by:

$$5.5 - \frac{x}{1 - e^{-x}} \, . \tag{5.7}$$

If the average hot molecular cloud has a color temperature of 40°K, then equation (5.5) gives a slope of 3.3 at 300 GHz (1 mm), the lowest frequency measurement of the dust. In order for equation (5.7) to equal this value for the slope at 300 GHz, the temperature must run from 40°K down to 8°K or less.

Of course, the actual submillimeter and millimeter observations of hot molecular clouds are not accurate enough to set such precise temperature limits. Even assuming a lower limit to the temperature of 15°K, we can obtain excellent fits to our results. In order to realistically estimate the amount of colder $\varepsilon\alpha\nu^{2.5}$ dust needed to fit the observations of our galaxies, we will assume that the dust is only at two temperatures, T_c and 15°K. A temperature of 15°K is not as arbitrary as it may seem, since this is roughly the lower end of the range of temperatures expected in a hot molecular cloud (Leung, 1976). We will therefore fit the galactic spectra to

$$F(\nu) = C_1\nu^{2.5} \, B(\nu, 15°K) + C_2\nu^{2.5} \, B(\nu, T_c) \tag{5.8}$$

where C_1 and C_2 are different constants for each galaxy. When this is done, the parameters given in Table 5-4 are derived. These results indicate that our model requires roughly 20 times as much 15°K dust as color temperature dust in order to fit the spectra. It is important to remember that all of this dust would be associated with hot molecular clouds in these galaxies.

Table 5-4

Two Temperature Dust Model

Galaxy	T_c (°K)	C_1/C_2
NGC 253	34	12
NGC 6946	35	25
M 82	82	24

For simplicity, in our derivations of dust masses we will assume all of the dust is at an average temperature of 20°K in the spiral galaxies. If the actual dust temperatures are closer to the color temperatures given in the isothermal model earlier, it will only lower our dust mass estimate by a factor of 2. Since the value of p is higher for NGC 1068, we will use the color temperature for this galaxy. The reader should keep in mind that the dust masses that will be derived will actually be lower limits, since very low temperature dust is being underrepresented.

Dust Masses

One mm observations of galaxies are particularly useful in estimating dust masses. We have seen that the 1 mm

emission is due to thermal radiation from dust at 15-40°K. Since 1 mm wavelengths are on the Rayleigh-Jeans tail of the blackbody curve, the expression for the flux received from an extended source becomes:

$$F(\nu) = B(\nu, T_d)\Omega\ \tau(\nu) \tag{5.9}$$

$$\approx 2k\,T_d\,(\nu^2/c^2)\Omega\ \tau(\nu) \tag{5.10}$$

where $B(\nu, T_d)$ is the blackbody function, T_d the dust temperature, Ω the effective beam size, and $\tau(\nu)$ the optical depth.

For a collection of spherical dust grains of number density n the optical depth can be expressed as

$$\tau(\nu) = \int n\pi a^2 Q(\nu) d\ell. \tag{5.11}$$

In this expression a is the grain radius, $Q(\nu)$ is the absorption efficiency, and $d\ell$ is an increment of path length. For grains of density ρ

$$\tau(\nu) = D\ \frac{3}{4}\ \frac{Q(\nu)}{a\rho} \tag{5.12}$$

where D is the dust mass column density.

For an optically thin, isothermal dust region the flux from any part of the region can be expressed as

$$F(\theta,\phi) = An(\theta,\phi)dw \tag{5.13}$$

where A is a constant, and $n(\theta,\phi)$ is the number column density at that position (see Figure 5-2). The signal received

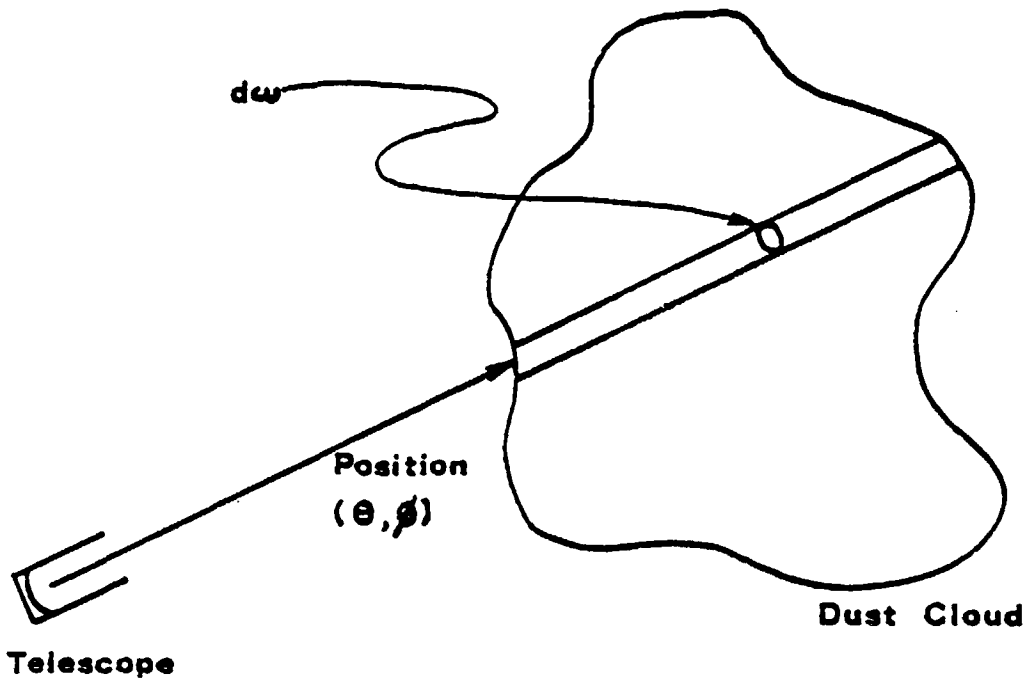

Figure 5-2: Diagram used for derivation of 1 mm flux.

by the telescope is given by

$$Fr = \int A' n(\theta,\phi) R(\theta,\phi) d\Omega \qquad (5.14)$$

where A' is a constant and $R(\theta,\phi)$ is the telescope beam response. We can define an average column density from

$$\bar{n} \equiv \frac{Fr}{A' \int R(\theta,\phi) d\Omega} \quad . \qquad (5.15)$$

Now for a Gaussian beam with a FWHM of 55",

$$\Omega' \equiv \int R(\theta,\phi) d\Omega = 8 \times 10^{-8} \text{ ster}, \qquad (5.16)$$

and corresponds to an effective beam diameter of 66". Combining all of these equations we find

$$\bar{D} = \frac{2\, Fr(\nu)}{3k\, T_d \Omega'} \frac{a\rho}{Q(\nu)} \quad , \qquad (5.17)$$

defining D as the beam averaged dust mass column density.

The value of the factor $Q/a\rho$ is strongly dependent on the grain composition. The calculated and measured values for $\lambda = 1$ mm range from 6 cm^2/g ("astronomical silicate," Draine, 1980) to 10^{-2} cm^2/g (graphite, Phillip, 1977). A list of some materials that have been suggested for grain composition together with their values of $Q/a\rho$ and p is given in Table 5-5.

This uncertainty in the value of $Q/a\rho$ is the largest source of uncertainty in dust mass estimates from millimeter flux measurements. Until the composition of the dust is better known, this problem will always be present. For the

rest of this work we will assume an average silicate value of 0.05 for $Q/a\rho$ at 1 mm.

Table 5-5

Values of $Q/a\rho$ at 1 mm for Some Suggested Grain Materials

Material	$Q/a\rho$ (10^{-3} cm^2/g)	Grain Emissivity Index, p
Olivine	9.3	2.2
Fused quartz	190	1.6
Fused quartz with ice mantles	48	3
Lunar rocks	76	1.9
Pure graphite	10	3
"Astronomical Silicate"	6000	2

(From Aannestad, 1975; Phillip, 1977; and Draine, 1980.)

With this value the dust mass column density can be calculated for the galaxies using their measured fluxes together with the temperatures derived earlier. For our 66" effective beam size on the 5 m Hale telescope equation (5.17) becomes

$$D(g/cm^2) = F_{1\ mm}(Jy)/8.32\ T_d(°K) \qquad (5.18)$$

Although we will rather loosely refer to D as the mass column density, it is important to remember that this quantity has been averaged over our beam and should not be compared

directly with other studies using beams of markedly different sizes. The results of the dust mass calculations are given in Table 5-6.

Translating these dust mass column densities into total masses requires knowing the distances to the galaxies. The distances used for these calculations are from various sources and are given in Table 5-7. The total mass of dust responsible for the 1 mm flux in our 66" effective beam is then

$$M_d = D(g/cm^2)\ell^2(M_{pc})3.83 \times 10^8\ M_\odot \qquad (5.19)$$

In this equation D is the dust column density and ℓ is the distance to the galaxy. The mass totals are given in Table 5-8.

Flux Correlations

The four galaxies, M 82, NGC 253, NGC 4631, and NGC 6946, that were detected in our observations do not form a large enough sample to draw statistically significant conclusions about the 1 mm flux from spiral galaxies as a class. It should also be noted that there was a selection effect in choosing which galaxies to observe. The prime criterion was the size of the galaxy. In practice, this meant that the galaxies were all at roughly the same distance. The selection effect entered when the observed galaxies were chosen out of this group, since they were chosen because their brightness at other wavelengths suggested that they might be bright at 1 mm. Thus some of the galaxies may be

Table 5-6

Dust Mass Column Densities

Object	Dust Temperature (°K)	D (x 10^{-3} g/cm^2)
M 82	20	11.5
1' NE	20	$3\sigma < 7.6$
1' SW	20	$3\sigma < 9.7$
NGC 253	20	12.9
NGC 891	20	$3\sigma < 4.4$
NGC 925	20	$3\sigma < 4.6$
NGC 1068	[33]	$3\sigma < 3.5$
NGC 4244	20	$3\sigma < 5.8$
NGC 4631	20	4.2
NGC 5907	20	$3\sigma < 7.4$
NGC 6946	20	1.3
IC 342	20	$3\sigma < 5.9$

Due to the numerous assumptions that went into calculating the value of D, no formal errors are included. We have assumed an average dust temperature of 20°K for all of the galaxies except NGC 1068 (see text for details).

[ ]: color temperature used for this object.

Table 5-7

Galactic Distances

Object	Hubble type	Distance (Mpc)	Ref.	Diameter of 66" beam (kpc)
M 82	Ir II	3.0	1	1.0
NGC 253	Sc	3.4	2	(1.4)
NGC 891	Sb	10.0	5	3.3
NGC 925	Sc/SBc	14.8	6	4.8
NGC 1068	Seyfert	18.1	2	5.8
NGC 4244	Scd	3.8	6	1.2
NGC 4631	Sc	5.2	4	1.7
NGC 5907	Sc	4.6	6	1.5
NGC 6946	Scd	4.2	6	1.3
IC 342	Scd	4.5	3	1.4

References:

1) Tammann and Sandage, 1968

2) Sandage and Tammann, 1975

3) Baker et al., 1977

4) Krumm and Salpeter, 1979

5) Sancisi and Allen, 1979

6) Roberts, 1969

( ): Diameter of 88" effective beam of Anglo-Australian telescope

Table 5-8

Total Dust Masses

Object	Total dust mass in 66" beam (10^7 $M_\odot$)
M 82	5
1' NE	$3\sigma < 2$
1' SW	$3\sigma < 5$
NGC 253	8
NGC 891	$3\sigma < 16$
NGC 925	$3\sigma < 40$
NGC 1068	$3\sigma < 40$
NGC 4244	$3\sigma < 4$
NGC 4631	4
NGC 5907	$3\sigma < 6$
NGC 6946	0.8
IC 342	$3\sigma < 5$

unrepresentative of spiral galaxies in general.

In spite of these disclaimers, it is impossible to resist the temptation of trying to find correlations between our 1 mm results and the results at other wavelengths. Some conclusions we can draw immediately.

1) The 1 mm radiation in spiral galaxies originates in thermal radiation from dust.

2) The 1 mm points are on the Rayleigh-Jeans tail of the dust blackbody curves.

3) The 1 mm, submillimeter, and far infrared measurements yield a similar spectral shape for all the galaxies detected at 1 mm. This same spectral shape is also observed in measurements of galactic molecular clouds.

As a result of point number 3, there is close correlation between the 100 μm and 1 mm flux densities. Our results show that for a 1' beam centered on the nucleus of a galaxy the average value of $F_{100\ \mu m}/F_{1\ mm}$ is 470.

We can also attempt to find a similar correlation between the 1 mm and gas observations. The correlations with CO and HI measurements will be discussed later in the sections on the individual galaxies. An additional comparison can be made between the 1 mm emission and the total HI emission from a galaxy. Such a correlation would imply that all spiral galaxies are basically the same, with the only differences due to distance and an overall size scale factor. There are two ways to check for this. If the source of the 1 mm emission in galactic nuclei is much smaller than

the beam size then the ratio

$$\frac{F_{1\ mm}\ \ell^2}{M_{HI}} \tag{5.20}$$

should be a constant. In this expression $F_{1\ mm}$ is the 1 mm flux, M_{HI} the total mass of HI in the galaxy, and ℓ the distance to the galaxy. If the source of the 1 mm radiation is larger than the beam size, then $F_{1\ mm}/M_{HI}$ should be a constant. Using data on the total mass of HI from Roberts (1969), together with the distance estimates listed in Table 5-7, it is possible to make these comparisons. The results are shown in Figure 5-3. As can be seen in the figure, there seems to be no correlation between these quantities.

One final comparison can be made between the synchrotron emission from the galaxies and their 1 mm flux. This comparison is shown in Figure 5-4 and indicates that there may indeed be a correlation between these two quantities. If this is real, this would imply that there is some physical connection between the amount of dust and the strength of the synchrotron radiation. This would be understandable if the 1 mm emission originates in hot molecular clouds. These clouds are the sites of star formation and their numbers indicate the general level of activity in the nucleus. A high level of star formation would also lead to more supernovae which would contribute to the overall level of synchrotron radiation from the galaxy. Future 1 mm extragalactic observations should help to firmly establish this relationship.

Figure 5-3: For the galaxies observed at 1 mm the flux is plotted as a function of a) the total flux of HI divided by the square of the distance and b) the total HI mass of the galaxy only.

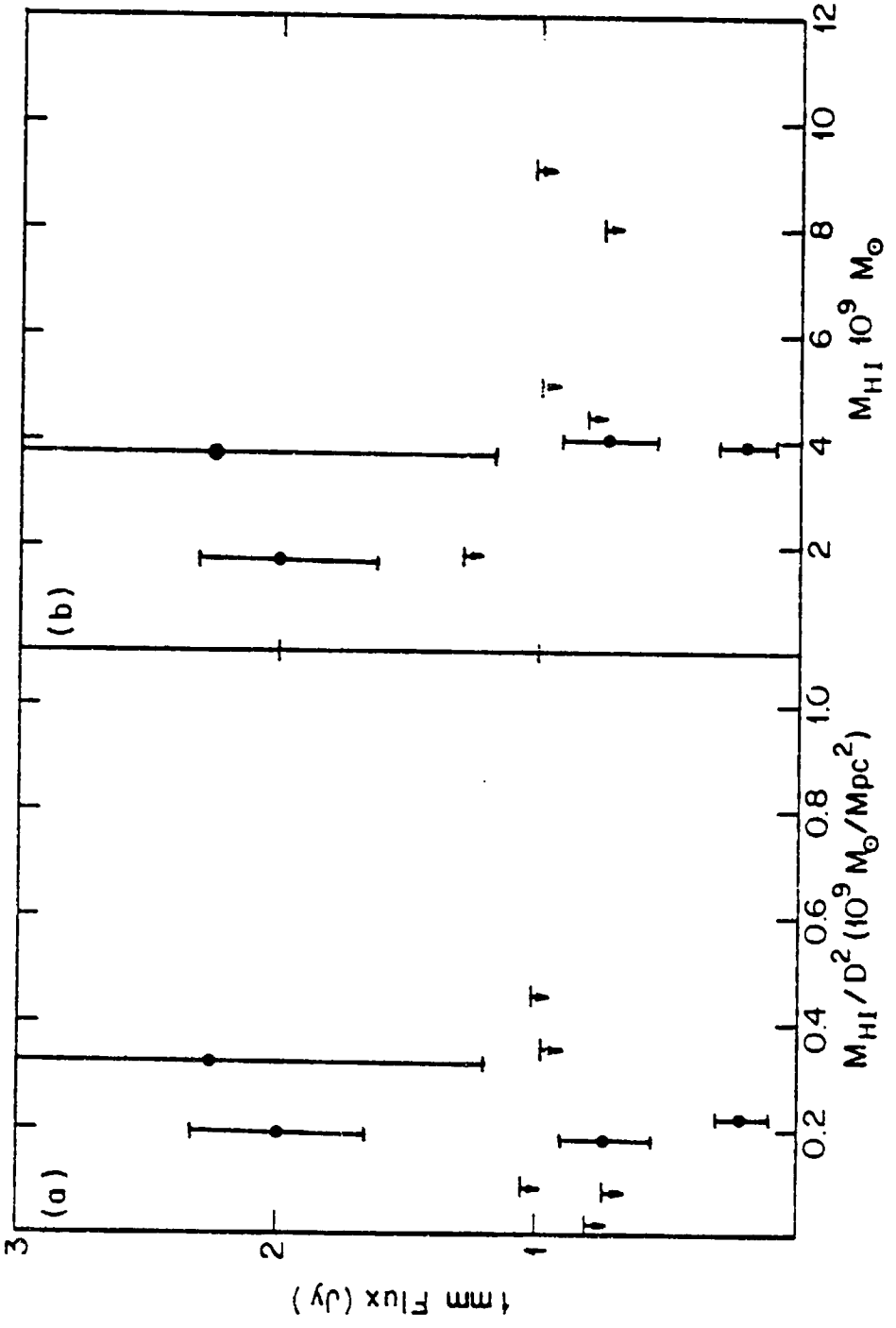
1mm Flux (Jy)
3
2
1
(a)
0.2
0.4
0.6
0.8
1.0
M_{HI}/D^2 (10^9 $M_\odot$/Mpc^2)
(b)
2
4
6
8
10
12
M_{HI} 10^9 $M_\odot$

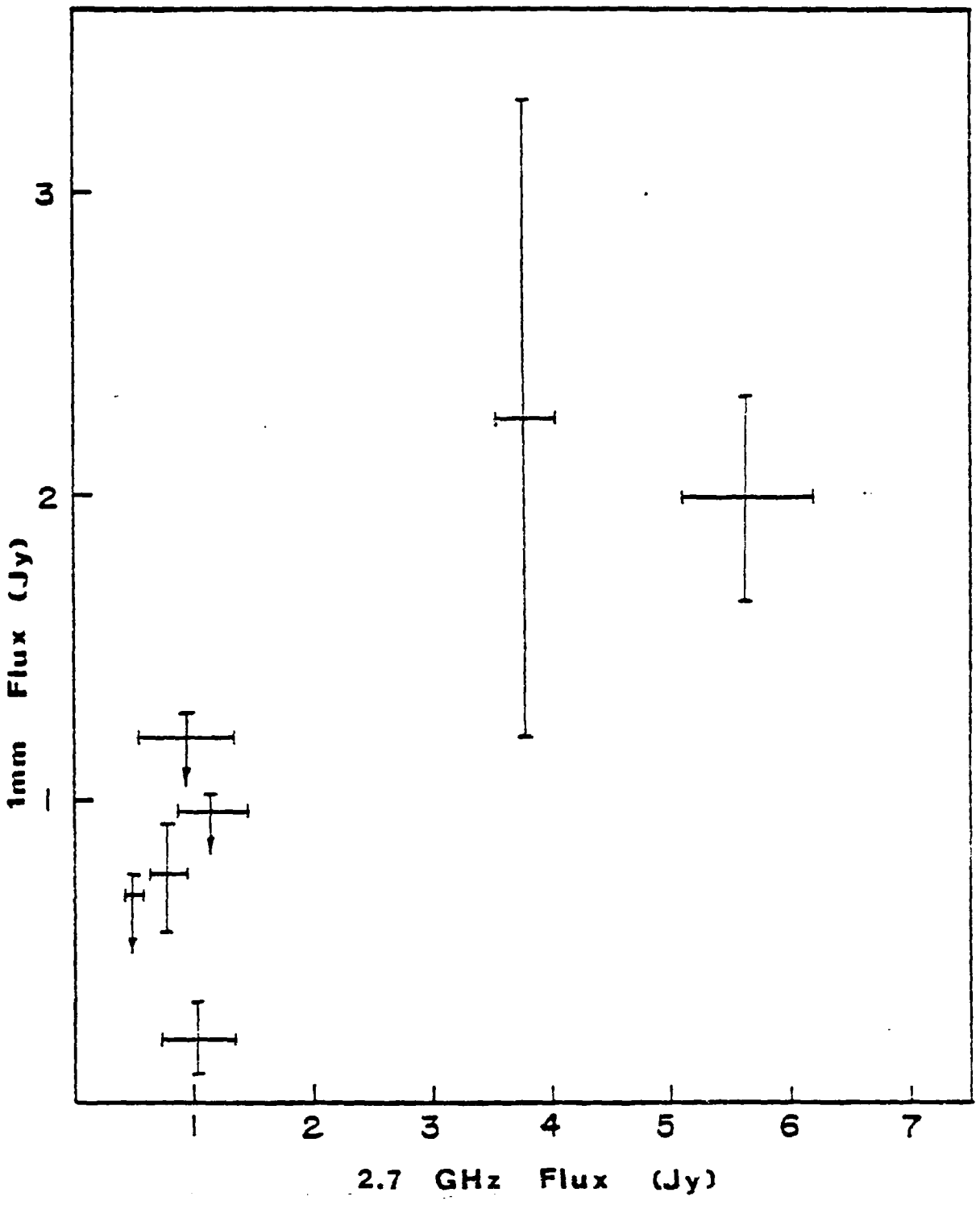

Figure 5-4: The 1 mm flux plotted against the radio continuum flux at 2.695 GHz.

Individual Objects

M 82

The 1 mm flux from M 82 was measured at three points along the galactic plane; one point centered on the nucleus and the others 1' along the plane on each side of the nucleus. The nuclear center given in Table 5-1 is the position of the peak radiation at 10 μm. Only the flux from the nuclear point was strong enough to be detected. The flux measured at this point, 1.98 ± 0.34 Jy, is in excellent agreement with previous 1 mm measurements (Elias et al., 1979 (2.7 ± 0.7 Jy)).

i) Spectrum: The nuclear region of M 82 is very bright in the infrared due to thermal radiation from dust. This dust is thought to be heated by large numbers of luminous early type stars (Telesco and Harper, 1980). Since the far infrared spectrum closely matches the spectra of galactic molecular clouds with hot embedded sources, the infrared radiation from M 82 probably arises from similar clouds. As was noted earlier, the 1 mm emission from M 82 can also be explained as originating in molecular clouds. This implies there is very little Region II dust (T_d ~ 15°K) in the galaxy.

ii) Gas measurements: M 82 has been observed in CO by Rickard et al. (1973) and in HI by Gottesman and Weliachew (1977). The beam sizes for these measurements were 65" and 3.5', respectively.

The CO beam size of Rickard et al. (1977) was very close to our 1 mm beam size, making comparisons between the two measurements very easy. In deriving their total CO column density Rickard et al. assumed a gas temperature of 26°K. We have recomputed their results using our dust derived temperature of 20°K. With this modification their total CO column density in the direction of the nucleus becomes 1.5 x $10^{19}/cm^2$. Using their value of $[CO]/[H_2] = 4 \times 10^{-5}$ for the ratio of CO to molecular hydrogen, the column density of H_2 becomes 4 x $10^{23}/cm^2$ or 1.3 g/cm^2.

The beam size of the HI measurements of Gottesman and Weliachew (1977) was too big for direct comparison with our 1 mm results. At this beam size there is no evidence of the HI hole found at the nuclear positions in many other galaxies (Krumm and Salpeter, 1979), although the peak HI emission is offset 30" to the south from the 10 μm peak. The HI peak corresponds to 1.5 x 10^{21} atoms/cm^2 or a mass column density of 9 x 10^{-3} g/cm^2. This is a factor of 140 lower than the H_2 mass column density estimated from the CO observations above. It is interesting that this ratio is so high, since estimates of the inner 500 pc of our galactic center give $[H_2]/2[H] = 30$ (Rickard et al., 1977). The cause of this discrepancy probably lies in the different beam sizes used in the measurements. Thus the total gas mass column density is close to the H_2 value.

Combining our 1 mm results with the gas measurements gives an approximate gas:dust mass ratio of 110:1. Although

this ratio is roughly equivalent to estimates for our galaxy, it must be emphasised that the value of $(\rho a/Q)$ used in calculating the dust mass column density was only a crude estimate.

iii) Scan comparisons: Since the CO beam size is so close to the 1 mm beam size, the CO and 1 mm scans can be compared directly. This is shown in Figure 5-5. The FWHM of the CO peak is 80". Since this is only slightly larger than the beam size used in the CO study, the nucleus is not really resolved. In our galaxy there is a strong correlation between 1 mm and CO emission. This correlation is also evident in our result from M 82; both the CO and 1 mm results show strong peaks in the emission at the location of the nucleus.

It is interesting to compare these results with the results from our own Galaxy. The Galactic center region has been mapped at 540 μm by Hildebrand et al. (1978) and in CO by Solomon et al. (1972). These results give 540 μm and CO source sizes of 13' FWHM (40 pc at 10 kpc). A similar size source in M 82 would be far too small to be resolved with our beam.

In M 82 the distance corresponding to the effective beam diameter (1.0 kpc) is only slightly larger than the size of the active central region defined by Soliger et al. (1977). The non-thermal radio emission from this region is similar to that from the Milky Way's galactic center region, although the central region of M 82 has a volume roughly 50 times

Figure 5-5: Plot of scans along the plane of M 82 at various wavelengths. The center of the plot is the nuclear position listed in Table 5-1. The 1 mm flux is expressed in Jy. The CO results are from Rickard et al. (1977). The 58 μm far infrared results are from Telesco and Harper (1980) and have a peak intensity of 1066 ± 44 Jy. The exact position of the 58 μm peak is not known, and the placement of the infrared scan is designed to show the size of the feature, rather than its exact location.

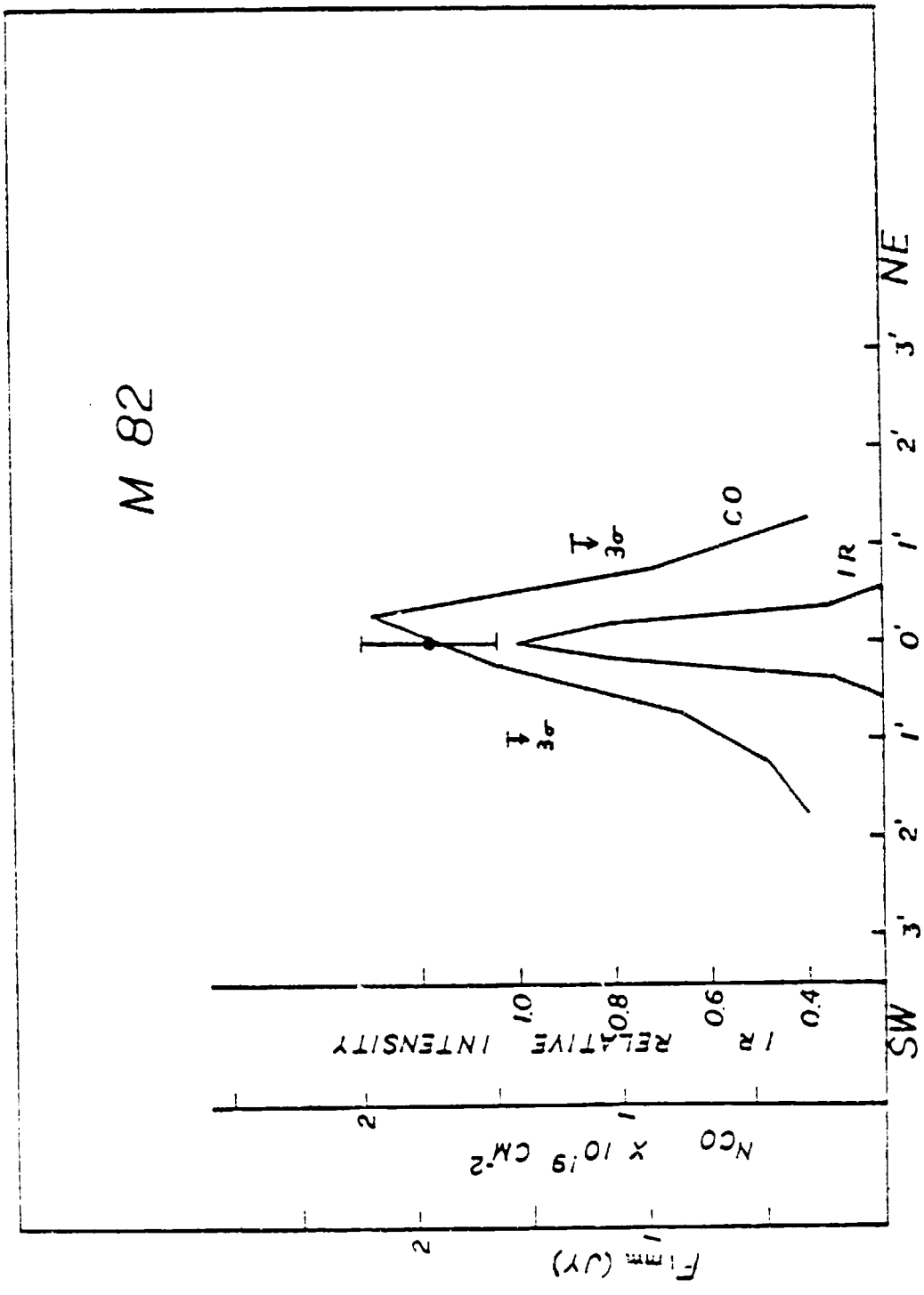
M 82
CO
IR
SW
NE
3'
2'
1'
0'
1'
2'
3'
0.4
0.6
0.8
1.0
IR RELATIVE INTENSITY
N_{CO} x 10^{19} CM^{-2}
F_{1mm} (Jy)

larger than in our galaxy (Soliger et al., 1977). If we accept the argument of Soliger et al. (1977) that the nucleus of M 82 is similar to the Galactic nucleus, only larger, we can estimate how large the 1 mm source should be. Since Soliger et al. concluded that the linear dimensions of M 82 are roughly 4 times those in our galaxy, this would correspond to a 1 mm source size of 10" at 3 Mpc.

We can give a definite value for the minimum 1 mm source size from

$$\pi \theta_{1/2}^2 \frac{2kT\nu^2}{c^2} \geq F(\nu) \qquad (5.21)$$

or

$$2\theta_{1/2} \geq 1" \qquad (5.22)$$

Telesco and Harper (1980) claim to have resolved a 37" source of 58 μm radiation in the nucleus of M 82. The 1 mm radiation could perhaps originate from the same source.

iv) Models for M 82: What kind of galaxy is M 82 anyway? Based on its appearance on photographic plates, M 82 is classified as an IrII galaxy. The earliest observations in the visible and in H_α showed a strange filamentary and knotted nucleus. Originally this appearance was explained as being due to a recent explosion in the nucleus. More recently, observations have uncovered evidence that dispute this theory. As a result, other models have been proposed to explain M 82's unusual appearance. Many of these models have been summarized by Soliger et al. (1977) and two are described below.

Gottesman and Weliachew's (1977) work in HI has shown a dynamical correlation between M 81 and M 82. They therefore proposed that a recent tidal encounter with M 81 has driven gas deeply into the nucleus of M 82. This gas caused density enhancements that resulted in a massive amount of star formation which results in large amounts of infrared emission.

A somewhat different model has been proposed by Elvius (1972) and more recently by Soliger et al. (1977). In these models M 82 is moving through a thin cloud of dust and gas associated with the M 81 system. This material is swept up and accreted into the core of M 82, causing large amounts of star formation and dust emission in the nucleus.

In view of these models it is perhaps surprising that the 1 mm results are so normal, with the estimated gas to dust ratio and far infrared spectrum similar to our Galaxy and other normal spirals. Our work shows that the large luminosity of M 82 is due to larger numbers of the same type of sources observed in other galaxies. As a result, it seems unlikely that there has been a recent massive explosion in the nucleus of M 82. Our instrument is not sensitive enough to distinguish between the two models above. Had it been more sensitive, the thin dust halo postulated in the models of Soliger et al. (1977) and Elvius (1972) could possibly be detected at 1 mm.

NGC 253

NGC 253 is classified as a Sc spiral (Sandage, 1961), showing prominent dust lanes in visible photographs. It is

also very bright in the infrared. The 1 mm flux measurements from NGC 253 are the only measurements presented in this work that were made on the 4 m Anglo-Australian telescope. As a result of this telescope's smaller size, the beam size for these measurements was 73" FWHM with an effective beam size on a uniform extended source of 88". The position of the beam center coordinates for the nucleus of NGC 253 were approximately 10" away from the 2.2 μm peak reported by Becklin et al. (1973).

i) Spectrum: The spectrum of NGC 253 including the 1 mm point is shown in Figure 5-1a. Although the single temperature fit is not as good for this object as it was for M 82, it is obvious that there is not a great deal of dust in the 10°K - 30°K temperature range outside of hot molecular clouds.

ii) Gas measurements: Measurements of the CO in NGC 253 were made by Rickard et al. (1977) and Solomon and De Zafra (1975). If we assume a gas temperature of 20°K, the results of Rickard et al. (1977) yield a total CO column density of 1.3×10^{19} cm^{-2}. Using $[CO]/[H_2] = 4 \times 10^{-5}$ we find a value of 3.2×10^{23}/cm^2 or 1.1 g/cm^2 for the nuclear column density of H_2.

Aperture synthesis measurements of NGC 253 in HI have been made by Combes et al. (1977). These measurements were made with a 2' x 3' beam. Their results show a peak HI column density of 1.3×10^{22}/cm^2 in the direction of the nucleus, or roughly 1/30th the amount of H_2 derived above.

As was the case with M 82, there was no sign of a HI hole at the nuclear position.

Combining the H_2 estimates with the HI and 1 mm observations gives a rough gas to dust ratio of 85:1 for NGC 253. A short observing schedule precluded any 1 mm mapping of NGC 253. The mapping done in CO by Rickard et al. (1977) shows a more extended central region than was observed in M 82. An interesting project for the future would be to see if this extension exists at 1 mm as well.

NGC 6946

Although NGC 6946 is almost face on, it was chosen for this study on the basis of the strong central concentration observed at other wavelengths (Morris and Lo, 1978; Rogstad et al., 1973). The galaxy is classified as a Scd (Morris and Lo, 1978). The beam center position for the 1 mm observations was approximately 17" off from the nuclear position listed in Condon and Dressel (1976). This discrepancy is due to an error in the SAO catalogue. The position used in our measurements is accurate.

i) Spectrum: Although the far infrared data on NGC 6946 is scanty, there is enough available to fit the curve shown in Figure 5-1d. Assuming the emissivity varies as $\nu^{1.5}$, this yields a dust color temperature of 43°K.

ii) Gas measurements: NGC 6946 has been observed in CO emission by Morris and Lo (1978). Their observations show a peak total CO column density of $1.4 \times 10^{18}/cm^2$ in the

direction of the nucleus for an assumed gas temperature of 20°K. For the purposes of comparison we have reduced this data using the technique described in Rickard et al. (1977). For $[CO]/[H_2] = 4 \times 10^{-5}$ the column density of H_2 is $3.7 \times 10^{22}/cm^2$ or $0.12\ g/cm^2$.

The HI distribution in NGC 6946 has been studied by Rogstad et al. (1973) with a beam size of 2'. Their work shows a definite HI hole at the position of the visible nucleus. Undoubtedly this is due to most of the hydrogen being in molecular form in the nuclear regions, as implied by the sharp nuclear peak seen in CO. As a result, the HI column density is only $1.4 \times 10^{21}/cm^2$ in the direction of the nucleus.

Combining the hydrogen estimates with our 1 mm data we derive a rough gas to dust ratio of 92:1 for NGC 6946. Since NGC 6946 is almost face on, there is no contribution to the 1 mm flux from the spiral arms. If the spiral arms have a radically different gas:dust ratio than the nucleus, this would show up as a difference in the gas;dust ratio for this galaxy compared to the edge on galaxies. Such a difference is not indicated by our results. It should be noted that the 100:1 gas to dust ratio quoted for our Galaxy is derived from local measurements in the spiral arms.

NGC 4631

NGC 4631 is a nearly edge on Sc spiral galaxy. Of the 14 edge on spiral galaxies studied by Krumm and Salpeter

(1979), NGC 4631 had the greatest column density of HI. The distance to this galaxy runs from 5.2 Mpc to 9.8 Mpc, depending on the distance determination method used (Krumm and Salpeter, 1979). For the analysis of our work we have used the lower figure.

i) Spectrum: The far infrared radiation from NGC 4631 has not been detected as yet. It is therefore impossible to determine the temperature or emissivity index of the dust. We therefore assumed that the dust in NGC 4631 had a temperature of 20°K.

ii) Gas measurements: NGC 4631 was observed in CO by Rickard et al. (1977) but no significant emission was detected. Their RMS noise for this object corresponds to a 3σ upper limit on the total CO column density of $1.6 \times 10^{18}/cm^2$, assuming a gas temperature of 20°K. For $[CO]/[H_2] = 4 \times 10^{-5}$ this means that the 3σ upper limit on the molecular hydrogen column density is $4.0 \times 10^{22}/cm^2$ or $0.13\ g/cm^2$.

The column density of HI has been mapped in NGC 4361 by Krumm and Salpeter (1979) along the plane of the galaxy with a beam size of 3.2'. They find no sign of a hole at the position of the nucleus and derive a HI column density of $3.2 \times 10^{21}/cm^2$ at this position. This gives a lower limit to the total gas mass column density of $5.4 \times 10^{-3}\ g/cm^2$.

The range in the gas to dust ratio, going from the lower gas limit derived from the HI measurements to the 3σ upper limit from the CO results, runs from 3:1 to 31:1. This indicates that NGC 4631 is an extremely dusty galaxy, or is

unusual in some other way that would increase the 1 mm flux to CO flux ratio.

IC 342

IC 342 is an almost face on Scd spiral galaxy. It was chosen to be included in this study due to the data that already exists at other wavelengths; data that indicated it should be bright at 1 mm.

i) Spectrum: Although IC 342 is relatively faint at far infrared wavelengths, some broadband detections were obtained by Becklin et al. (1980). These results, shown in Figure 5-1f, are insufficient to determine both the temperature and emissivity index of the dust. Accordingly, the emissivity was assumed to vary as $\nu^{1.5}$ in a manner similar to the other observed spiral galaxies. Using this assumption the temperature is then calculated to be 32°K for isothermal dust. The 3σ upper limit at 1 mm fits this model.

ii) Gas measurements: IC 342 has been observed in CO by Morris and Lo (1978) with a 65" beam. Their results show a peak total CO column density of $1.1 \times 10^{18}/cm^2$ assuming a gas temperature of 20°K. These workers have also made a scan across the galaxy through the nucleus. As expected, the CO emission is strongly peaked at the position of the nucleus. Assuming $[CO]/[H_2] = 4 \times 10^{-5}$, the column density of H_2 is $2.8 \times 10^{22}/cm^2$ or $0.10\ g/cm^2$.

IC 342 has also been observed in HI by Rogstad et al. (1973) using aperture synthesis techniques. Their beam size

for the observations was 4'. As was the case with NGC 6946, the results show a pronounced HI hole at the location of the nucleus. Again, this is probably due to most of the hydrogen being in molecular form in this region. The HI column density at the nucleus is $7.2 \times 10^{20}/cm^2$, or 1/50th of the amount of H_2. As a result, our 3σ lower limit for the overall gas:dust ratio is 17:1 for the nucleus of IC 342.

NGC 1068

Seyfert galaxies are characterized by extremely bright nuclei. It has already been mentioned that these galaxies have been classified into two classes, with a few galaxies belonging to an intermediate class (Khachikian and Weedman, 1974; Osterbrock and Koski, 1976). Although this classification is made on the basis of observed line widths in the visible, it turns out that there is also a difference in the infrared spectra between the two classes. NGC 1068 is classified as an archetypical Class II Seyfert. Various workers have concluded that the infrared radiation from Class I Seyferts is due to the same non-thermal source that is responsible for the short wavelength radio emission, while the infrared radiation from Class II Seyferts is due to thermal emission from dust (Neugebauer et al., 1976; Stein and Weedman, 1976). Neugebauer et al. (1976) have carried their conclusions further, postulating that there is a non-thermal source in all Seyfert galaxies. In their model the non-thermal source is stronger in the Class I galaxies than it is in the Class II's; strong enough to vaporize dust grains.

Therefore, infrared emission from dust will only be observed in Class II galaxies.

i) Spectrum: The far infrared and submillimeter spectrum of NGC 1068 cannot be fit with the $\varepsilon(\nu)\alpha\nu^{1.5}$, isothermal dust model that fits the other galaxies observed (Figure 5-1b). Telesco and Harper (1980) have found a peculiar double hump in the far infrared spectrum that can be fit by a two temperature dust model. The galaxy has not been detected at wavelengths longer than 380 μm in the submillimeter. Our 1 mm measurement gives a 3σ upper limit of 0.99 Jy, over a factor of two lower than previous 1 mm upper limits (Elias et al., 1978).

If the 1 mm emission is due to the lowest temperature dust reported in Telesco and Harper (1980) (dust temperature = 33°K), and the dust emissivity is described by $\varepsilon(\nu)\alpha\nu^{p}$, then $p \geq 2$. The very low 1 mm flux also means that there can be very little dust in a Region II environment.

ii) Gas measurements: NGC 1068 has been observed in CO by Rickard et al. (1977). Their CO total column density for a 33°K gas temperature is $8.4 \times 10^{18}/cm^2$. Using $[CO]/[H_2] = 4 \times 10^{-5}$ (which may be greatly in error for Seyferts) the column density of H_2 is $2.1 \times 10^{23}/cm^2$ or 0.70 g/cm^2. This column density poses a problem (cf. Rickard et al., 1977) in that it implies too much mass within the beam. The total mass of stars and gas estimated by dynamical means is smaller than the H_2 mass derived above (Walker, 1968). The most probable reason for this discrepancy is that the

value of $[CO]/[H_2]$ is larger in NGC 1068 than it is in spiral galaxies.

HI measurements of NGC 1068 have been made by Rogstad et al. (1967) and Heckman et al. (1978). Since neither of these observations were made using aperture synthesis techniques, fine scale maps are not available. With the 3.3' beam of Heckman et al. (1978) the average HI column density in the direction of the nucleus is only 5×10^{-5} g/cm^2. This value is so low as to be comparable to the mass column density of CO measured by Rickard et al. (1977). Undoubtedly this is due to the different beam sizes used in the two observations, the HI flux being much more diluted. As in the spiral galaxies, we will assume that the HI mass in the nucleus is much smaller than the H_2 mass.

Using the CO measurements only, the 3σ lower limit to the gas:dust ratio is 200:1. This is very high. Changing $[CO]/[H_2]$ to a value such that there is no total mass problem would bring this ratio down closer to the 100:1 ratio estimated for our galaxy.

iii) Models for NGC 1068: Hildebrand et al. (1977) have reviewed the various theories that have been advanced to explain the far infrared emission from NGC 1068 and have concluded that only thermal radiation from dust can explain their observations. Our 1 mm results present a difficulty with this conclusion. Since the 3σ upper limit at 1 mm is so low, the emissivity index of the dust must be greater than or equal to 2. This is significantly higher than the

emissivity index of other normal spiral galaxies. This means that either a) the dust is of a different composition in NGC 1068 than it is in the spiral galaxies, or b) there is a different temperature distribution in the dust emission regions in the galaxies and in NGC 1068.

There is no evidence supporting point a). In fact, there is evidence that the dust is of similar composition in M 82, NGC 253, the Galactic center, and NGC 1068 since there is an observed 10 μm absorption feature in all of these objects (Rieke and Low, 1975; Kleinman, Gillett, and Wright, 1976; Gillett et al., 1975; Aitken and Jones, 1973; Houck et al. 1980).

Point b) is more likely to be correct. It has already been stated that most of the 1 mm emission from normal spiral galaxies originates in hot molecular clouds. In these clouds the energy is supplied by small hot stellar or proto-stellar objects embedded in the dust and gas. These clouds have been treated theoretically by Werner and Salpeter (1969) and Leung (1976), among others. These workers have concluded that there is only a mild variation of temperature throughout the cloud. Nonetheless, the temperature gradient that does exist will have the effect of decreasing the spectral index of the submillimeter emission. This means that the large spectral index for NGC 1068 could be due to dust that is all at the same temperature. This could happen if the dust in NGC 1068 were spread throughout the energy source. If this is the case, it is possible to set a lower limit on

the size of the non-thermal source.

Hildebrand et al. (1977) have used their submillimeter observations and equation (5.15) to derive a lower limit to the diameter of the submillimeter emission region of 5". At a distance of 18 Mpc this corresponds to 440 pc or a volume of 4.4×10^7 pc^3. Since the infrared luminosity of NGC 1068 is 3×10^{11} $L_\odot$ (Telesco and Harper, 1980), the energy generation per unit volume is less than 10^{-18} ergs/cm^3.

If the energy source were non-thermal, it is difficult to understand how dust could survive within the source. In addition, for dust grains with a radius of 1 μm located in a region 440 pc in diameter and with a total dust mass equal to the 3σ upper limit for NGC 1068 given in Table 5-7, the lifetime of a relativistic electron would only be about one year before it struck a dust grain. This makes it unlikely that the dust is mingled in with a non-thermal source.

One further process for creating isothermal dust is given in Harwit and Pacini (1975). They suggest that the flux from active galactic nuclei is due to large numbers of HII regions and supernovae. There are two ways such a region could have isothermal dust. Large numbers of molecular clouds, packed sufficiently close together, would have dust temperatures that are more isothermal than the dust temperatures in an isolated molecular cloud. In other words, the colder dust in the outer regions of a molecular cloud would be heated by the flux originating in a nearby cloud. For a

typical HII region luminosity of 10^6 $L_\odot$ (Wynn-Williams and Becklin, 1974), it would require 3 x 10^5 such regions to account for the infrared luminosity of NGC 1068. An average sized molecular cloud is perhaps 2 parsecs in diameter. If we assume that a packing density of 1 HII region per 10 pc^3 is necessary for isothermal dust; the total volume occupied by the regions will be 3 x 10^6 pc^3. This volume is a factor of 10 less than the minimum volume derived by Hildebrand et al. (1977). This objection could be overcome if the packing density needed for isothermal dust were less than the 1 cloud per 10 pc^3 estimated above.

There is a second way that the active region proposed by Harwit and Pacini (1975) could have isothermal dust. It has been suggested by Harwit et al. (1972) that the dust inside of the Stromgren sphere around an ionising source would be illuminated by an essentially constant flux of Lyman photons, irrespective of its location. If there were enough ionizing sources, the nucleus of NGC 1068 could be one large Stromgren sphere with isothermal dust. Following the arguments outlined in Harwit et al. (1972) and using the lower limit to the volume set by Hildebrand et al. (1977), we find that this scenario requires that $n_e \leq 350/cm^3$ within the active region. This value is within the electron density upper limits set by Neugebauer et al. (1976) on the basis of the observed emission lines. Therefore, this could be what is happening in the nucleus of NGC 1068.

The Harwit-Pacini scenario does have one serious complication. As their model requires large amounts of molecular clouds and star formation, it will also mean that there are frequent supernovae in the nucleus of NGC 1068. A typical supernova remnant can sputter away the silicate grains in 300 $M_\odot$ of gas before it slows and cools sufficiently to be harmless (Draine and Salpeter, 1979). With grains that are more fragile than silicates, having icy mantles for example, even more dust can be sputtered. If the supernovae occur frequently enough, their blast waves will destroy grains faster than they can be created in molecular clouds.

If we let t_c be the time it takes a cloud to turn inside out, releasing its grains to the interstellar medium, then there must be less than

$$R_{SN} = \frac{M_D}{3\ M_\odot} \times \frac{1}{t_c} \qquad (5.23)$$

supernovae/year for the grains to exist. In this equation M_D is the total mass of dust in the nucleus of NGC 1068 and we are assuming a gas to dust ratio of 100:1. We can estimate R_{SN} in the following way. Let us assume that 10% of the total luminosity from NGC 1068 comes from stars that will eventually become supernovae. Now in one cloud turnover lifetime $L_T t_c$ energy will be generated in the nucleus of NGC 1068, where L_T is the total observed luminosity (3×10^{11} $L_\odot$, Telesco and Harper, 1980). A 10 $M_\odot$ star, burning 10% of its hydrogen to helium, will generate 10^{52} ergs of energy in its lifetime. Thus the number of such stars that are

needed to account for the energy released from the nucleus of NGC 1068 in time t_c is given by:

$$\frac{L_T t_c}{10^{52} \text{ ergs}} \tag{5.24}$$

If 10% of these stars become supernovae, this gives a supernova rate of

$$\frac{L_T}{10^{53} \text{ ergs}} \tag{5.25}$$

or approximately 3/year. If $M_D = 2 \times 10^7 M_\odot$ (Telesco and Harper, 1980) then

$$t_c < 2 \times 10^6 \text{ years} \tag{5.26}$$

if the dust creation rate is to exceed the destruction rate. Now in our Galactic disk the estimates of t_c range from 10^6 to 10^8 years (Salpeter, 1977; Scoville et al., 1979). It might be expected that the cloud turnover rate in the nucleus of NGC 1068 would be on the low side of this range, since the Harwit-Pacini model requires a much more compact distribution of gas and dust than exists in the disk of our Galaxy. Therefore, although supernovae sputtering does not totally rule out the Harwit-Pacini scenario, it certainly must be taken into account in any detailed model. Since icy mantles sputter away much more easily than do the silicate cores, the above analysis shows that such core-mantle grains cannct exist in a Harwit-Pacini model for NGC 1068.

Finally, there is one other way that has been suggested to create isothermal dust. It has been shown (Ferch, 1977) that the stellar flux in a planetary nebula will create

enough radiation pressure to drive the dust grains away from the central star. As the dust moves away from the star it drags the gas along with it. Eventually, a hollow shell of nearly isothermal gas and dust forms around the star. Possibly a similar shell exists in NGC 1068, although on a much larger scale.

One difficulty with any sort of isothermal model is caused by the CO measurements. The CO flux level from NGC 1068 is very high. This implies a great deal of molecular hydrogen. Since so little dust is seen, the gas:dust ratio for NGC 1068 is much higher than in our galaxy. The only way to bring this ratio down is to have large amounts of very cold unobservable dust.

Upper Limits

The spiral galaxies NGC 891, NGC 925, NGC 4244, and NGC 5907 were not detected at 1 mm. The various parameters of these galaxies, and the results of observations at other wavelengths are listed in Table 5-9. The 1 mm derived dust mass upper limits assume a dust temperature of 20°K.

None of these galaxies have been reported to have been observed in CO emission so that estimates of H_2 masses are difficult to make. Both NGC 891 and NGC 925 have been observed in HI with sufficiently small beam sizes to be useful. NGC 891 is an almost edge on Sb spiral galaxy. Sancisi and Allen (1979) have observed this galaxy using aperture synthesis techniques that realise a beam size of 25" x 37". A scan along the plane of the galaxy shows a

pronounced hole, roughly 1' in size, in the column density at the location of the nucleus. A similar hole was observed in NGC 925 by Krumm and Salpeter. Their beam size in this observation was 3.2'. Comparing these galaxies to IC 342 and NGC 6946, these results would imply that there is a great deal of molecular hydrogen in the nuclei of these galaxies. The HI nuclear column densities for both of these galaxies are shown in Table 5-9. Since the information about the gas is so scanty, no attempt was made to compute the gas:dust ratio lower limits for these galaxies.

Table 5-9

Upper Limits

Galaxy	Type	Distance (Mpc)	3σ Upper Limit for D (g/cm^2) x 10^{-3}	HI ($atoms/cm^2$) x 10^{21}
NGC 891	Sb	10.0	4.4	7.9
NGC 925	Sc/SBc	14.8	4.6	1.6
NGC 4244	Scd	3.8	5.8	–
NGC 4907	Sc	4.6	7.4	–

HI column densities are from Krumm and Salpeter (1979) and Sancisi and Allen (1979).

Upper limits on the dust mass column density assume a dust temperature of 20°K.

The Milky Way Galaxy

It is interesting to consider how our galaxy would appear if placed at a distance of 4 Mpc. In some ways it is

more difficult to observe our galaxy, since we are located in the dusty spiral arms. For example, even the Hubble type of our galaxy is not known with any degree of confidence, although it is thought to be either Sb or Sc (de Vancouleurs and Pence, 1978).

At a distance of 4 Mpc a 66" effective beam size would correspond to 1.3 kpc. Thus, we should consider only the observations of the central 1.3 kpc of the Galaxy. At a distance of 10 kpc, this corresponds to maps of 7 1/2° in extent. This is a problem, since most studies, in the far infrared and submillimeter in particular, do not extend over such a large area of sky. There is also the problem of including the contributions from the spiral arms; this contribution would vary as we change our imagined position outside of the Galaxy.

The largest extent far infrared map of the Galaxy was obtained by Hoffman et al. (1971) at 100 μm. Their mapped area, 2° x 3.6°, had a 100 μm integrated flux density of 7.6×10^6 Jy. If we assumed that:

1) all the 1 mm radiation would come from this region,
2) the dust emissivity would vary as $\nu^{1.5}$, and
3) the dust temperature is 40°K,

then the 1 mm flux would be 1.5×10^4 Jy at 10 kpc. At a distance of 4 Mpc this would be reduced to 0.1 Jy, or lower than the flux from any of the detected galaxies. It might be expected that the measured flux at our imaginary position would be somewhat higher, since our beam would take

in more of the galaxy than appears in the map of Hoffman et al. (1971). Our galaxy could therefore be similar in brightness to NGC 6946, which had a 1 mm flux of 0.2 Jy at a distance of 4.2 Mpc.

Summary and Conclusions

To summarize our results we find:

1) The 1 mm flux observed from spiral galaxies is due to thermal emission from dust.

2) The far infrared, submillimeter, and millimeter measurements of M 82 and the spiral galaxies give spectra that are similar in shape to those from molecular clouds with embedded hot sources that have been observed in our Galaxy. The galactic spectra can be fit to an isothermal dust model with dust temperatures around 40°K and emissivity indices of 1.5, or to a two temperature model with a dust emissivity index of 2.5.

3) There is little dust at temperatures $30°K > T_d > 10°K$ outside of hot molecular clouds in any of the detected galaxies.

4) There seems to be no correlation between the total HI mass in a galaxy and the 1 mm flux from that galaxy's nucleus. There may be a correlation between the 1 mm flux and the synchrotron radiation from spiral galaxies.

5) In M 82 the 1 mm emission shows a strong peak at the nuclear position, similar to the peak observed in CO.

6) NGC 4631 seems to be an unusually dusty galaxy.

7) The submillimeter spectral shape of NGC 1068 is different than the spectral shape of the other galaxies observed. This difference could be caused by differences in either the composition of the dust or in the temperature structure of the submillimeter emission region. The gas to dust ratio is also very high in this galaxy.

8) The average gas:dust ratio for the galaxies was roughly the same as the 100:1 ratio estimated for our Galaxy. There are, however, three major sources for uncertainty in these measurements. First of all, the estimates of $Q/a\rho$ were admittedly rather arbitrary. Using a lower value for this quantity would bring the gas:dust ratio down. In addition, the presence of cold dust ($T_d < 10°K$) would not be detected in this study. Finally, there is some dispute about the correct value of $[CO]/[H_2]$. If we use the value suggested in Blitz and Shu (1980), the gas:dust ratio would be a factor of 5 lower than is reported above.

Appendix A

The Bolometer

Theory

A bolometer is a radiation detector that works by absorbing incident radiation and then measuring the temperature rise in the device due to the power absorbed. The ideal bolometer will absorb radiation of all wavelengths, giving it an infinite bandwidth. Although this ideal is not realizable, bolometers still offer the largest bandwidths of any radiation detectors.

We can represent a bolometer schematically as shown in Figure A-1. Bolometers are composed of three main elements. One element absorbs the radiation, one element measures the temperature change, and one element thermally connects the bolometer with a cold sink. This last element is needed to reset the bolometer after it has absorbed radiation so that it can be used to make another measurement. These three elements are called the absorber, thermistor, and thermal link, respectively. In some bolometers some of these elements do double duty. For example, in some short wavelength bolometers the thermistor also acts as the absorber.

As will be seen later, making many short measurements leads to lower noise than making one long measurement does. Therefore, bolometers are traditionally run in an AC mode. This means that the incident radiation varies periodically, with the bolometer measuring the magnitude of the variations.

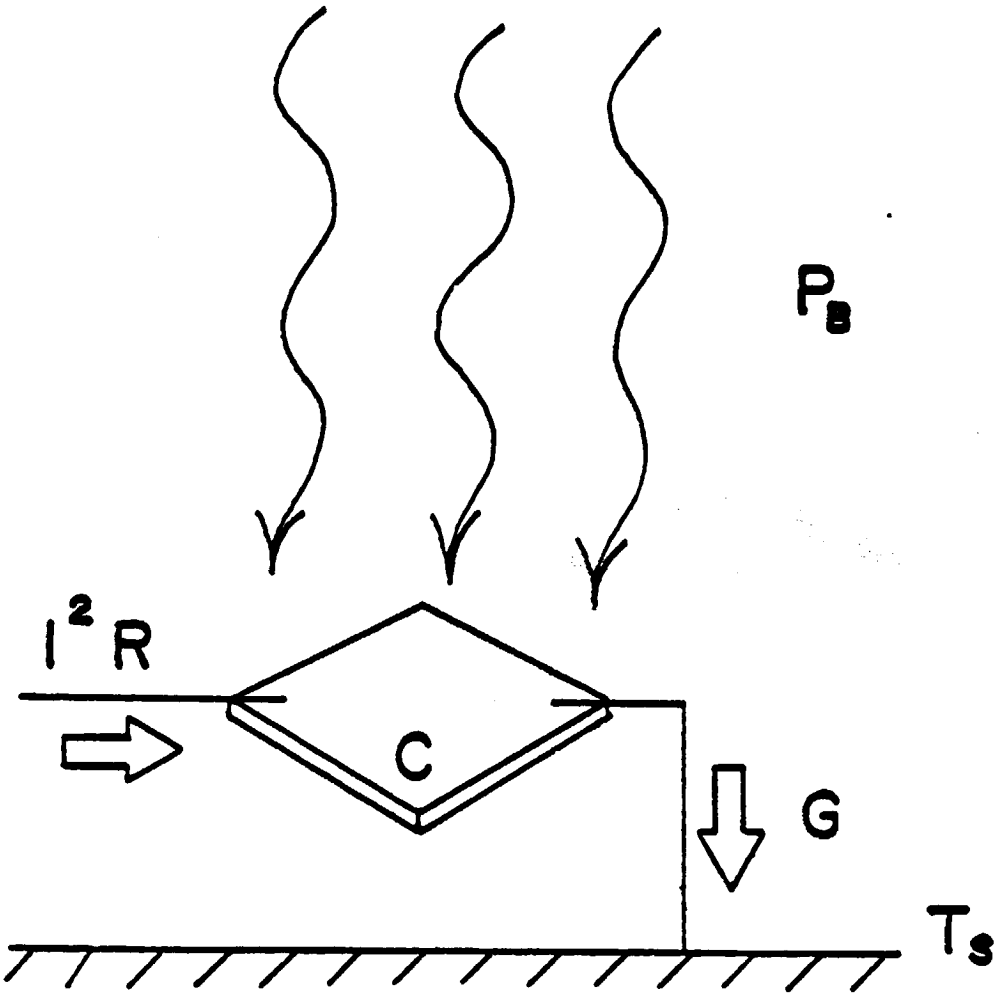

Figure A-1: Schematic diagram of a bolometer. The symbols are defined in Table A-1.

Optimisation of bolometers is a complicated problem. Following the treatment of Nishioka et al. (1978) we define the symbols listed in Table A-1. The DC temperature balance of the bolometer is given by:

$$T_b = \frac{P}{G} + T_s . \qquad (A.1)$$

It can be shown from statistical mechanics that the thermal fluctuations in an object vary as the square root of the absolute temperature. Therefore, bolometers become less noisy and more sensitive as they are cooled down. The additional temperature variations caused by the periodic variability in the radiation absorbed by the bolometer are given by:

$$\Delta T = \frac{\Delta P}{G} \left(1 + w^2 c^2 / G^2\right)^{-1/2} \qquad (A.2)$$

Two different types of thermistor elements are now commonly used to measure the ΔTrms of the bolometer. The resistance of superconducting metals, carefully maintained on the transition edge temperature, is very sensitive to small changes in temperature. Thus superconducting transition edge thermistors can be very sensitive. However, bolometers using this type of thermistor are more complex and less reliable than bolometers using semiconducting thermistors (Clarke et al., 1977).

Semiconductors with appropriate doping levels can also be very sensitive temperature measuring devices. The resistance of these semiconductors can be described by an energy

Table A-1

Symbol Definitions

T_s: Temperature of cold surface (thermal sink)

T_b: Temperature of bolometer

G : Thermal conductivity between cold surface and bolometer

c : Heat capacity of bolometer

P : Total power into bolometer from absorbed radiation and resistive heating

w : $2\pi X$ chopping frequency

ΔT: RMS temperature change of bolometer

ΔP: RMS change in radiative power absorbed in bolometer

I : Current through bolometer

R_b: Resistance of bolometer

A : Energy gap of thermistor crystal in °K

P_b: Radiation absorbed by bolometer

K : Boltzman's constant

h : Planck's constant

R_L: Resistance of load resistor

T_L: Temperature of load resistor

N : Excess current noise constant

i_n: Preamp current noise

e_n: Preamp voltage noise

ϵ : Bolometer absorption efficiency

δ : $\equiv \dfrac{R_b}{R_L + R_B}$

gap relation

$$R = R_o e^{A/T} \tag{A.3}$$

where A depends on the doping level. The bolometer used in the Cornell ^{3}He system used a Germanium crystal doped with indium and antimony as the thermistor element. The resistance of the thermistor element was measured by connecting it to a current source and then measuring the voltage drop across the element. The simplest current source is a voltage source and a large load resistor connected in parallel. With this current source the voltage response of the bolometer becomes:

$$S(\text{volts/watt}) = \frac{I\, dR_b/dT_b\, (1-\delta)}{G_e (1 + w^2 c^2 / G_e^{\,2})^{1/2}} \tag{A.4}$$

In this equation

$$G_e = G - I^2 \frac{dR_b}{dT_b} (1 - 2\delta) \tag{A.5}$$

This effective thermal conductivity reflects the extra heating by the bias current as the resistance changes. Again, following the treatment of Nishioka et al. (1978) we can write the voltage noise in the output of the bolometer as the combination of the various noise sources added in quadrature.

$$V_{tot}^2 = S^2 N_{BP}^2 + S^2 N_{TF}^2 + N_{JL}^2 + N_{JB}^2 + N_{EB}^2 + N_{CP}^2 + N_{VP}^2 \tag{A.6}$$

In this equation, N_{BP} is the noise to statistical fluctuations in the background power and

$$= \sqrt{\frac{2P_b h\nu}{1-e^{h\nu/kT}}} \approx \sqrt{2P_b kT} \quad \text{for } h\nu << kT \tag{A.7}$$

(In this equation T is the temperature of the background.)
N_{TF} is the noise due to statistical thermal fluctuations in the bolometer and

$$= \sqrt{4kT_b^2 G} \tag{A.8}$$

N_{JL} is the Johnson noise in the load resistor and

$$= \delta \sqrt{4kT_L R_L} \tag{A.9}$$

N_{JB} is the Johnson noise in the bolometer and

$$= \sqrt{4kT_b R_b} \tag{A.10}$$

N_{EB} is the excess current noise in the bolometer and

$$= N \frac{IR_b}{\sqrt{W}} \tag{A.11}$$

This noise is also called contact noise and arises from poor electrical contacts. It is impossible to eliminate, but with proper construction techniques the constant N can become very small.
N_{CP} is the excess current noise of the preamp and

$$= i_n R_b \tag{A.12}$$

and N_{VP} is the voltage noise of the preamp and

$$= e_n/\sqrt{w} \qquad \text{(A.13)}$$

The total power, P, into the bolometer that must be carried away by the thermal link is given by

$$P = P_b + I^2R_b \qquad \text{(A.14)}$$

Looking at these equations a number of general points can be made about bolometer optimisation.

1) It is desirable to have as small a heat capacity as possible. In practice this means going to low temperatures, since the heat capacity varies as T^3 for insulators and superconductors and as T for conductors.

2) Even assuming the heat capacity can be made very small, the total power, P, into the bolometer determines the minimum value of G that can be used. From equation A.1 we see that too small a value of G means that the bolometer temperature will rise to unacceptable values. Therefore, it is important that the background radiation falling on the bolometer be filtered so that the bolometer is heated only by radiation wavelengths of astronomical interest. Furthermore, it is also important to keep the electrical I^2R heating of the bolometer at a minimum.

3) The maximum value of R_b is limited by the properties of the JFETs used in the preamps. For most transistors of this design the current noise and voltage noise will be equal with an input impedance of approximately 1 MΩ.

4) Using the energy gap relation of equation A.3 for the bolometer we find

$$\frac{dR_b}{dT_b} = -\frac{AR_b}{T_b^2} \qquad (A.15)$$

Therefore, keeping the bolometer at as low a temperature as possible is important for high sensitivity.

5) The load resistor should be as large as is physically convenient.

It can be seen that bolometer optimisation is a complicated problem, with peak results obtained only for a given bolometer environment. The bolometer used in the Cornell ^{3}He system was carefully optimised for the background power load, preamp properties, and cold surface temperature of the dewar being used. The electrical performance of the bolometer is given in Table A-3. The optical performance of the bolometer will be covered in Appendix B.

Total System Noise

Some of the various sources of bolometer noise have been discussed above. To get a complete picture of the system performance it is useful to consider all of the noise sources. The noise sources can be divided into four main categories.

1) Dewar noise. Dewar noise incorporates all of the terms in equation A.6 as well as additional noise caused by microphonics and changing sensitivity. The measured magnitude of the various terms of equation A.6 is given in Table

A-2. In addition, the dewar optical responsivity and noise are plotted in Figure A-2 as a function of bolometer bias current.

Microphonics is always a problem with high impedance detector systems such as bolometers. In order to minimise this problem, every wire was securely glued down inside the dewar while the dewar was constructed to be as rigid as possible. These procedures caused the residual microphonics to be of a high resonant frequency ($\nu >> 10$ Hz) and to be quickly damped. A Fourier analysis was made of the total dewar noise and the results are shown in Figure A-3. It can be seen that there is some 1/f noise, but at the 11 Hz chopping frequency its magnitude is small.

In order to estimate the degree the sensitivity of the dewar changed during an observing run, careful measurements were made of the system response in the laboratory as a function of time and tilt angle of the dewar. It was found that the dewar sensitivity remained constant to within a few percent as long as the dewar was not tipped more than 70° from the vertical and as long as sufficient time was allowed for the dewar to reach operating temperature after the heat switch was closed. In practice, this thermalisation time was only about 20 minutes.

2) Photometer noise. Photometer noise arises from two different sources. If the chopper throw is set longer than about 4 1/2', the wobbling tertiary mirror will begin to strike the counterbalanced magnets. This causes a serious

Table A-2

Dewar Noise at 10 Hz, Measured at the Bolometer

Background power noise	5.2 nV/$\sqrt{Hz}$
Thermal fluctuation noise	5.0 nV/$\sqrt{Hz}$
Bolometer Johnson noise	5.6 nV/$\sqrt{Hz}$
Load resistor Johnson noise	3.2 nV/$\sqrt{Hz}$
Excess current noise	4.9 nV/$\sqrt{Hz}$
Preamp voltage noise	4.1 nV/$\sqrt{Hz}$
Preamp current noise	5.4 nV/$\sqrt{Hz}$

Table A-3

Measured Bolometer Electrical Performance

Time constant C/G_e = 13.9 msec

Heat capacity $C = 1.50 \times 10^{-9}$ J/°K

Effective thermal conductivity $G_e = 1.08 \times 10^{-7}$ W/°K

Thermal conductivity $G = 0.91 \times 10^{-7}$ W/°K

Operating temperature T_b = 0.43°K

Load resistor R_L = 36.5 MΩ

Figure A-2: Bolometer optical signal and noise as a function of bolometer bias current. The optical signal was measured using a 10 Hz chopped liquid nitrogen source with an f/35 beam.

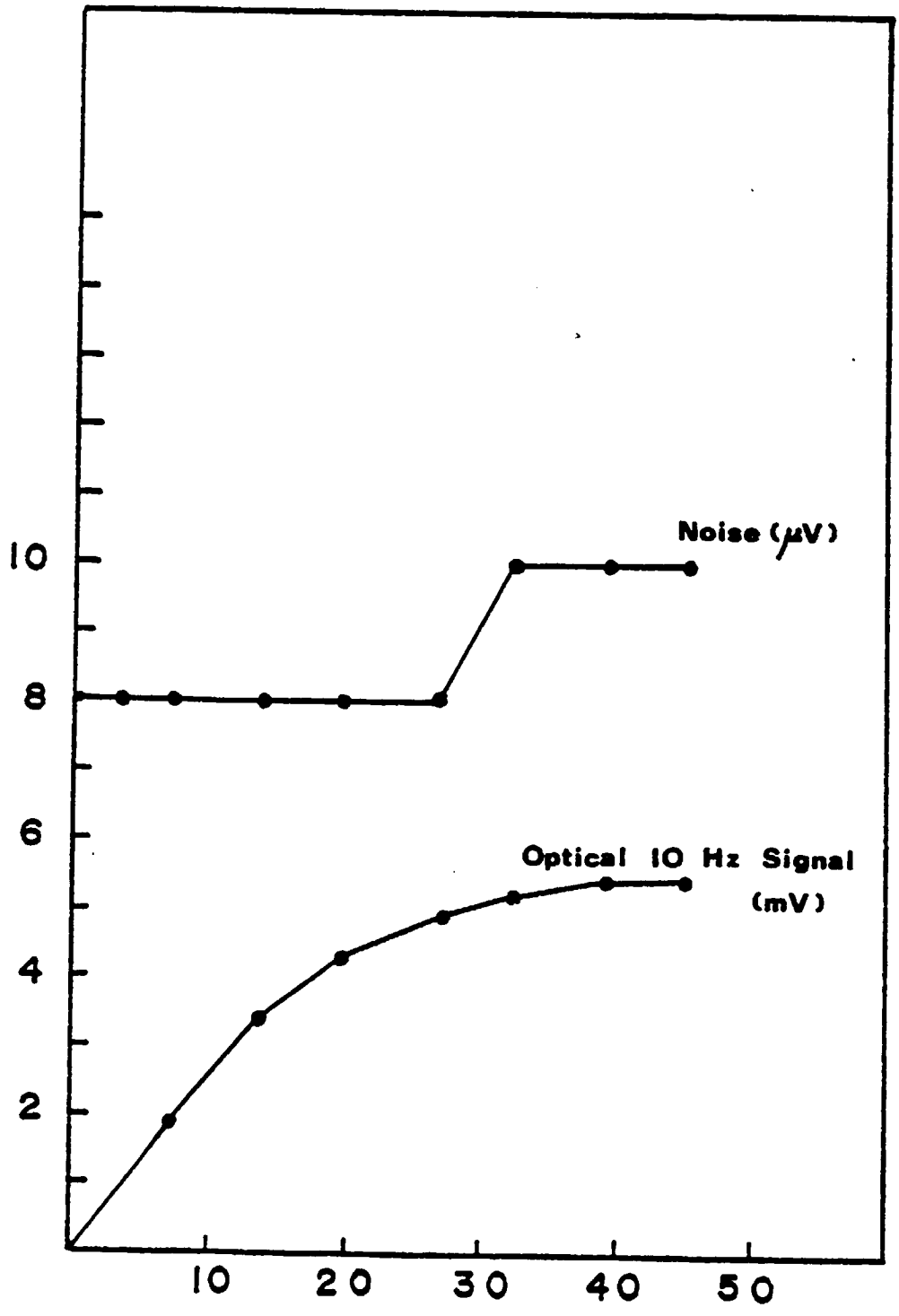
Noise (μV)
Optical 10 Hz Signal
(mV)
10
8
6
4
2
10
20
30
40
50

Figure A-3: Fourier transform spectrum of noise from bolometer and preamp. The high frequency components have been filtered so that there was no aliasing problem.

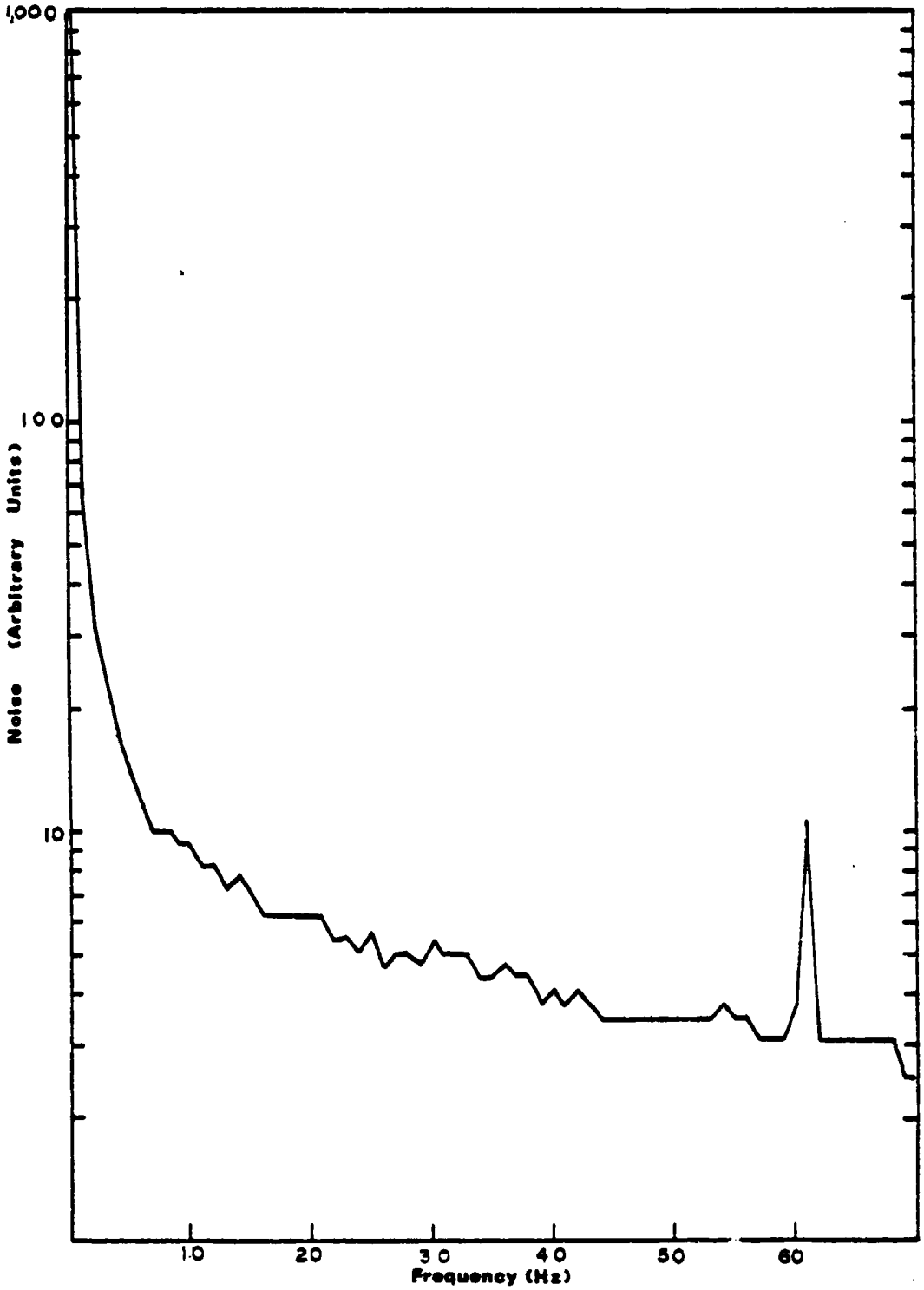
1,000
100
10
Noise (Arbitrary Units)
10
20
30
40
50
60
Frequency (Hz)

distortion of the mirror position waveform and introduces large amounts of microphonic noise in the dewar. This noise source can be eliminated by setting the chopper throw at 4' or less. Another possible source of noise from the photometer is important only during observations of bright sources. If the wobbling mirror is not perfectly periodic in time, the beam position on the sky will change. Since the beam is so large, this effect is very small, but could contribute to the noise from a bright source. For fainter objects the other sources of noise are more important.

3) Atmospheric noise. Due to atmospheric opacity at submillimeter and millimeter wavelengths, atmospheric noise is significant in all but the very best weather. Sky noise is very poorly understood, but is thought to have roughly a 1/f frequency dependence. During our 1 mm observations the sky noise is due to inhomogeneities in the atmospheric water vapor. As these inhomogeneities drift through the telescope beam they will cause variations in the optical depth of the atmosphere at 1 mm. The variability will cause noise from both the atmospheric emission and transmission. The noise caused by the variability in the atmospheric transmission is only important for the brighter sources, while the variability in the emissivity is more important when observing faint sources.

Sky noise is difficult to parameterise, since its effects vary with the observing site, telescope, and weather conditions. In general, the lowest sky noise occurs on

days with very little water vapor. The worst sky noise in a visibly blue sky occurs before a frontal system moves in. Any type of water droplet clouds such as cumulus or stratus clouds render observations useless. Cirrus clouds, being composed of ice crystals, are a problem only in that they can obscure the bright stars needed for the offset pointing technique used during the observations. In fact, cirrus clouds have been present during some of the driest days at Mount Palomar. With a blue sky, the precipitable water vapor levels must be lower than 6 mm for photometric results.

4) External man-made noise. The other noise that has been noted during some observations has been caused by RF interference. At Mount Palomar a nearby radar station can cause RF pickup when the dome slit is aimed due east. At the Anglo-Australian telescope a television broadcast repeater located on an adjacent peak gave some excess noise. By carefully shielding the system electronics these problems were minimised, but were always present in some degree when the respective transmitters were on the air. Luckily, neither of these transmitters ran continuously, so that low noise observations were possible when they shut off.

Bolometer Construction

It has been shown that it is desirable for bolometers to have the lowest heat capacity possible. The easiest way to reduce the heat capacity of the bolometer is to make it smaller. However, beyond a certain point further reductions

in size are no longer possible, since the bolometer will become less efficient in absorption when its size approaches the wavelength of the radiation.

Traditionally, bolometers for the detection of wavelengths of up to 100 μm have been constructed of semiconducting single crystals with two soldered leads providing support, a thermal connection with the cold surface, and electrical connections to the semiconductor. The incident radiation is absorbed either in the bulk crystal itself or in a thin layer of absorbant material painted on the crystal surface.

For longer wavelengths this type of bolometer is no longer suitable for three reasons. 1) The heat capacity of semiconductors is fairly high for bolometers large enough to absorb efficiently. 2) The bulk crystal becomes transparent at these longer wavelengths. 3) Any absorbant material painted on the bolometer would require a thickness that would increase the heat capacity dramatically. Therefore, for wavelengths longer than 100 μm composite bolometers are more sensitive than bulk semiconductors with soldered leads.

In a composite bolometer different specialised parts are assembled together so that the heat capacity is at a minimum while the physical dimensions are large enough for efficient absorption. The composite bolometer constructed for 1 mm astronomy at Cornell is shown in Figure A-4, while Table A-4 lists the sizes and heat capacities of the various elements.

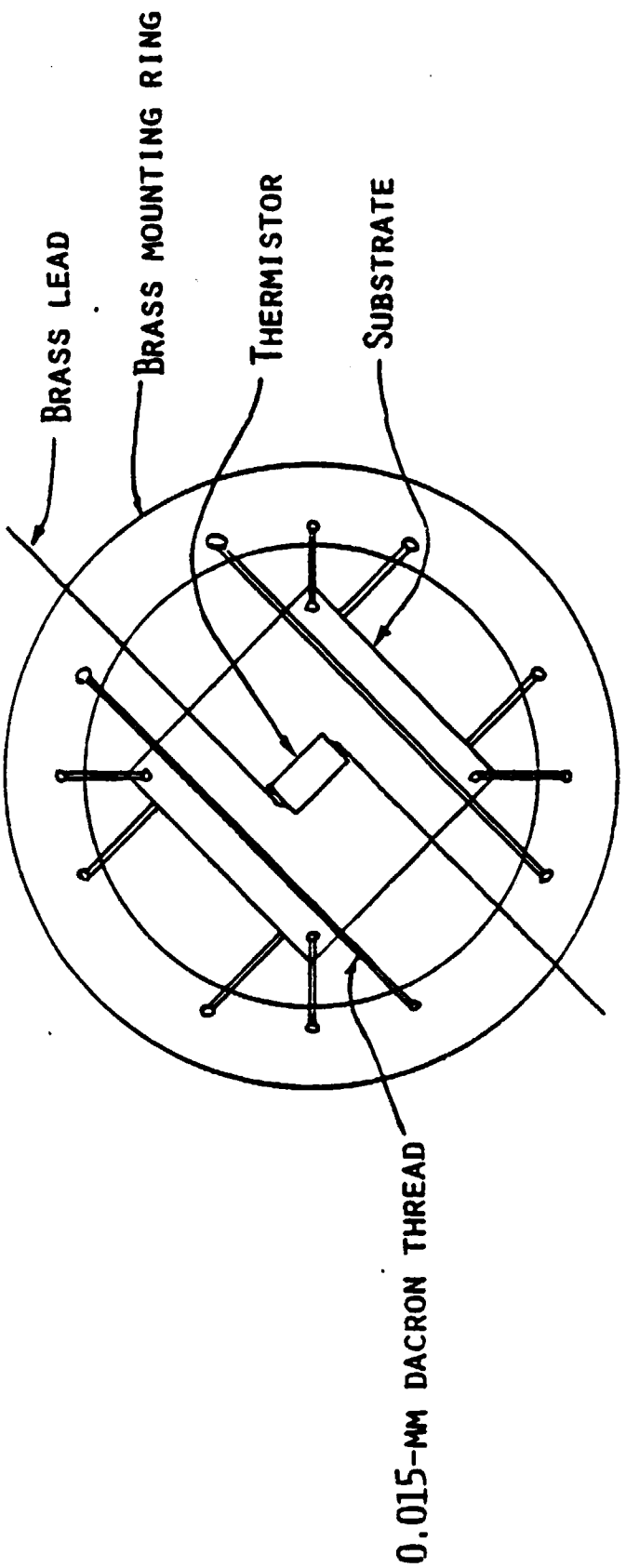

Figure A-4: Composite bolometer used in the ^{3}He dewar.

Table A-4

Heat Capacity of Bolometer Elements

Element	Volume	Heat Capacity	0.43°K Heat Capacity
Sapphire chip	$0.476 \times 0.476 \times 0.127$ cm^3	3.80×10^{-7} T^3 J/°K	8.39×10^{-11} J/°K
Ge thermistor	$0.40 \times 0.30 \times 0.10$ cm^3	3.5×10^{-6} T^3 J/°K	3.22×10^{-11} J/°K
Epoxy	1.6×10^{-5} cm^3	7.00×10^{-4} T^3 J/°K	8.60×10^{-10} J/°K
Indium solder	1.6×10^{-5} cm^3	1.47×10^{-4} T^3 J/°K	1.81×10^{-10} J/°K
Brass wires	3.24×10^{-6} cm^3	1.36×10^{-4} T J/°K	2.02×10^{-10} J/°K
NiCr film	1.7×10^{-7} cm^3	1.50×10^{-3} T J/°K	1.10×10^{-10} J/°K

The basic structural element of the bolomter is a sapphire crystal chip 4.8 mm x 4.8 mm x 0.13 mm in size. Sapphire was chosen because its high Debye theta will cause it to have an extremely small heat capacity at the dewar operating temperature. Diamond has an even smaller heat capacity, but is much more expensive. In any case, even with sapphire the other elements in the bolometer provide the dominant heat capacity. The 23 mm^2 area of the sapphire is large enough to provide efficient absorption of 1 mm wavelength radiation.

A layer of Nichrome has been evaporated on one side of the sapphire chip. Nichrome was chosen because its resistivity is high enough that continuous films of relatively high impedance are easily obtainable, because the resistivity changes very little with temperature, and because the alloy does not become a superconductor at pumped ^3He temperatures. The film thickness was chosen so that the surface resistance of the metal film matched the impedance of free space inside the sapphire. With this criterion there will be no multiple internal reflections when the radiation is incident on the sapphire surface, travels through the sapphire, and is absorbed in the metal film. The absence of these internal reflections also means that the adsorption will be independent of frequency. With frequency independent absorption, 50% of the radiation is absorbed, 25% is reflected, and 25% is transmitted on a single pass through the bolometer (Clarke et al., 1977).

The impedance of free space inside the sapphire is given by

$$Z = \frac{Z_0}{n-1} \qquad \text{(A.16)}$$

where Z_0 is the impedance of free space in a vacuum and has a value of 377 Ω/□ (Clarke et al., 1977). For sapphire at mm wave frequencies n = 3 so that a surface resistance of 189 Ω/□ was required for the Nichrome film. With the resistivity of Nichrome of 1.08×10^{-4} Ω-cm we find a film thickness of 571 nm is needed for the proper impedance. In practice, the thickness of the Nichrome film was monitored during the evaporation process by measuring the visible light transmission through the film. In the dewar the bolometer is mounted in an integrating cavity so that almost all the radiation is eventually absorbed in the bolometer.

In order to measure the temperature change of the sapphire-Nichrome combination a small crystal of germanium doped with indium and antimony was epoxied onto the sapphire surface. This crystal was supplied by A. Sievers and its properties are described in Drew and Sievers (1969).

The crystal was prepared in the following way. First, it was cut to approximate size using a wire saw. The rough crystal was then lapped on glass plate using a slurry of water, glycerine, and #600 grit Unasil abrasive. After being washed in acetone and distilled water, the crystal was etched in a solution of CP-4 until it was shiny and smooth. (CP-4 is composed of a 5:5:3 ratio of 70% nitric acid, 48%

hydrofluoric acid, and glacial acetic acid, respectively. A few drops of 48% hydrobromic acid were added to each 100 ml of mixture in order to speed the etching process.) When the etching was completed, the crystal was immediately quenched in anhydrous methyl alcohol.

The first step in the soldering procedure was to wet the ends of the germanium crystal with pure (99.99%) indium. A soldering iron was plugged into a Variac so that its temperature could be maintained at just above the melting point of indium. The germanium was held with tweezers with a very small droplet of Special-X soldering flux on the bottom-most end. Touching the germanium briefly to the indium-tinned and fluxed soldering iron tip caused the end of the crystal to wet with indium. The procedure was repeated with the other end of the crystal. At this time the fine wire brass leads were also tinned at their very ends with indium.

The crystal was then placed on a resistance strip heater and the fine wires mounted as shown in Figure A-5. Small droplets of Special-X flux were also placed in the positions indicated. While the process was monitored under a microscope, the resistance strip heater was turned on just long enough to cause the fine wires to be soldered to the ends of the crystal. The vapors from the boiling droplets of flux provided the necessary fluxing action.

The completed crystal with leads attached was washed thoroughly in anhydrous methyl alcohol to remove all traces of the remaining flux. The germanium crystal was then tested

Figure A-5: Overhead view of Ge thermistor on resistance heating strip just prior to soldering.

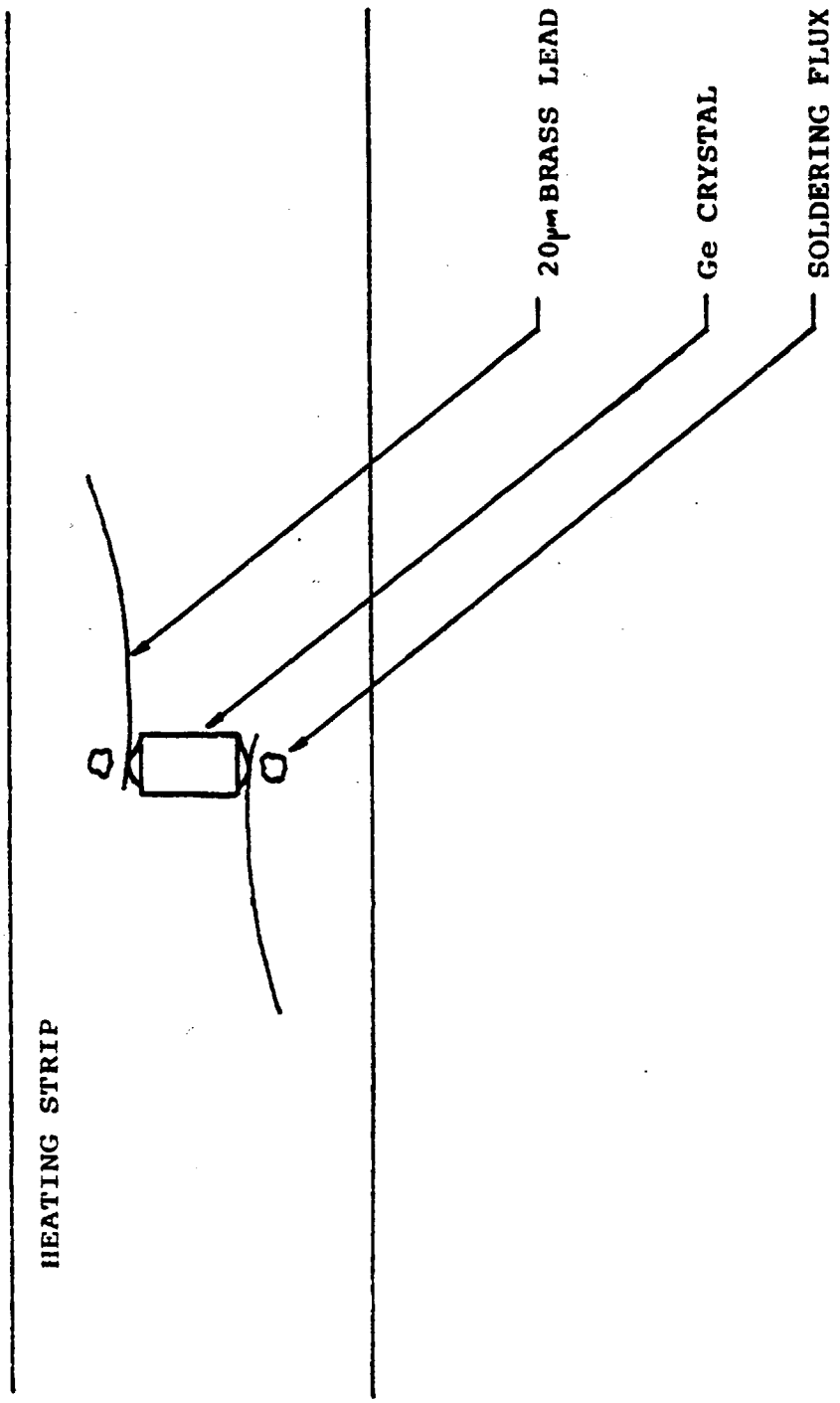
20μm BRASS LEAD
Ge CRYSTAL
SOLDERING FLUX
HEATING STRIP

at ^{3}He temperatures to make sure there was very little excess current noise. This noise, which is 1/f in character, arises predominantly from poor electrical contacts. After passing this test the crystal of germanium was glued into place on the sapphire crystal chip using Emmerson and Cumming Stycast 2850-FT epoxy resin mixed with catalyst #9.

The fine brass wires, being only 0.0008" in diameter, were much too fragile to support the weight of the bolometer. Therefore, strands of Dacron 15 μm in diameter (individual strands of unwaxed dental floss) were epoxied to the four corners of the sapphire chip. The other ends of these strands were epoxied to the bolometer mounting ring. Further rigidity was provided by additional Pyrex fibers laced around the bolometer and attached to the mounting ring. One of the brass bolometer leads was soldered to the mounting ring using Wood's metal to form the ground point for the bolometer. The other lead was epoxied to the ring with Teflon sheets insulating the wire from the ring. Using this mounting system for the bolometer gave enough rigidity to reduce the microphonic noise to a tolerable level. The mounting ring was fashioned from brass and was cemented to the OFHC copper liquid ^{3}He chamber.

Appendix B

Filters and Field Optics

As was noted in Appendix A, it is most important that the incoming radiation entering the dewar be filtered so that only the wavelengths of astronomical interest are absorbed by the bolometer. As is seen in Figure 2-1, submillimeter wavelengths shortward of approximately 750 μm are almost totally absorbed by the atmosphere at ground based observing sites. As a result, the filter stack shown in Figure B-1 was used to form a low pass filter with a half power point of approximately 750 μm. Taking the various elements separately:

1) The Teflon window. The primary purpose of the Teflon window is to provide a vacuum tight window that is transparent to 1 mm radiation. The transmission of Teflon in the submillimeter is given in Hadni (1967) and Muehlner and Weiss (1973). Using these results we find that the transmission of the Teflon window is approximately 90% from 750 μm to 1500 μm.

2) Black polyethylene. The purpose of the 77°K black poly filter is to eliminate the visible and near infrared radiation. Hadni (1967) gives the transmission of black poly as 80% in the 750 μm to 1500 μm range. It is opaque in the visible and near infrared out to 16 μm.

3) Fluorogold. The 4.2°K fluorogold filter provides additional far infrared filtering. The transmission curve

Figure B-1: Diagram of the filters and optics used in the dewar.

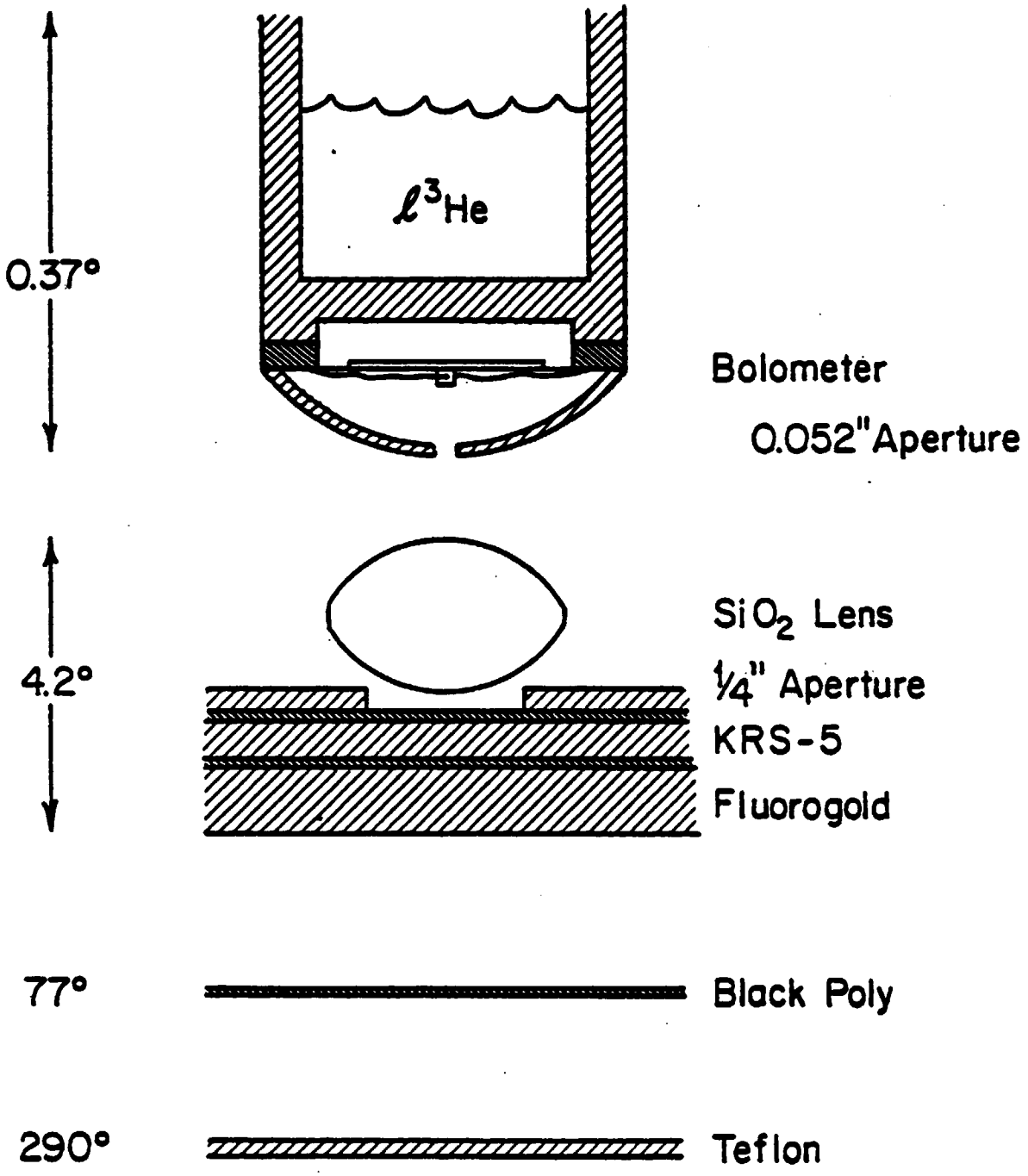
0.37°
ℓ^3He
Bolometer
0.052" Aperture
4.2°
SiO_2 Lens
1/4" Aperture
KRS-5
Fluorogold
77°
Black Poly
290°
Teflon

for 3/32" thick fluorogold rises rather gradually longward of 280 μm with a half power point of 400 μm (Muehlner and Weiss, 1973). Although this material is opaque from 1 μm to 40 μm, it is barely translucent in the visible, hence the need for the black poly. In the 750 μm to 1500 μm range the transmission of the fluorogold filter is 90%.

4) KRS-5. At room temperature KRS-5 is opaque from 40 μm to at least 1500 μm. However, when it is cooled to 4.2°K it opens up at longer wavelengths with a half power point of 750 μm for a crystal thickness of 1 mm. The biggest difficulty in using this material as a filter for millimeter work is caused by its very large refractive index ($n = \sqrt{\varepsilon} = 5.7$, Wolfe, 1965). The large index causes significant reflection losses from the filter surfaces. In an attempt to reduce these losses, quarter wave (at 1 mm) plates of Infrasil quartz were mounted on each side of the filter. Although Infrasil quartz has a refractive index of only 2.0 at 1 mm, it was deemed to be the best material available due to its low water content and structural strength. Ideally, the quarter wave plates should have had a refractive index of $\sqrt{5.7}$ or 2.39. Even with the antireflection plates, the transmission of the KRS-5 filter is only 60% at 1 mm.

Multiplying the transmission of the various components of the filter stack we arrive at a total transmission of 40% at 1 mm.

The field aperture lies just behind the filter stack. This aperture performs two functions. First of all, it

determines the beam size on the sky. The 1/4" aperture corresponds to 64" on the sky with the 5 m Hale telescope. Secondly, the aperture size is roughly the same as the size of the Airy disk for an f/4 beam at 1 mm. As a result, the aperture acts as a long wavelength cutoff filter. The expression for the fraction of light contained inside a radius r of the Airy pattern for a circular aperture is given by:

$$F = 1 - J_0^2\left(\frac{kar}{R}\right) - J_1^2\left(\frac{kar}{R}\right) \qquad (B.1)$$

where $k = 2\pi/\lambda$, a is the radius of the circular aperture (100" for the 5 m Hale telescope), R is equal to $\sqrt{r^2+D^2}$ where D is the distance from the aperture to the Airy pattern (800" for the 5 m telescope at f/4), and J_0 and J_1 are Bessel functions of order zero and one, respectively. Using r = 1/8" and the above values for the Hale telescope, we find:

$$F(\lambda) = 1 - J_0^2(2.48/\lambda) - J_1^2(2.48/\lambda) \qquad (B.2)$$

where λ is measured in millimeters. A plot of this function is shown in Figure B-2.

It should be noted that this expression is not exactly correct, since it does not take the obscuration due to the prime focus cage into account; however, the change resulting from introducing this factor is only of the order of a few percent. Furthermore, equation B.1 is only valid for a point source; for extended sources there is no Airy pattern. As a result, the long wavelength response of the dewar

Figure B-2: Transmission of the various apertures and combinations of apertures in the dewar and telescope.

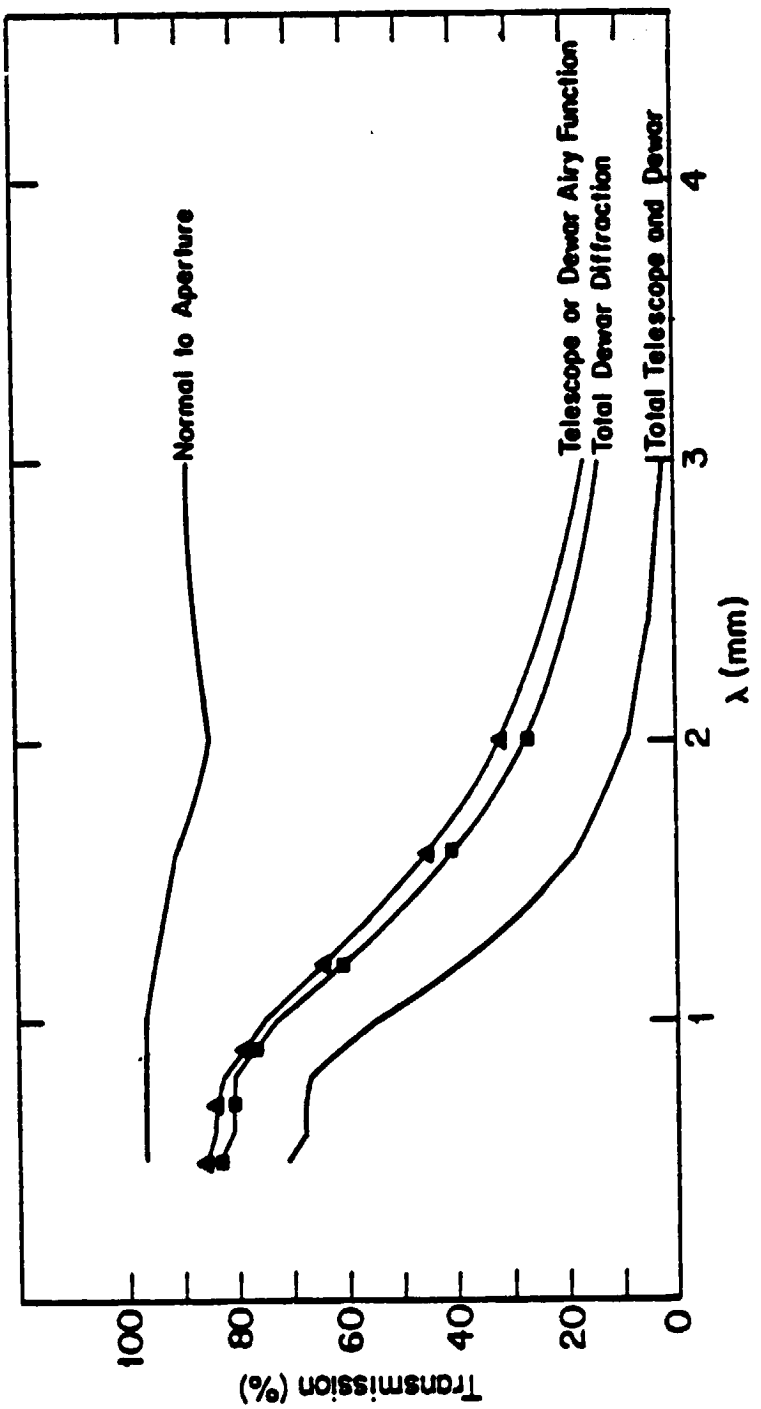
Transmission (%)
100
80
60
40
20
0
1
2
3
4
λ (mm)
Normal to Aperture
Telescope or Dewar Airy Function
Total Dewar Diffraction
Total Telescope and Dewar

changes somewhat depending on the nature of the source.

A short focal length fused silica field lens is located behind the field stop. The focal length was chosen so that together with the integrating cavity entrance aperture the f/# of the dewar would match the f/4 beam of the telescope-photometer combination. The transmission of the fused silica at 1 mm is somewhat uncertain, since the water content of the material is not known. Assuming that it is similar to the fused silica measured in Hadni (1967) a value of 75% can be assigned for the lens transmission.

The long wavelength attenuation due to the integrating cavity entrance aperture can be treated in a similar manner as the field stop. In this case the values to be used in equation B.1 are: a = 3.18 mm, R = 5.28 mm, and r = 0.66 mm. Since the beam f/#'s are the same, equation B.2 is still valid. There are, however, two additional complications:

1) The aperture is roughly equal in size to the wavelength of the incoming radiation. The transmission of normally incident radiation through a circular aperture is given by:

$$T = 1 - \frac{1}{2ka} \int_0^{2ka} J_0(t)dt \qquad (B.3)$$

where a is the radius of the aperture and $k = 2\pi/\lambda$. The integrating cavity entrance aperture has a diameter of 1.32 mm, hence equation B.3 becomes

$$T(\lambda) = 1 - \frac{\lambda}{16.59} \int_0^{16.59/\lambda} J_0(t)dt \qquad (B.4)$$

where λ is in millimeters. This function is plotted in Figure B-2.

2) Radiation will not illuminate the field aperture evenly if a point source is being observed but will instead have an illumination pattern described by the Airy function. Since the field stop is large enough so that most of the Airy central peak fits inside of it at 1 mm, this is a significant effect. Therefore, the expression given in equation B.2 is no longer valid unless an extended source is being observed. Unfortunately, the magnitude of this effect cannot be measured in the laboratory with our present test apparatus since the equipment illuminates the field aperture evenly. Mathematically, the problem is very complex, so that it would need to be solved numerically. Observationally, many of our sources were neither point like nor greatly extended, so that the problem would have to be solved as a function of source size as well. Due to these complications, we have decided to approximate the illumination of the field stop as being totally even, which allowed us to use the measured dewar response in the lab.

Combining the transmission of the filter stack, field lens, and integrating cavity entrance aperture at 1 mm we find a total dewar transmission of 22% at 1 mm.

The measured spectral response of the dewar was measured on both a grating monochrometer and a Fourier transform spectrometer. These results are presented in Figures B-3 and B-4. It can be seen that the grating monochrometer had much better resolution. The mercury vapor source of the grating monochrometer was assumed to have a flat spectral output in the 500 μm-1500 μm range. In addition, special precautions were taken to eliminate the effects of diffraction in the monochrometer. The results of the Fourier transform spectrometer have been divided by the response of a Golay cell, which was assumed to have a flat response.

Now that we have estimated or measured the transmission and spectral response of the various optical elements of the dewar we are in a position to be able to give the optical performance of the bolometer and dewar. The dewar optical NEP was measured on a test stand consisting of a variable aperture, chopper wheel, and liquid nitrogen source. In both the optical and electrical NEP measurements the noise was measured at a frequency of 10 Hz. Integrating the dewar response curve over the black body function for the liquid nitrogen chopping gives the total power entering the bolometer integrating cavity as

$$P = \frac{3.86 \times 10^{-9}}{(f/\#)^2} \text{ watts} \qquad (B.5)$$

where (f/#) is the f number of the test stand aperture (dewar-aperture distance/aperture diameter). This expression

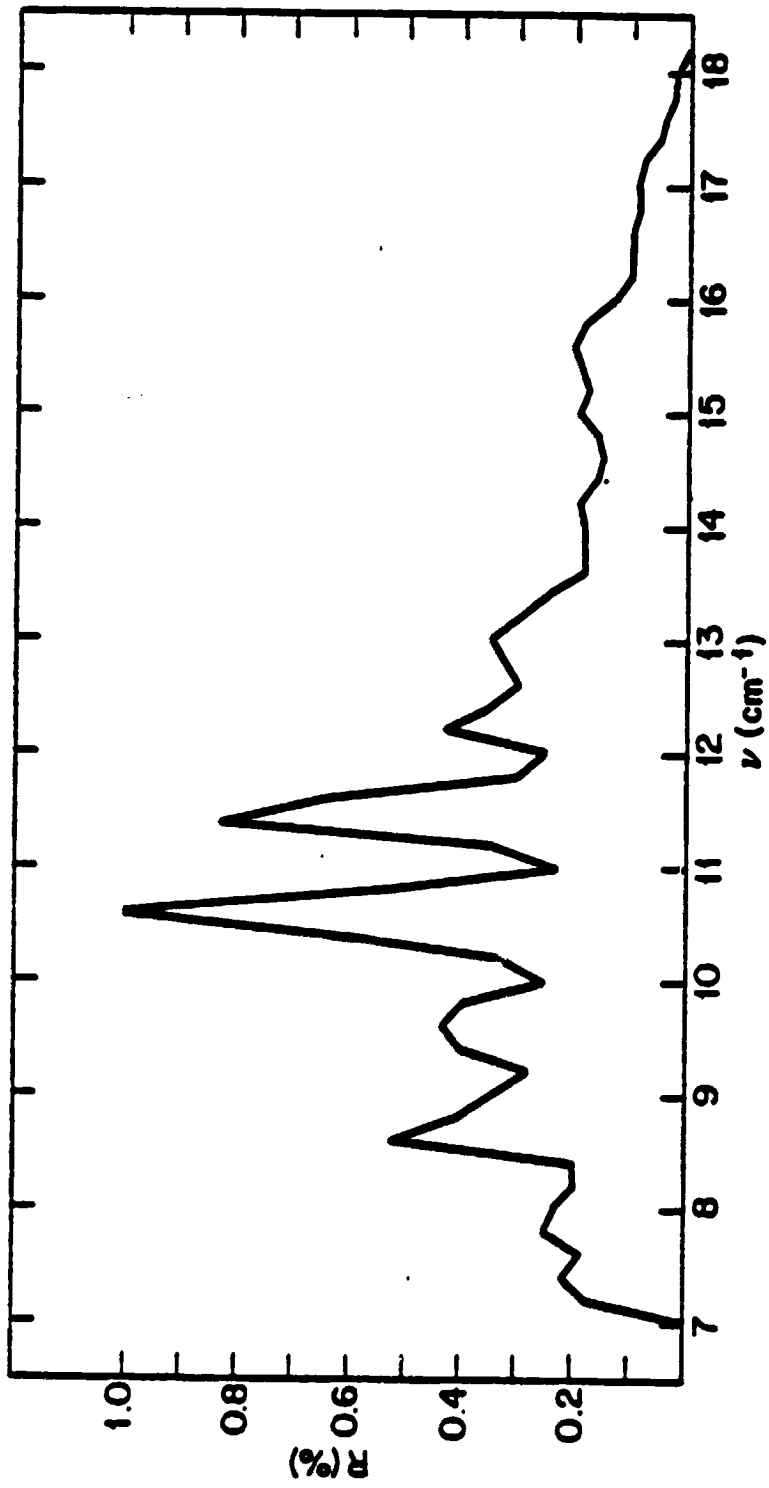

Figure B-3: Grating monochromater dewar response.

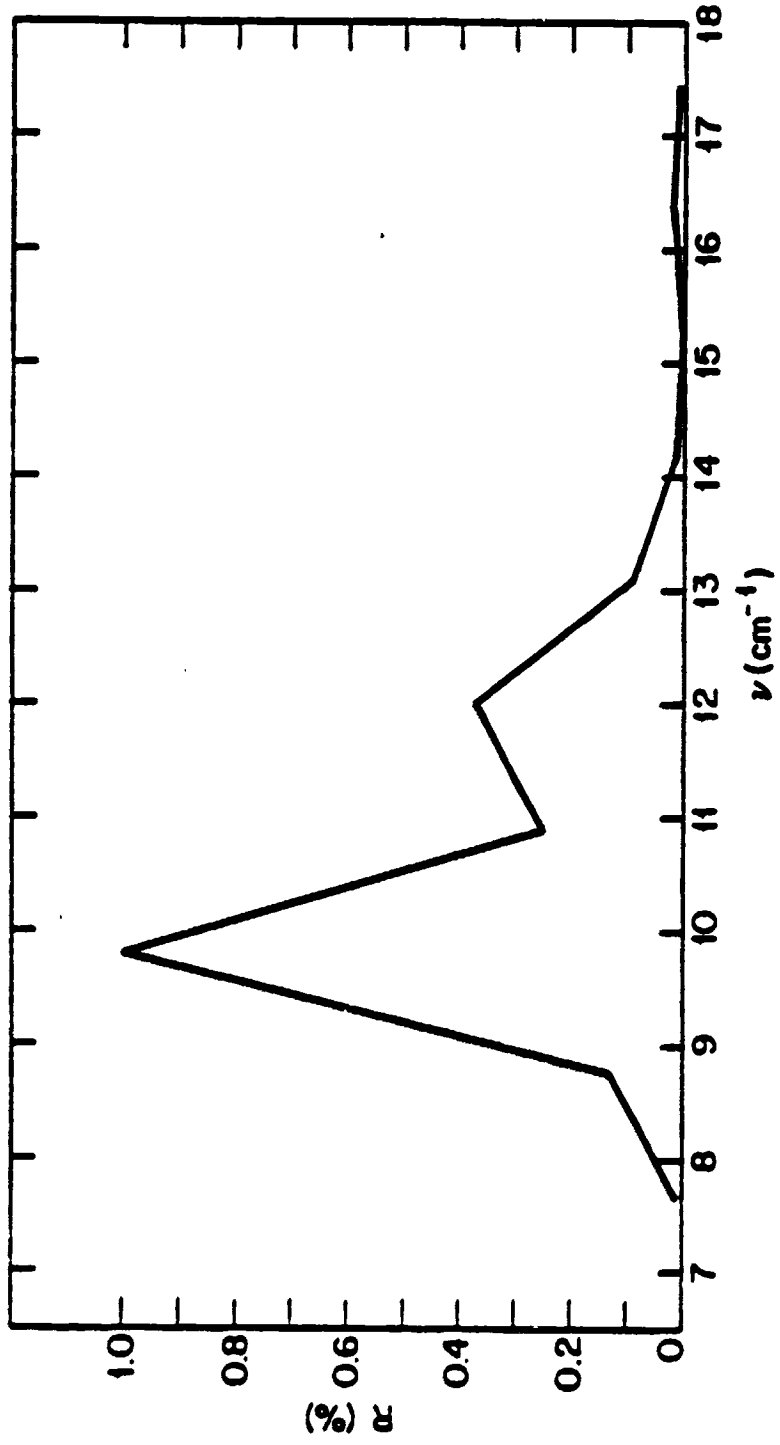

Figure B-4: Fourier transform spectrometer dewar response.

is valid only up to f/4, the entrance aperture of the dewar. Now diffraction has the effect of smoothing the edges of the dewar f-beam pattern. Therefore, in order to accurately measure the optical performance of the bolometer, an f/35 source was used in the test stand. Finally, in order to compare an optical NEP with the electrical NEP the optical NEP must be converted to a DC response. This can be done using equation A.2. With the time constant given in Table A-3 and a chopping frequency of 10 Hz this amounts to a factor of 0.75 that must be multiplied against the 10 Hz optical NEP measurement to convert it to a DC measurement.

The optical performance of the dewar and bolometer is given in Table B-1. This performance can now be compared with the electrical NEP derived in Appendix A to find a bolometer absorption efficiency of 37%.

Table B-1

Bolometer Optical Performance

Dewar optical NEP (10 Hz)	2.5×10^{-14} W/$\sqrt{\text{Hz}}$
Bolometer optical NEP (10 Hz)	5.1×10^{-15} W/$\sqrt{\text{Hz}}$
Bolometer optical NEP (D.C.)	3.9×10^{-15} W/$\sqrt{\text{Hz}}$
Bolometer absorption efficiency	37%

Appendix C

Atmospheric Corrections

In order to correctly interpret the 1 mm signals measured on the telescope, the effects of the atmosphere must be removed. This is done by modeling these effects using an appropriate atmospheric model, deriving a number that is a measure of the magnitude of the atmospheric effects, and dividing the signals received on the telescope by this number.

Water vapor is responsible for most of the atmospheric absorption at 1 mm. The water vapor absorption parameters used in our atmospheric model were derived from Burch (1968). The data correction method that was employed was exactly the same as the one described in Elias et al. (1978).

The flux density from any object is approximated by

$$F(\nu) = F_0(\nu/\nu_0)^n \qquad (C.1)$$

where ν_0 is 3×10^{11} Hz and n is the spectral index of the object. Therefore, the total system response to this object will be given by

$$S = \int F(\nu)R(\nu)d\nu = F_0\int(\nu/\nu_0)^n R(\nu)d\nu \qquad (C.2)$$

where $R(\nu)$ is the total dewar, telescope, and atmospheric response at frequency ν. We can therefore define a function

$$Q \equiv \int(\nu/\nu_0)^n R(\nu)d\nu \qquad (C.3)$$

The function $R(\nu)$ will depend on the atmospheric

response, which is predominantly a function of the water vapor in the line of sight, and the dewar and telescope response, which will vary slightly with the spatial extent of the source. Therefore, Q(n,w) can be tabulated for both point and extended sources, where w is a measure of the water vapor in the line of sight. Some representative Q curves are shown in Figure C-1. The curves were derived from the dewar response shown in Figure B-3.

During 1 mm observations the water vapor is measured hourly with the Westphal hygrometer as long as the sun is up. During the night the water vapor is estimated by comparing the observed signals of standard objects with earlier measurements of the same objects measured in the daytime. Since the sensitivity of the bolometer remains constant to a high degree, the atmospheric model can then be used backwards to find the precipitable water vapor.

The accuracy of the Q curves can be checked in two ways. The results along a curve can be checked by following an object as it sets, since this will change the airmass and hence the water vapor in the line of sight. A plot of the raw signal from NGC 7027 versus water vapor integrated along the line of sight is shown in Figure C-2. Although there is considerable scatter in the points, there is little evidence of a steep systematic slope in the data. There may be a very slight negative slope, but the errors introduced by this are much less than the other calibration errors.

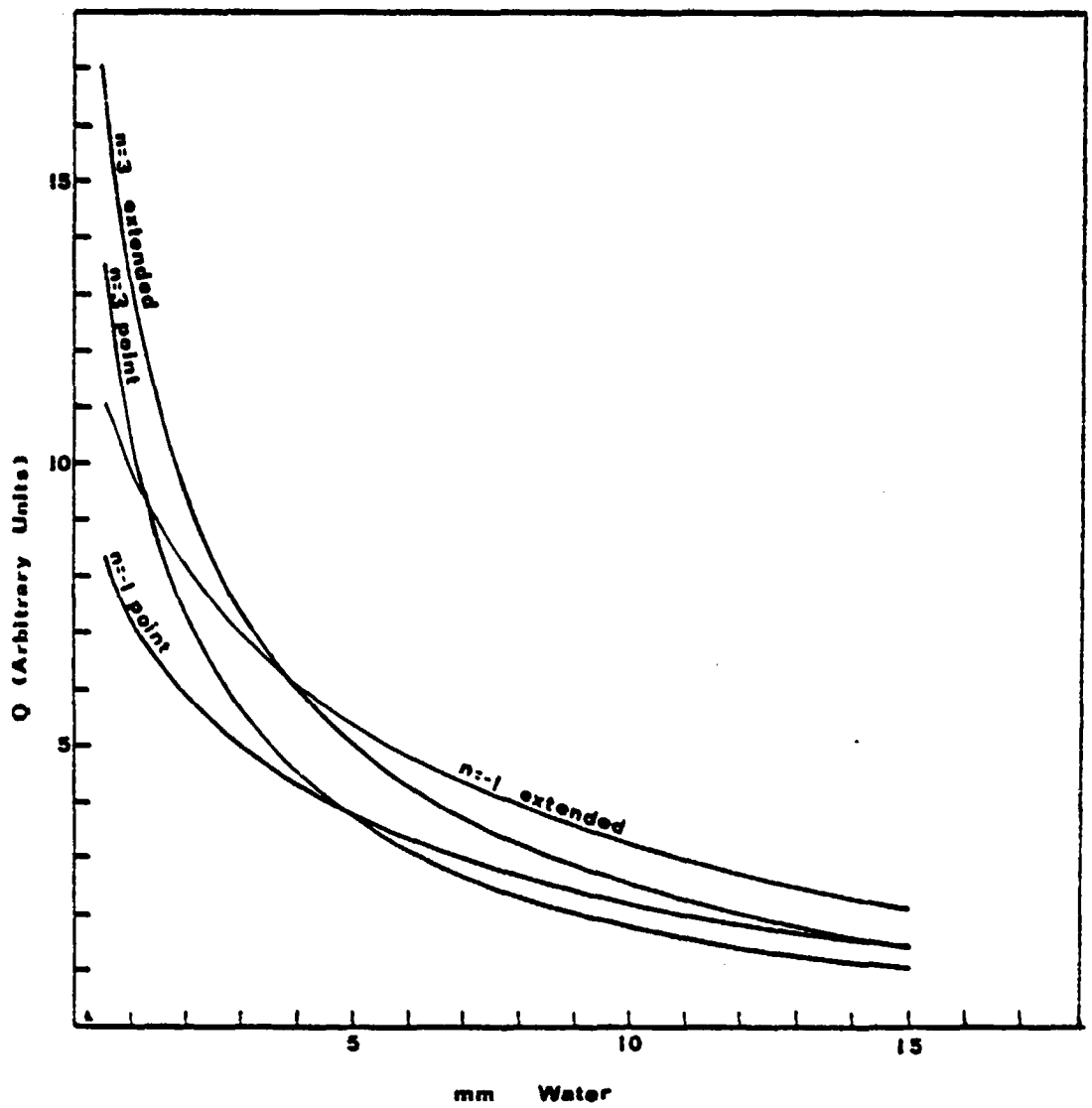

Figure C-1: Plot of Q as a function of water vapor, w, for the two spectral indices and both extended and point sources.

Figure C-2: Plot of signal from NGC 7027 divided by Q for different water vapor levels.

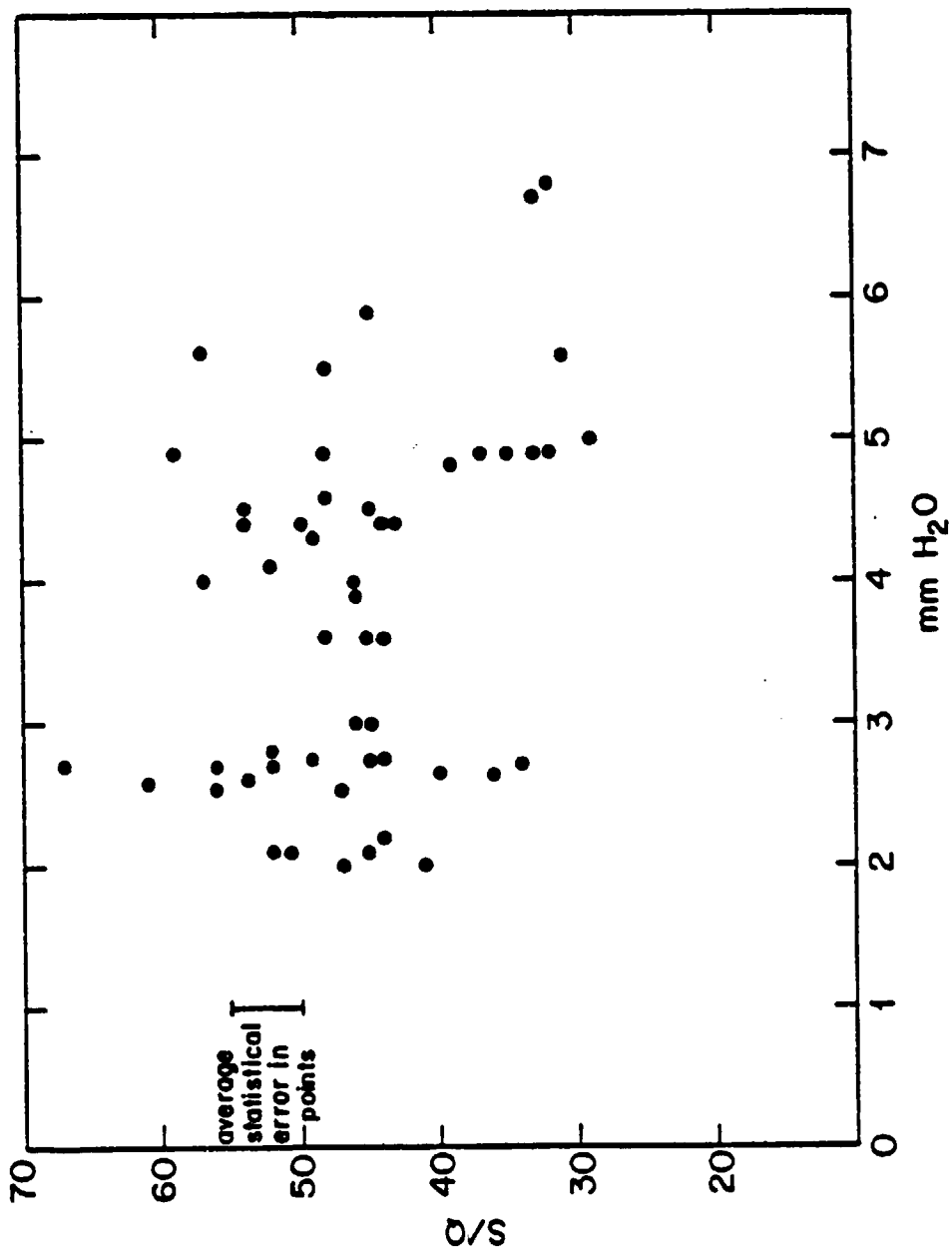
S/σ
70
60
50
40
30
20
0
1
2
3
4
5
6
7
mm H_2O
average statistical error in points

The curves can also be checked by observing two objects with different spectral indices and with known fluxes. We have used the planets and NGC 7027 for this test. Interpolating from radio and far infrared measurements we derive a 1 mm flux from NGC 7027 of 5.5 Jy (Terzian, 1978; Moseley, 1979). Using our method of data reduction and our atmospheric model we find an observed 1 mm flux of 5.8 ± 0.8 Jy from NGC 7027 with Saturn as a calibrator. Since the spectral indices of NGC 7027 and Saturn were taken to be 0 and 2, respectively, this agreement between our flux and the interpolated flux shows that the Q's are also accurate between curves. The 1 mm measurement of Elias et al. (1978) gives a value of 4.8 ± 1.0 Jy for NGC 7027 at 1 mm, in good agreement with our results. We therefore conclude that our atmospheric model does correct for most of the effects of the atmosphere.

Using the Q values derived from our atmospheric model we find that the 1 mm flux from an unknown object is given by

$$F = F_s \frac{Q(w_s,n_s)}{S_s} \frac{S}{Q(w,n)} \qquad (C.4)$$

where F_s is the flux from the 1 mm standard, w_s is the water vapor along the line of sight to the standard, n_s is the spectral index of the standard, and S_s is the raw signal received from the standard. S, w, and n are similarly defined for the object.

We can define the effective wavelength during an observation from

$$\lambda_{eff} = 1 \text{ mm } \frac{Q(w,n)}{Q(w,n+1)} \qquad (C.5)$$

λ_{eff} is plotted for two values of n as a function of w for two values of n in Figure C-3. This figure shows that the effective wavelength can be considered to be 1 mm for just about any object in any water vapor conditions.

Figure C-3: Plot of the effective wavelength of the ^3He millimeter system as a function of water vapor, w.

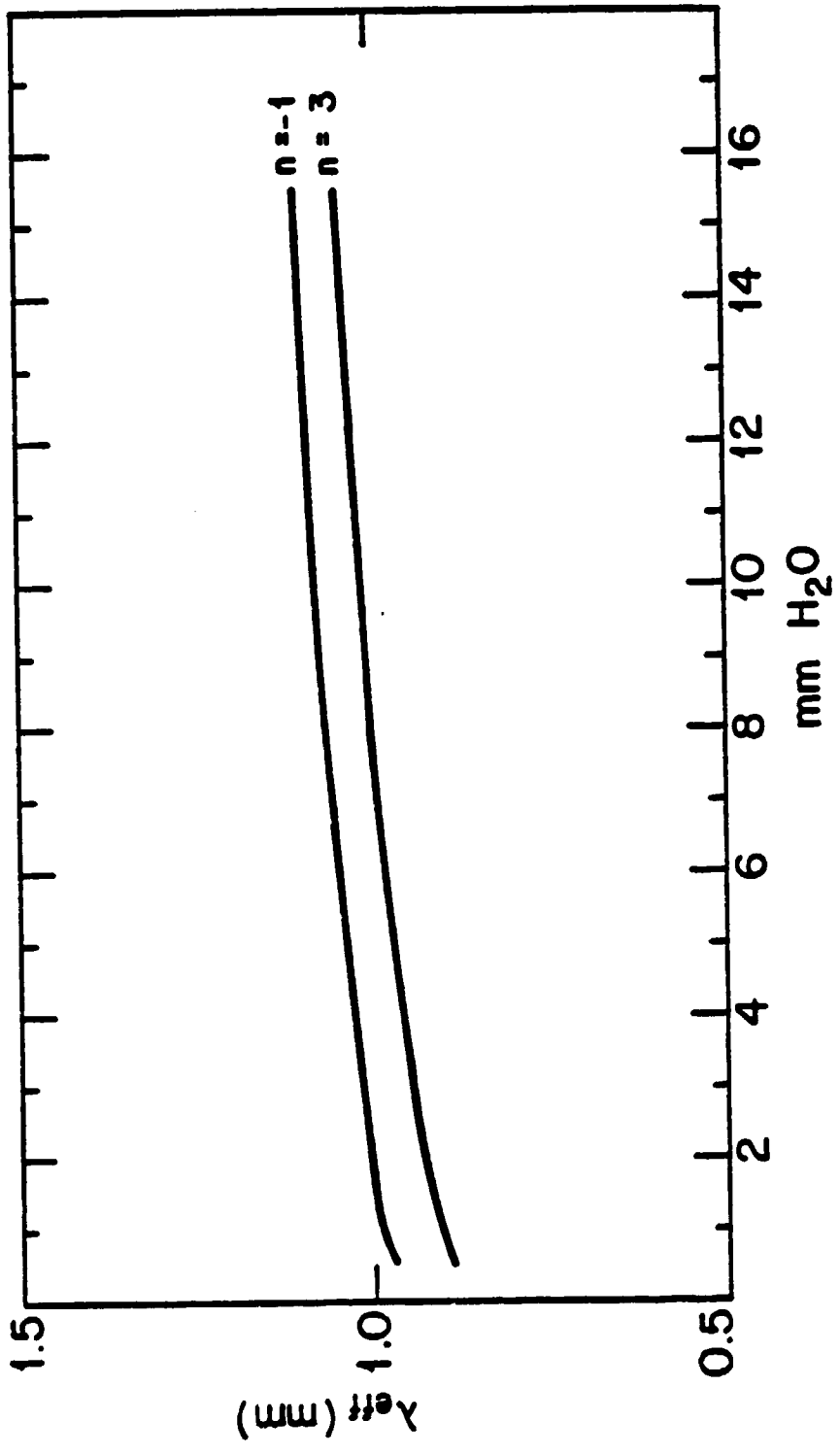
n=-1
n=3
1.5
1.0
0.5
λ_{eff} (mm)
2
4
6
8
10
12
14
16
mm H_2O

References

Aannestad, P. A. (1975) Ap. J., 200, 30.

Ade, P.A.R., Clegg, P. E., and Rather, J.D.G. (1974) Ap. J. Lett., 189, L23.

Aitken, D. K. and Jones, B. (1973) Ap. J., 184, 127.

Baker, J. R., Haslan, C.G.T., Jones, B. B., and Wielebinski, R. (1977) Astron. & Astrophy., 59, 261.

Becklin, E. D., Fomalont, E. B., and Neugebauer, G. (1973) Ap. J. Lett., 181, L27.

Becklin, E. E., Gatley, I., Matthews, K., Neugebauer, G., Sellgren, K., Werner, M. W., and Wynn-Williams, C. G. (1980) Ap. J., 236, 441.

Blitz, L. and Shu, F. H. (1980) Ap. J., 238, 148.

Burbridge, E. M., Burbridge, G., and Rubin, V. C. (1964) Ap. J., 140, 942.

Burch, D. E. (1968) J. Opt. Soc. Am., 58, 1383.

Combes, F., Gottesman, S. T., and Weliachew, L. (1977) Astron. & Astrophy., 59, 181.

Clarke, J., Hoffer, G. I., Richards, P. L., and Yeh, N.-H. (1977) J. Appl. Phys., 48, 4865.

de Vaucouleurs, G. and Pence, W. A. (1978) Astron. J., 83, 1163.

Dent, W. A. and Balonek, T. J. (1980) Private communication.

Draine, B. T. (1980) Preprint.

Draine, B. T. and Salpeter, E. E. (1979) Ap. J., 231, 438.

Dressel, L. L. and Condon, J. J. (1976) Ap. J. Supp. Ser., 31, 187.

Drew, H. D. and Sievers, A. J. (1969) Appl. Opt., 8, 2067.

Elias, J. H., Ennis, D. J., Gezari, D. Y., Hauser, M. G., Houck, J. R., Lo, K. Y., Matthews, K., Nadeau, D., Neugebauer, G., Werner, M. W., and Westbrook, W. E. (1978) Ap. J., 220, 25.

Elvius, A. (1972) Astron. & Astrophy., 19, 193.

Ennis, D. J. (1979) Private communication.

Ferch, R. C. (1977) Thesis, Cornell University.

Forrest, W. J., (1980) Private communication.

Gillett, F. C., Kleinmann, D. E., Wright, E. L., and Capps, R. W. (1975) Ap. J. Lett., 198, L95.

Gottesman, S. T. and Weliachew, L. (1977) Ap. J., 211, 47.

Gould, R. J. and Rephaeli, Y. (1978) Ap. J., 219, 12.

Hadni, A. (1967) "Essentials of Modern Physics Applied to the Study of the Infrared" (Oxford: Pergammon Press).

Harper, D. A. and Low, F. J. (1973) Ap. J. Lett., 182, L89.

Harwit, M. O. and Pacini, F. (1975) Ap. J. Lett., 200, L129.

Harwit, M. O., Soifer, B. T., Houck, J. R., and Pipher, J. L. (1972) Nat. Phys. Sci., 236, 103.

Haynes, R. F., Huchtmeier, W.K.H., Siegeman, B. C., and Wright, A. E. (1975) "A Compendium of Radio Measurements of Bright Galaxies" (Sydney: CSIRO Div. Radiophysics).

Heckman, T. M., Balick, B., and Sullivan III, W. T. (1978) Ap. J., 224, 745.

Hildebrand, R. H., Whitcomb, S. E., Winston, R., Stiening, R. F., Harper, D. A., and Moseley, S. H. (1977) Ap. J., 216, 698.

Hildebrand, R. H., Whitcomb, S. E., Winston, R., Stiening, R. F., Harper, D. A., and Moseley, S. H. (1978) Ap. J. Lett., 219, L101.

Hoffman, W. F., Frederick, C. L., and Emery, R. J. (1971) Ap. J. Lett., 164, L23.

Houck, J. R., Forrest, W. J., and McCarthy, J. F. (1980) Preprint.

Khachikian, E. Ye. and Weedman, D. W. (1971) Astrofizika 7, 389.

Khachikian, E. Ye. and Weedman, D. W. (1974) Ap. J., 192, 581.

Kleinmann, D. E., Gillett, F. C., and Wright, E. L. (1976) Ap. J., 280, 42.

Krumm, N. and Salpeter, E. E. (1979) Astron. J., 84, 1138.

Leung, C. M. (1975) Ap. J., 199, 340.

Leung, C. M. (1976) Ap. J., 209, 75.

Lynds, C. R. and Sandage, A. (1963) Ap. J., 137, 1005.

Morris, M. and Lo, K. Y. (1978) Ap. J., 223, 803.

Moseley, S. H. (1979) Thesis, Univ. of Chicago.

Muehlner, D. and Weiss, R. (1973) Phys. Rev. D, 7, 326.

Neugebauer, G., Becklin, E. E., Oke, J. B., and Searle, L. (1976) Ap. J., 205, 29.

Nishioka, N. S., Richards, P. L., and Woody, D. P. (1978) Appl. Opt., 17, 1562.

Osterbrock, D. E. and Koski, A. T. (1976) MNRAS, 176, 61P.

Phillip, H. R. (1977) Phys. Rev. D, 16, 2896.

Richard, L. J., Palmer, P., Morris, M., Turner, B. E., and Zuckerman, B. (1977) Ap. J., 213, 673.

Rieke, G. H., Harper, D. A., Low, F. J., and Armstrong, K. R. (1973) Ap. J. Lett., 183, L67.

Rieke, G. H. and Low, F. J. (1972) Ap. J. Lett., 176, L95.

Rieke, G. H. and Low, F. J. (1975) Ap. J. Lett., 199, L13.

Roberts, M. S. (1969) Astron. J., 74, 859.

Rogstad, D. H., Rougoor, G. W., and Whiteoak, J. B. (1967) Ap. J., 150, 9.

Rogstad, D. H., Shostak, G. S., and Rots, A. H. (1973) Astron. & Astrophys., 22, 111.

Rowan-Robinson, M., Clegg, P. E., and Ade, P.A.R. (1975) MNRAS, 172, 603.

Salpeter, E. E. (1977) Ann. Rev. Astron. & Astrophys., 15, 267.

Sancisi, R. and Allen, R. J. (1979) Astron. & Astrophys., 74, 73.

Sandage, A. R. (1961) "The Hubble Atlas of Galaxies" (Washington, D.C.: Carnegie Institute of Washington).

Sandage, A. R. and Tammann (1975) Ap. J., 196, 313.

Savage, B. D. and Mathis, J. S. (1979) Ann. Rev. Astron. & Astrophys., 17, 73.

Scoville, N. Z., Solomon, P. M., and Sanders, D. B. (1979) in "The Large Scale Characteristics of the Galaxy," IAU Symposium #84 (Boston: D. Reidel).

Solinger, A., Morrison, P., and Markert, T. (1977) Ap. J., 211, 707.

Solomon, P. M. and de Zafra, R. (1975) Ap. J. Lett., 199, L79.

Solomon, P. M., Scoville, N. Z., Jefferts, K. B., Penzias, A. A., and Wilson, R. W. (1972) Ap. J., 178, 125.

Stein, W. A. and Weedman, D. W. (1976) Ap. J., 205, 44.

Tammann, G. A. and Sandage, A. R. (1968) Ap. J., 151, 825.

Telesco, C. M. and Harper, D. A. (1980) Ap. J., 235, 392.

Terzian, Y. (1978) in "Planetary Nebulae, Observations and Theory," ed. Y. Terzian (Boston: D. Reidel).

Thronson Jr., H. A. and Harper, D. A. (1979) Ap. J., 230, 133.

Traub, W. A. and Stier, M. T. (1975) Preprint.

Traub, W. A. and Stier, M. T. (1976) Appl. Opt., 15, 364.

Walker, M. F. (1968) Ap. J., 151, 71.

Werner, M. W., Elias, J. H., Gezari, D. Y., Hauser, M. G., and Westbrook, W. E. (1975) Ap. J. Lett., 199, L185.

Werner, M. W., Neugebauer, G., Houck, J. R., and Hauser, M. G. (1978) Icarus, 35, 289.

Werner, M. W. and Salpeter, E. E. (1969) MNRAS, 145, 249.

Westbrook, W. E., Werner, M. W., Elias, J. H., Gezari, D. Y., Hauser, M. G., Lo, K. Y., and Neugebauer, G. (1976) Ap. J., 209, 94.

Westphal, J. A. (1974) "Infrared Sky Noise Survey, Final Report," grant NGR 05002185 NASA CR139693, N74-32782 (Springfield, VA: National Technical Information Services).

Wolfe, W. L. (1965) "Handbook of Military Infrared Technology," W. L. Wolfe, ed. (Washington, D.C.: U. S. Government Printing Office).

Woody, D. P. and Richards, P. L. (1979) Phys. Rev. Lett., 42, 925.

Wright, E. L. (1976) Ap. J., 210, 250.

Wynn-Williams, C. G. and Becklin, E. E. (1974) PASP, 86, 5.